Ab initio study of the effect of charge localisation on the properties of defects in magnesium oxide and zirconolite

Jack Mulroue

UCL

Department of Physics and Astronomy

A Thesis submitted for the degree of Doctor of Philosophy

I, Jack Mulroue, confirm that the work presented in this thesis is my own. Where information has been derived from other sources, I confirm that this has been indicated in the thesis.

Acknowledgements

I would firstly like to thank my supervisor Dorothy Duffy for her help and guidance through the PhD. I am very grateful that she allowed me to take control of the research but also for preventing me from taking it in too many different directions. Her support has been instrumental in the progress of the research involved in this thesis.

I would also like to thank my second supervisor Alex Shluger for his help and expertise during the research. Our talks were always insightful and very helpful in explaining the mistakes I'd made and also what analysis needed to be done.

The knowledge of Keith McKenna, Matthew Watkins and Matthew Wolf in the computational codes used was a great help. I must also thank them for their patience when explaining the reason behind the observed results. I would like to thank Andrew Morris for his help in using AIRSS and for reading through this thesis.

I would finally like to thank Kelly Hutchinson for proofreading the majority of the thesis in her spare time and for showing there was more to life then just the PhD. Also the rest of my friends and family for their support.

Abstract

The localisation of excited electrons on defects in ceramic materials has a significant effect on the evolution of damage resulting from irradiation. The localisation of charge on a defect will change the charge state of that defect, which will affect the position of the defect level and change the defect properties. In ceramic materials for encapsulating radioactive waste the alpha decay of the actinide results in the accumulation of helium within the lattice, which will affect the durability of the waste and alter the performance of the waste form. DFT was used to study the structure and mobility of defects in different charge states for two ceramic materials. MgO was used as a model oxide due to the simple crystal structure. It was found that the charge state has a significant effect on the structure and mobility of the oxygen defects. The localisation of a hole onto the O^{2-} interstitial significantly reduces its migration barrier. The effect of charge localisation on a hexa-interstitial cluster was investigated and it was found that the charge state affects the migration barriers, with the singly charged cluster again having the lowest migration barrier. Zirconolite, a proposed encapsulation matrix for plutonium, was also studied. The monoclinic crystal structure comprises of layers of alternating 5- and 6-fold coordinated Ti-O polyhedra, separated by layers of alternating Ca and Zr ions. The structures of intrinsic defects, in different charge states, were studied and a significant effect on the defective structure of Zr and Ti vacancies was observed. *Ab initio* random structure searching was used to identify the lowest energy interstitial site for each species. DFT-D3 was used to study the structure, mobility and binding of a He atom in zirconolite. It was found that the neutral 5-fold coordinated Ti vacancy was the strongest binding site.

Publications

J. Mulroue and D. Duffy, *Proceedings of the Royal Society A* **467**, 2011, 2054

J. Mulroue, A. J. Morris and D. Duffy, *Physical Review B* **84**, 2011, 094118

D. Duffy, S. Daraszewicz and J. Mulroue, *Nuclear Instruments and Methods in Physical Research B: Beam Interactions with Materials and Atoms* **277**, 2012, 21

J. Mulroue, M. Watkinks, A. J. Morris and D. Duffy, *Journal of Nuclear Material*, submitted

J. Mulroue, B. Uberuaga and D. Duffy, *Journal of Physics: Condense Matter*, submitted

Presentations

Radiation Damage workshop - Sheffield 2012 “Density functional theory modelling of intrinsic defects and He in zirconolite”

MRS - XXXV Scientific Basis for Nuclear Waste Management - Buenos Aires, Argentina 2011 “ Density functional theory modelling of the effect of charge localisation on the structure and migration of defects in MgO”

UNTF 2011 - Huddersfiels 2011 “Density functional theory study of defects in zirconolite”

NUMAT 2010 - Karlsruhe, Germany 2010 “ An ab initio study of the effect of charge state on the properties of point defects in MgO”

CCP5 Radiation Damage in Materials - Daresbury 2010 “A study of defects and radiation damage in zirconolite”

Posters

MRS - XXXV Scientific Basis for Nuclear Waste Management - Buenos Aires, Argentina 2011 “Density functional theory modelling of the intrinsic defects and He in zirconolite”

NUMAT 2010 - Karlsruhe, Germany 2010 “A study of irradiation induced damage in zirconolite”

Actinides: Correlated electrons and nuclear materials - Manchester 2010 “modelling ceramics for radioactive waste disposal”

Contents

List of Tables

List of Figures

Chapter 1

Introduction

The reduction in the amount of carbon dioxide (CO_2) generated is seen as a vital component of tackling climate change and nuclear energy is seen as the only achievable way of generating large quantities of low carbon energy. However, there are issues with nuclear energy that must be overcome if it is to be the dominant electricity generator, the most pressing issue being how to deal with the long lived radioactive waste generated from the nuclear fuel cycle. Nuclear waste is divided into three categories depending on the activity of the waste and the half-lives ($t_{1/2}$) of the species present: these are low-level waste (LLW), intermediate-level waste (ILW) and high-level waste (HLW). LLW contains a small amount of short half-life material. It comprises materials that are taken onto a nuclear site, such as paper, overalls and tools and it only accounts for 1% of the total radioactivity of nuclear waste. The ILW comprises of the resins and metal which encased the fuel and it is stored in metal cans encapsulated in Portland cement (OPC). High level waste accounts for 95% of the total reactivity of the waste generated from the nuclear cycle. This waste stream contains the radioactive elements from the nuclear fuel and those generated through the reprocessing of the nuclear waste.[5]

1.1 Disposal routes of nuclear waste

The three classes of radioactive waste require different levels of protection to prevent the distribution of radiation into the biosphere, and therefore different disposal routes are used for each waste category. LLW is disposed of at a site in Drigg, north Cumbria, where the waste is stored in concrete vaults below the surface after being compressed to reduce the volume of the disposed waste.[6] The ILW is currently stored as a concrete encapsulant, with Portland cement used to solidify the metal fuel cladding and chemical sludges inside a steel drum. Different viscosities of cement can be used, depending on the structure of the waste, to ensure complete encapsulation and prevent any voids being formed. The alkali environment of the cement used can limit the waste that can be disposed of, such as aluminum components, as $Ca(OH)_2$ reacts with Al to produce hydrogen.[7] The hydrogen gas leads to bubble formation inside the cement, causing a decrease in the mechanical strength. HLW is currently stored as a vitrified product, a solid matrix of borosilicate glass inside a steel drum.[5] The liquid waste is calcined (turned into an oxide) before being mixed into the molten glass. The glass can contain p-block and transition metal oxides to act as stabilisers and network modifiers to prevent the HLW clustering or settling inside the canister. The vitrified waste is then stored above ground at the Sellafield site before being transported back to the nuclear power plants where the waste was produced.[5]

However, there is currently no disposal route for the HLW and ILW but the National Decommissioning Authority (NDA) has proposed a geological disposal facility (GDF) to dispose of this waste. The proposed GDF has a multi-barrier design[8] which consists of a number of barriers to reduce the rate at which radioactive elements will be transferred to the biosphere. The designed barriers are divided into two sections, the near field and the far field; with the near field consisting of man-made barriers around the waste, while the far field is the back-fill material and the host rock the GDF is located in. The first of the near field barriers is the waste itself, with a solid waste form which introduces a diffusion barrier for the actinide species to be leached, thus slowing the rate of release from the waste form. The metal waste container acts as the second barrier of the near field by preventing the ground water from coming into contact with the waste. The role of the far field is to create a highly alkaline environment which will help suppress the release of the actinide species into the ground water should it enter the facility, as the solubility of the actinides is low in alkaline solutions.[9]

1.2 Waste matrices for HLW

The proposed use of ceramic matrices instead of borosilicate glasses as an encapsulant for HLW is due to the superior retention of actinide species in leach tests[10] and in naturally occurring ceramic materials.[11] The retention of the actinides in ceramic materials is caused by the actinide species being chemically bonded within the matrix. The species are substituted into the lattice of the ceramic whereas in the glass the actinides are retained due to the steric hindrance introduced by the silica matrix. The leaching rate of the actinide species from a ceramic matrix is hundred times smaller than that of borosilicate glass.[12]

However, the use of ceramics has limitations when compared to those of glasses, the first being the amount of actinide which can be loaded into the structure. Zirconolite is a ceramic proposed as an encapsulation matrix that can be loaded up to 30 wt% before any additional crystal structures forms,[13] although $CaPuTi_2O_7$ has been synthesised.[14] In practice it is expected to be limited to a loading of 10 wt% compared to borosilicate glass, which has a loading of 25 wt%.[10] The decrease in wt% loading of the waste form means that a greater number of ceramic waste forms are needed to encapsulate the same amount of waste as glasses. This leads to problems for the GDF as the size will need to be increased to accommodate the increased number of waste forms. Glass encapsulants are able to accommodate a number of elements into their matrices due to the way they isolate the waste. However, as the ceramics incorporate the waste elements into the lattice structure this limits the range of elements it can encapsulate. There are two routes around this problem: the first is to use only pure actinide oxides when encapsulating; the second is to use a range of matrices, each capable of accommodating different waste species. An example of this second option is SYNROC, a synthetic rock, which comprises at least three different ceramics. SYNROC was first derived at the Australian Nuclear Science and Technology Organisation (ANSTO) and has different compositions designed for each waste stream. The composition which has received the most interest is SYNROC-C which was derived by Ringwood in 1981.[12] This composition contains zirconolite, pyrochlore and hollandite and is used for the encapsulation of HLW. The zirconolite is the major actinide-bearing phase with pyrochlore also accommodating some actinides and the hollandite accommodating the fission products. However, as there is no universal composition achievable, no universal route for disposal can be achieved, unlike glasses. Glasses are constructed from amorphous networks of silica chains, therefore the bombardment by the recoil particle has little significance on the structural integrity of the glass waste form. On the other hand, the ceramic waste forms are constructed from crystalline lattice structures, which become amorphous after continual cascade events. The amorphisation of the ceramic lattice has a significant effect on the chemical and physical durability of the waste, with the leaching of Si from zircon increasing by one or two orders of magnitude through alpha bombardment.[15] The amorphisation of the lattice structure also leads to volume swelling and shear deformation.[16] The volume swelling is caused by relaxation of the lattice ions due to the presence of defects created by the irradiation, as the interstitial defects cause larger relaxations in the lattice than the relaxations around the vacancies.

The ceramic encapsulation matrices can be synthesised through isostatic pressing or the sol-gel method. The isostatic press method can be achieved through heating (hot isostatic press(HIP)) or at room temperature (cold isostatic press(CIP)). The HIP requires the ceramic and waste components to be in an oxide form and these are placed in a steel canister.[10] A lid is inserted with copper seals placed between the lid and container before the system is heated. The copper seals melt before the solid state reaction occurs, forming a sealed canister before any of the volatile radionuclides are released from the waste,[10] meaning less protection is needed for the people operating the process. The canisters have been designed to collapse under the pressure inside the chamber making a more dense waste form and producing a uniform waste package. The CIP is similar to HIP but performed at room temperature and uses a liquid instead of a gas to apply the pressure. The advantage of using CIP over HIP is that higher pressures can be reached, the pressure is applied uniformly and it is cheaper as no heating is required. However, the lower temperatures used means that the sample needs to be sintered after being pressed, which adds an additional step to the waste form production process. The sol-gel route gives a ceramic with a controlled composition, size and morphology.[17] However, the sol-gel route appears to produce zirconolite crystals that are deficient in Ca, with the maximum uptake of 0.8 instead of the 1 for stoichiometry, while maintaining the Ti:Zr ratio.[17] Also, the method of drying the sol-gel product affects the resulting nanoparticle, with hollow and doughnut particles being produced as well as spheres by altering the spray-drying process.[18]

Many ceramic matrices have been proposed as an encapsulation matrix for HLW, including pure systems like zirconolite and pyrochlore, mixed systems like SYNROC and composite systems like glass-ceramics. Zircon initially received a large amount of attention as the favoured matrix,[19, 15, 20, 21] due to the amount of U found in natural analogues of zircon which has been dated to 2 billion years old.[19] However, the process of synthesising zircon has lead the National Nuclear Laboratories (NNL) to abandon zircon as a waste matrix and focus on other long-lived natural structures that are easier to synthesise and zircon has a higher leach rate when the structure becomes amorphous. Zirconolite and pyrochlores are the natural analogues favoured by the NNL: both have the fluorite crystal structure, are comprised of Ti-O polyhedra and are able to incorporate Pu into their lattice structure. NNL are focusing on zirconolite because of the low leaching rate. When the structures are in an amorphous state it is superior to that of pyrochlores, thus improving the barrier for the multi-barrier design.[22] These single phase matrices are only able to encapsulate one or two waste elements in a pure state. SYNROC is a multi-phase encapsulant, allowing multiple waste elements to be incorporated. The composition of the phases can be tailored to fit a particular waste stream, allowing the most suitable encapsulation matrix to be used for each waste species, increasing the durability of the waste form. The localisation of the actinide species in the specific phases leads to problems arising during post encapsulation, the phase which encapsulates the actinides will be subjected to more decay events than the other phases in the waste form. A lattice subjected to radioactive bombardment will swell as the structure accommodates the defects created by the damage, and, as the different phase will be damaged at different rates, the rate of swelling will also differ. When there is a different swelling rate between two phases, such as at a grain boundary within the waste form, it will lead to cracking. These cracks will increase the surface area of the waste available to ground water inside the GDF and will affect the leaching rate of the waste. The encapsulating system favoured by the NNL is the glass-ceramic matrix, consisting of zirconolite crystals, to encapsulate the Pu and U species, suspended in a glass matrix, which encapsulates the other waste species. The advantage of this system is that the waste oxides do not need to be purified, the species not incorporated into the zirconolite lattice are encapsulated within the glass. These systems can also be synthesised via the HIP process, with the addition of SiO_2 and the other modifiers placed inside the canister with the same oxides as the pure ceramic synthesis. The glass-ceramic matrix also allows the vast knowledge of glasses within the nuclear industry to be used. The NDA are considering an additional disposal matrix for Pu in the form of mixed oxide fuel (MOx). The MOx can be used in two different ways, either low specification MOx or irradiated MOx. The low specification MOx mixes PuO_2 with a large quantity of depleted uranium.[5] This has the advantage of diluting the fissile U^{235} generated from the decay of the Pu with U^{238}, which would prevent a build-up of fissile material and prevent a criticality issue inside the GDF. The other option uses MOx as a fuel which is burnt in a reactor to produce electricity. The fuel is then packaged and disposed of in a similar way to current spent fuel. This method then relies on the gamma decay of the fission products to act as a proliferation deterrent and also recycles the Pu generated from reprocessing. However, this option would require a change from government to consider Pu as more than a zero value asset.[23]

1.3 Types of irradiation

There are many ways in which a material can become damaged via irradiation, but there are only four types of ionizing radiation: α, β, γ and neutrons. Neutrons are the largest energy particles generated from irradiation events, having energies up to 14 MeV in fusion reactors.[24] The neutron is generated in the decay of radioisotopes along with other radiation, such as the decay of Be^{14} generating a β ion and a neutron.[25] The high energy of the emitted neutron results in a large number of displacements within a crystal structure via collision cascades, in which the neutron will transfer some of its energy to the ions it collides with along its path.

γ radiation is the emission of a high energy photon, the photon has an usual energy of 35.5 keV from the I^{125} nuclei.[26] A Tc^{99} atom in an excited state, generated from the decay chain Mo^{99}, emits a γ photon as it decays to the Tc^{99} ground state.[5]

$$\mathrm{Tc}^{99}* \longrightarrow \mathrm{Tc}^{99} + \gamma$$

β decay consists of an electron ejected from the nucleus of an atom as a neutron is converted into a proton and the emitted electron. The electron is emitted from such nuclei as Sr^{90} with an energy of 0.54 MeV.[27]

$$\mathrm{Sr}^{90} \longrightarrow \mathrm{Y}^{90} + \beta$$

$$\mathrm{Pu}^{239} \longrightarrow \mathrm{U}^{235} + \alpha$$

The α particle comprises of two protons and two neutrons and is ejected with 4.5-5.8 MeV, allowing it to penetrate 16-22 μm into the lattice from an actinide nucleus.[15] The α particle initially has too much energy for it to interact with the nuclei within the structure but it is in the region of the electronic stopping range. The α particle dissipates its energy into the electron system until the electrons have removed enough energy for it to fall into the nuclear stopping range. The α particle dissipates its energy by creating a few hundred displacements along its path until it has lost all of its energy to the lattice. As a large proportion of the energy was removed via the electronic stopping power of the material, a large number of electron excitations will have been created. These excited electrons are able to diffuse throughout the solid and can self-trap at lattice sites. If self-trapping occurs, the localisation of energy can lead to the formation of Frenkel defects or, if trapped at a defect, it can alter the charge state and properties of that defect.[28]

The majority of radiation damage caused by α decay is caused by the recoil (daughter) nucleus. The U^{235} (generated from the decay of Pu^{239}) ion recoils with 86 keV but only travels 30-40 nm.[15]The energy is in the range of the nuclear stopping power and therefore the recoil nucleus dissipates all of its energy into atomic displacements and over a smaller range than the α particle, leading to an increase in damage produced.

Although the α particle, which has the same structure as the He nucleus, doesn't create as many displacements, each α decay causes a He impurity to be formed. The α particle captures two electrons at the end of its path and becomes a He atom. The behaviour of He in a waste form is vital to the understanding of the long-term durability of a waste form; if an α emitter is present in the waste, He will be too in some concentration. If He is present in low concentrations, it is likely to remain as isolated atoms at the interstitial site within the lattice

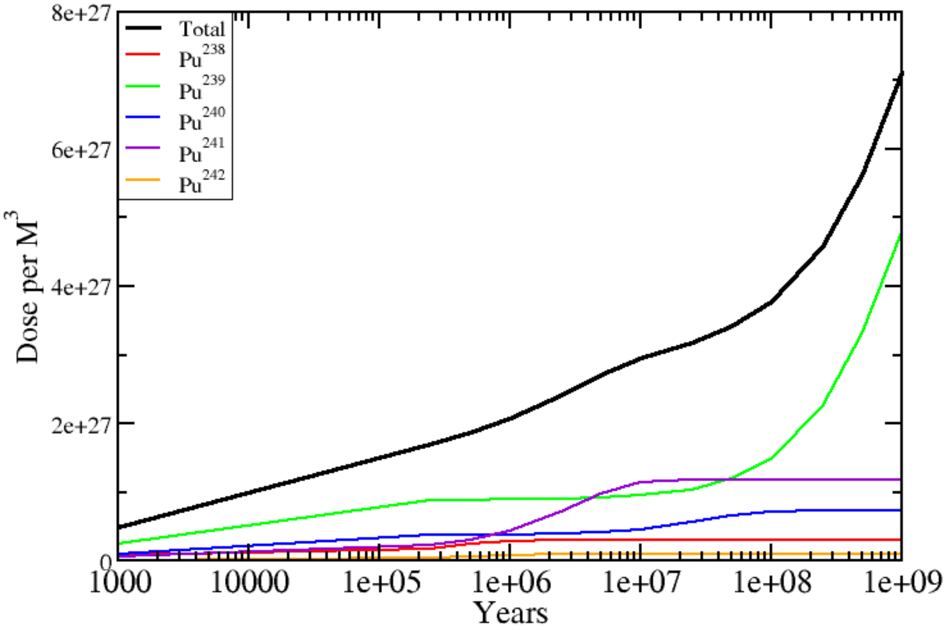

Figure 1.1: Total radiation dose as a function of age for the Pu composition generated from reprocessed PWR fuel.

structure. As the concentration increases, the He atoms will start to interact with each other and may change the defect structure. When a high concentration is present, He interstitials will start to cluster and will lead to the formation of a He bubble in structural voids. These bubbles will grow as more He atoms diffuse to them via Ostwald ripening or a coalescence mechanism.[29] These bubbles have an effect on the structural stability of the solid as well as the properties of defects within the solid.[30] The defect behaviour of He is observed experimentally using various techniques, such as ion beam studies,[11] scanning tunneling microscope (STM) images of actinide loaded samples,[31]and thermal release mass spectroscopy.[32] These techniques along with simulations have been used to study He defects in a number of materials including metals (such as V,[33] W[34] and Fe[35]), alloys (including V-4Cr-4Ti,[33] steel[36] and TZM[37]) and ceramics (zirconolite[32, 31], UO_2 in different stoichiometries[38, 39] and zircon[40, 41]). As mentioned earlier, the NDA are proposing a 10 wt% Pu loading of the waste form, with zirconolite being the preferred matrix of the NNL. This loading is equivalent to having one Pu per unit cell of zirconolite. The Pu^{239} decay sequence involves eight α decays, which means that there will be eight He atoms per Pu atom incorporated into zirconolite. However, each isotope of Pu will go through a different decay sequence and a mixture of Pu isotopes are generated from the reprocessing of nuclear fuel, therefore the total amount of He introduced into the lattice will depend on the composition of the encapsulated Pu. Figure 1.1 shows the He concentration as a function of the waste forms age for the Pu composition generated from the reprocessing of PWR fuel.

1.4 Types of defects

Intrinsic defects in ceramics can be divided into two categories: Schottky and Frenkel defects. Schottky defects consist of a unit formula of cation and anion vacancies,[42] so charge neutrality remains. Frenkel defects consist of either an anion or cation interstitial and vacancy pair.[42] An interstitial is defined as a species not located at a lattice site, i.e. interstitial and vacancy defects are paired as the lattice ion is moved to the interstitial site, leaving a vacancy behind. The Frenkel pair defect is predominantly produced by radiation damage, as the ballistic collisions cause the lattice ions to be permanently displaced from their lattice sites.[28] Point defects are able to combine in other arrangements, leading to the formation of three-dimensional defects called defect clusters. A void is formed within the structure of the solid when vacancies coalesce to form pores on a surface and holes within the bulk. These voids are able to act as trapping sites for other impurities and can therefore lead to the retention of impurities within the solid.[30] The collection of interstitial defects can lead to a variety of clusters with various shapes. Interstitial loops comprise of interstitial defects positioned in interstitial sites in different unit cells to give a cylindrical shape. These loops are able to collapse in on themselves to form a disk and produce a dislocation loop, as the disk inserts a new half-plane of ions into the structure. If alkali halides are subjected to irradiation events, segregation of defects can occur and lead to phase seperation.[43] The cation interstitials congregate together, which leads to the formation of a metallic phase within the host structure. This metallic phase will have a different lattice spacing to that of the host phase, which will lead to strain at the interface and to the eventual degradation of the alkali halide. The halogens are also able to congregate, leading to the formation of bubbles within the structure. These halogen bubbles introduce a large amount of strain on the lattice because of their size, with an average size of 10 nm in NaCl.[43] This can lead to cracking of the solid. Halogen atoms are not the only atoms to form bubbles within lattice structures. The behaviour of fission products is of major interest to the nuclear industry, with the fission gases forming bubbles within the nuclear fuel; only He is an issue for the disposal of HWL, generated from α decay of the actinide species. He bubbles are known to form in a number of different materials, from metals[30, 44] to ceramics.[32, 45] The presence of He bubbles inside a waste form is a concern because if the strain leads to the formation of cracks which will lead to an increase in leaching and will undermine effectiveness of the barrier.

1.5 Effects of electronic localisation

The electronic excitations generated from an irradiation event have a significant effect on the evolution of the damage generated, but current simulation methods for radiation damage neglect these effects due to the method used in these simulations. The results from these calculations are fed into different methods to extend the results to engineering timescales, so the effects missing in the initial simulation are also missing in the long timescale simulations. An effect of the electronic excitations missed in the current simulations is the localisation of the excited electron at sites within the structure. This localisation, known as trapping if it occurs at a defect or self-trapping if it occurs spontaneously at a lattice site, can occur in insulators due to the presence of the band gap and the creation of defect levels, which are able to be occupied by these excited electrons. If these states do localise either electrons or holes then the charge state of the defect will be changed and this will affect the properties of that defect, such as the structure, chemistry and conductivity.[46] Trapping can occur for an electron, a hole or for an exciton (an electron-hole pair) and each type of trapping will affect the lattice in a different way.[46]

The localisation of excited electrons can affect the evolution of the defects by altering the processes involved in recovering the lattice structure from an irradiation event. The migration barriers involved in the displaced ion returning to its original position will be altered, as well as decreasing the Coulomb energy between two defects, resulting in the stabilisation of the defect pair. The localisation can affect the migration barrier by altering the relaxed structure surrounding the defect and, as a result, the pathway along which it diffuses will also change. The different pathways will have different transition states, and so will have different migration barriers. The localisation can stabilise defect pairs by reducing the Coulombic interactions between them, which may normally lead to recombination, by a hole or electron localising on either of the defects, resulting in the charge state of that defect being reduced. Localisation may not only hinder the recovery of the lattice structure but it may also increase the growth rate of defect clusters. The defects cluster to relieve the strain on the lattice caused by the presence of the defect. If more defects are stabilised due to the localisation, there will be more strain in the lattice. Additionally, the new migration pathways may enhance diffusion, allowing the defect to diffuse away before it can recombine in its original position. These changes to the recovery and cluster growth will have an effect on how the microstructure will behave, and as a result, the mechanical stability will also be affected. An understanding of these effects will be important if correct predictions are to be made for the stability of a waste form on geological timescales.

Chapter 2

Computational methods

This chapter discusses the background theory to the computational methods used through this research. The theory used through this work is density functional theory (DFT) and the underlying theory is explained. The advantages and disadvantages of this theory are discussed, as well as the choice of exchange correlation functional used for this research. The key theories for the working of the computational codes used, VASP and CP2K, are explained and also the methods for analysing results used in the discussion of the Chapters 4, 5, 6 and 7.

2.1 Density functional theory

DFT enables the calculation of the ground state energy of a many-body system through the use of electron density instead of electron wave functions. The theory was originally proposed by Hohenberg and Kohn in 1964,[47] which extended the ideas introduced by the Thomas-Fermi model.

Two theorems were introduced by Hohenberg and Kohn, meaning that the Thomas-Fermi model could be used for many-body systems.

Theorem one:

- ‘For any system of interacting particles in an external potential $V_{ext}(\mathbf{r})$, the potential $V_{ext}(\mathbf{r})$ is determined uniquely, except for a constant, by the ground state particle density $n_0(\mathbf{r})$’.[48] This allows for the system’s properties to be calculated if $n_0(\mathbf{r})$ is known. Where **r** is the coordinates of the electron density.

The second theorem states:

- ‘For any particular $V_{ext}(\mathbf{r})$, the exact ground state energy, E, of the system is the global minimum value of this functional, and the density $n(\mathbf{r})$ that minimises the functional is the exact ground state density $n_0(\mathbf{r})$.[48] This implies that the functional $E[n]$ is sufficient to calculate the ground state properties.

The total energy of the system can be calculated from equation (2.1), minimising this equation with respect to $n(\mathbf{r})$ gives the ground state energy.

$$E_{Total}\left[n\left(\mathbf{r}\right)\right] = \int dr\nu(\mathbf{r})n(r) + F\left[n(\mathbf{r})\right] \tag{2.1}$$

where $F[n(\boldsymbol{r})]$ denotes the kinetic energy of electrons and the interactions between them, n is the density of electrons and v is the potential.

$F[n(\boldsymbol{r})]$ can be broken down into:

$$F\left[n(\mathbf{r})\right] = T\left[n(\mathbf{r})\right] + U\left[n(\mathbf{r})\right] \tag{2.2}$$

where $T[n(\boldsymbol{r})]$ is the kinetic energy of a system of non-interacting electrons whose distribution is $n(\boldsymbol{r})$, $U[n(\boldsymbol{r})]$ denotes the electron-electron interaction energy.

The electron-electron interaction can be broken down into the Hartree energy and the exchange correlation energy:

$$U\left[n(\mathbf{r})\right] = E_{Hartree}\left[n(\mathbf{r})\right] + E_{XC}\left[n(\mathbf{r})\right] \tag{2.3}$$

Therefore, the total energy can be written as:

$$E_{Total} = T\left[n(\mathbf{r})\right] + \int dr v(\mathbf{r}) n(\mathbf{r}) + E_{Hartree}\left[n(\mathbf{r})\right] + E_{XC}\left[n(\mathbf{r})\right] \tag{2.4}$$

where $E_{XC}[n(\boldsymbol{r})]$ is the only unknown variable in equation (2.4).

As $T[n(\boldsymbol{r})]$ is the kinetic energy, it cannot be minimised with respect to n and is therefore described in orbital form. Kohn-Sham proposed an indirect method to minimise the total energy:

$$0 = \frac{\delta E\left[n\right]}{\delta n\left(\mathbf{r}\right)} = \frac{\delta T\left[n\right]}{\delta n\left(\mathbf{r}\right)} + \frac{\delta V\left[n\right]}{\delta n\left(\mathbf{r}\right)} + \frac{\delta E_{Hartree}\left[n\right]}{\delta n\left(\mathbf{r}\right)} + \frac{\delta E_{XC}\left[n\right]}{\delta n\left(\mathbf{r}\right)} = \frac{\delta T\left[n\right]}{\delta n\left(\mathbf{r}\right)} + v_{external}(\mathbf{r}) + v_{Hartree}(\mathbf{r}) + v_{XC}(\mathbf{r}) \tag{2.5}$$

The external potential is a potential that is external to the electron-electron interactions and unlike $v_{Hartree}$ and v_{XC} it is not calculated through self-consistent methods. These potentials can be collected together to form an overall potential (v_{effect}) for a system of non-interacting electrons that affect the electronic system.

$$v_{effect} = v_{external} + v_{Hartree} + v_{XC} \tag{2.6}$$

This effective potential can be used in the Kohn-Sham equation to calculate the ground state density of the system through a self-consistent process.

$$-\frac{\hbar}{2m}\nabla^2 \psi_n\left(\mathbf{r}\right) + v_{effect}(\mathbf{r})\psi_n(\mathbf{r}) = \varepsilon_n \psi_n(\mathbf{r}) \tag{2.7}$$

v_{effect} is calculated from an initial estimate of the density, which is fed into equation (2.7) to produce $\varepsilon_n \psi_n$, and used to calculate a new density. This is repeated until convergence is reached. The ground state energy is obtained by removal of the double counting terms.

2.1.1 Exchange correlation assumptions

2.1.1.1 Local density approximation

The Local Density Approximation (LDA) uses the density calculated from a uniform electron gas to measure the exchange energy at a given **r**.[48] As the electron density is uniform, there is no **r** dependence on the value of the electron density.[49]

$$\delta E_{XC}[n] = \sum_{\sigma} \int dr \left[\varepsilon_{XC}^{homogeneous} + n \frac{\partial \varepsilon_{XC}^{homogeneous}}{\partial n^{\sigma}} \right]_{\mathbf{r},\sigma} \delta n(\mathbf{r},\sigma) \tag{2.8}$$

here ε is the energy per electron at point **r** and σ is the spin.

The uniform electron density means that the $E_{Hartree}$ part of the total energy can be calculated easily. The LDA method is limited to systems where there are slowly varying electron densities. This is due to the implemented method of breaking the system into small partitions, where the electron density varies little, thus allowing the uniform electron gas modell to be used. Nevertheless, it has been shown that the LDA method works well for surfaces,[49] where there are strong variations in the electron density.

2.1.1.2 Generalised gradient approximation

The Generalised Gradient Approximation (GGA) also uses the density of the uniform electron gas and also the addition of the gradient of the density distribution at given **r**.

$$\delta E_{XC}[n] = \sum_{\sigma} \int dr \left[\varepsilon_{XC} + n \frac{\partial \varepsilon_{XC}}{\partial n^{\sigma}} + n \frac{\partial \varepsilon_{XC}}{\partial \nabla n^{\sigma}} \nabla \right]_{\mathbf{r},\sigma} \delta n(\mathbf{r},\sigma) \tag{2.9}$$

This means that the dependence on the density becomes non-local and this gives a more accurate description of the changes occurring during bond formation/breaking.[49] This results in better agreement with experimental results for the ionisation energies and electron affinities of the elements.[50] Therefore, as this research involves the trapping of electrons, GGA is more suitable to be used in this work than LDA.

2.1.1.3 Hybrid functional

The need to improve the density functionals lead to the inclusion of exact exchange into the functional, leading to the formation of the hybrid functionals.

The formation of the hybrid functionals is through the evaluation of λ in equation (2.10).

$$E_{XC}[n] = \int_0^{e^2} \mathrm{d}\lambda \left\langle \psi_\lambda \mid \frac{\mathrm{d}V_{int}}{\mathrm{d}\lambda} \mid \psi_\lambda \right\rangle - E_{Hartree}[n] = \frac{1}{2} \int \mathrm{d}^3 r n(\mathbf{r}) \int \mathrm{d}^3 r' \frac{\bar{n}_{XC}(\mathbf{r},\mathbf{r}')}{\mid \mathbf{r}-\mathbf{r}' \mid} \tag{2.10}$$

where λ is a coupling constant and $\bar{n}_{XC}(\mathbf{r},\mathbf{r}')$ is the coupling constant averaged hole:

$$\bar{n}_{XC}(\mathbf{r},\mathbf{r}') = \int_0^1 \mathrm{d}\lambda n_{XC}^{\lambda}(\mathbf{r},\mathbf{r}') \tag{2.11}$$

In equation (2.10) if $\lambda = 0$, the energy is that of the Hartree-Fock exchange energy and if $\lambda = 1$, it is argued by Becke that either a GGA or LDA potential is most appropriate.[48] The value of the $E_{XC}[n]$ is approximated by a linear dependence on λ, when $\lambda \neq 1$ or 0, using a half and half form.[48]

$$E_{XC} = \frac{1}{2}\left(E_X^{HF} + E_{XC}^{DF}\right) \tag{2.12}$$

where E^{HF} is the energy of the Hartree-Fock exchange and E^{DF} is the energy of exchange-correlation from a density functional, either GGA or LDA.

The commonly used B3LYP hybrid functional mixes Hartree-Fock exchange, the exchange functional of Becke and the LYP correlation.[48] B3LYP defines the exchange-correlation energy as[48]

$$E_{XC} = E_{XC}^{LDA} + a_0\left(E_X^{HF} - E_X^{DF}\right) + a_X E_X^{Becke} + a_C E_C \tag{2.13}$$

where values of 0.20, 0.72 and 0.81 for a_0, a_X and a_C are commonly used, respectively.

The current computational cost of hybrid functional calculations means that they are too expensive for the system sizes used in this research. Therefore, GGA exchange-correlation has been used in this research.

2.1.2 Advantages of DFT

The main advantage of using DFT over Hartree-Fock (HF) is the electronic correlation energy. The correlation energy is generated through the interaction of a pair of electrons. The HF method only considers the correlation energy that is required by the Pauli repulsion energy.[48] Electron correlation is the reason for localisation or the delocalisation of electrons in a system, as well as, magnetism and dissociation of bonds.[48, 51] The correlation is therefore important in this work with the localisation of electronic charge by the defects.

The reduced computational cost of DFT is another advantage over HF,[52] allowing the large simulation cells used in the research. The computational cost of DFT calculations usually scales as N^3, while HF scales as N^6,[53] where N is the number of electrons in the system. This 10^3 difference in cost means that larger simulation cells can be simulated using DFT for the same computation cost. DFT codes have been developed that scale linearly with the number of electrons.[54, 55, 56]

2.1.3 Disadvantages of DFT

There are however, known issues that are present in DFT calculations, with some of these discussed below.

The size of the band gap of the system is underpredicted by the DFT method, usually be a factor of 50%.[57] This can be a problem if studying semi-conductors, where the band gap may be small and even zero, when studied via DFT. When defects are considered, the position of the defect level effects the properties of that defects. This means that the simulated spectrometry results from DFT are difficult be predict accurately, due to the incorrect position of the defect level in the band gap, such as optical spectra and ESR. The hybrid functionals of predict more accurately the band gap of a material by including the Hartree-Fock exchange. However, B3LYP still underpredicts the band gap of MgO. There are proposed corrections to this error in the literature[58] but due to the large band gap of MgO, these corrections were not required in this research.

The self interaction error present in the density functional results in the electron interacting with itself. This self interaction effects the modelling of charge localisation, magnetic materials and superconductivity.[48] There are ways of correcting for this self interaction in the literature, with the commonly used self interaction correction (SIC) or through using DFT+U.[48]

In DFT, the cohesive energy of a system is incorrectly described. The GGA functional underpredicts cohesive energy of the system and this results in lattice parameters larger than experimental results. This is because the atoms are not bonded as strongly to each other as they are in nature and therefore, the separation distance between the atoms increases. LDA, on the other hand, results in lattice parameters smaller than the experimental results. This is due to the fact that the cohesive energy is over predicted when using this exchange-correlation assumption.

2.2 Projector augmented waves

The Projector Augmented Waves (PAW) approach retains the full electron wave function. As the full wave function varies rapidly near the nucleus, all integrals are evaluated as a combination of integrals of smooth functions extending throughout space plus localised contributions evaluated by radial integration over muffin-tin orbitals.[48] This is achieved by defining the smooth part of a valence wave function $\psi'{}_i{}^{\upsilon}(\mathbf{r})$ and a linear transformation $\psi^{\upsilon} = T\psi'^{\upsilon}$ that relates the set of all electron valence functions $\psi_j^{\upsilon}(\mathbf{r})$ to the smooth functions $\psi_i'^{\upsilon}(\mathbf{r})$. The transformation is assumed to be unity except within a sphere centered on the nucleus, $T = 1 + T^0$, omitting the valence superscript.[48] Adopting the Dirac notation, the expression of each smooth function $|\psi>$ in partial waves m within each sphere can be written as:

$$| \psi' >= \sum_m c_m \mid \psi'_m > \tag{2.14}$$

with the corresponding all-electron function:

$$| \psi >= T \mid \psi' >= \sum_m c_m \mid \psi_m > \tag{2.15}$$

Hence the full wave function in all-space can be written as:

$$| \psi >=| \psi' > + \sum_m c_m \left[| \psi_m > - \mid \psi'_m > \right] \tag{2.16}$$

The transformation, T, involves the full electron wave function when the smooth functions of p’($\mathbf{r}$) is chosen:

$$T = 1 + \sum_m \left[| \psi_m > - \mid \psi'_m > \right] < p'_m \mid \tag{2.17}$$

2.3 Periodic boundary conditions

The VASP and CP2K computational codes both use periodic boundary conditions to simulate an infinite lattice. Bloch’s theorem states that in a periodic system each wave function can be written as the product of a cell-periodic part and a wavelike part.[59]

$$\psi_i(\mathbf{r}) = \exp[\mathbf{ik} \cdot \mathbf{r}] f_i(\mathbf{r}) \tag{2.18}$$

The cell-periodic component of the wave function can be expanded using a basis set consisting of a discrete set of plane waves, whose wave vectors are reciprocal lattice vectors of the crystal.

$$f_i(\mathbf{r}) = \sum_G c_{i,G} \exp[iG \cdot \mathbf{r}] \tag{2.19}$$

where G is the reciprocal lattice vector, defined by $G \cdot l = 2\pi m$, l is a lattice vector of the crystal and m is an integer. The wave functions can be written as a sum of plane waves.[59]

$$\psi_i(\mathbf{r}) = \sum_G c_{i,k+G} \exp[i(k+G) \cdot \mathbf{r}] \tag{2.20}$$

The description of the wave function from a small periodic unit, means only a small number of ions are needed to describe an infinite lattice. However, this comes at the cost of requiring larger k-point sampling.

2.4 Nudged elastic band

The minimum energy path is defined by the requirement that the force at any point be parallel to this path. So for any direction perpendicular to the path, $\mathbf{p}_s . \frac{d}{ds} \blacksquare_s = 0$, the potential energy on the atom is at a minimum:[60]

$$\mathbf{p}_s \cdot \nabla V(\blacksquare_s) = 0 \tag{2.21}$$

where $\mathbf{p}_s$ is a perpendicular path and $\blacksquare_s$ is the reaction path parametrised with reaction coordinate s.

The minimum energy path must be between two local minima. An “elastic band” is stretched between the reactant and product states, with a set of replicas of the system spread along this band. These replicas are used to describe a discrete transition path, turning the energy pathway into a series of minimisations.[60]

$$F\left(\mathbf{r}_1,\mathbf{r}_2,\ldots,\mathbf{r}_{P-1}\right)=\sum_{i=1}^{P-1}V\left(\mathbf{r}_i\right)+\sum_{i=1}^{P}\frac{kP}{2}\left(\mathbf{r}_i-\mathbf{r}_{i-1}\right)^2 \tag{2.22}$$

where $\mathbf{r}$ is the replicas along the path; the first sum is over the potential energy of all the replicas of the system, the second sum is a spring energy that connects adjacent images and P is the final configuration. The end point replicas ($\mathbf{r}_0$, $\mathbf{r}_P$) are fixed. The spring constant is arbitrary except that it scales kP to ensure convergence to the minimum energy path as more images are introduced into the chain, $P \to \infty$.[60]

The component of the net spring force on a replica parallel to the local path tend to keep the replica an equal distance from its neighbours; whereas the perpendicular spring force will tend to make it collinear with its neighbours. If the minimum energy path is curved, the perpendicular spring force will tend to pull the band off the minimum energy path, therefore causing corner cutting. The perpendicular component of the spring force is therefore zeroed.[60] The replicas also act on a force because of the gradient of the potential energy. The component of this gradient force perpendicular to the path acts to pull the replicas down toward the minimum energy path; whereas the parallel component tries to pull the replicas away from the saddle point, towards the end points. Therefore the parallel component of the gradient force is zeroed.[60] Moving each replica in the direction of its adjusted force until the adjustment force becomes zero will put the replicas on the minimum energy path, equally spaced in the $3N_P$ dimensional space.[60]

2.5 Gaussian plane wave code

CP2K is a periodic DFT code that uses Gaussian basis sets, as well as plane waves, to efficiently treat the electrostatic interactions, which leads to a linear scaling computational cost with system size.[61] The atom centred Gaussian type basis describe the wavefunctions, but uses an auxiliary plane wave basis to describe the density.[61] The Gaussian Plane Wave (GPW) representation of the Kohn-Sham energy is:

$$\begin{aligned}E[n] &= E_T\left[n\right]+E_V\left[n\right]+E_{Hartree}\left[n\right]+E_{XC}\left[n\right]+E_{II}\\
&=\sum_{\mu\nu}P^{\mu\nu}\left\langle\varphi_\mu\left(\mathbf{r}\right)\mid-\frac{1}{2}\nabla^2\mid\varphi_\nu\left(\mathbf{r}\right)\right\rangle+\sum_{\mu\nu}P^{\mu\nu}\left\langle\varphi_\mu\left(\mathbf{r}\right)\mid V_{loc}^{PP}\left(\mathbf{r}\right)\mid\varphi_\nu\left(\mathbf{r}\right)\right\rangle\\
&+\sum_{\mu\nu}P^{\mu\nu}\left\langle\varphi_\mu\left(\mathbf{r}\right)\mid V_{nl}^{PP}\left(\mathbf{r},\mathbf{r}'\right)\mid\varphi_\nu\left(\mathbf{r}\right)\right\rangle+2\pi\Omega\sum_{\mathbf{G}}\frac{\tilde{n}*\left(\mathbf{G}\right)\tilde{n}\left(\mathbf{G}\right)}{\mathbf{G}^2}\\
&+\int e^{XC}\left(\mathbf{r}\right)\mathrm{d}\mathbf{r}+\frac{1}{2}\sum_{I\neq J}\frac{Z_IZ_J}{\left|\mathbf{R}_I-\mathbf{R}_j\right|}\end{aligned} \tag{2.23}$$

here E_{II} is interaction energies of the ionic cores with charge Z_A and position $\mathbf{R}_A$, $P^{\mu\nu}$ is the density matrix, $\varphi_\mu\left(\mathbf{r}\right)=\sum_i d_{i\mu}g_i\left(\mathbf{r}\right)$ with $g_i(\mathbf{r})$ as a primitive Gaussian function and corresponding contraction coefficient $d_{i\mu}$, Ω is the volume of the unit cell, $\boldsymbol{G}$ are the reciprocal lattice vectors and $\tilde{n}\left(\mathbf{G}\right)$ is such that $\tilde{n}\left(\mathbf{r}\right)$ is equal to $n\left(\mathbf{r}\right)$ on a regular grid in the unit cell.[61]

2.6 DFT with dispersion

All semilocal density functionals and conventional hybrid functionals are unable to model the $\frac{1}{R^6}$ dependence of the dispersion interaction energy correctly.[62] This arises due to the charge fluctuations not being represented in density interactions, where the density functionals only consider the electron exchange and not the transition of density.[62] The lack of van der Waals (vdw) interactions in DFT mean that the species that only interact through vdw interactions, like noble gases and benzene rings, are incorrectly described. Therefore, methods to add vdw interactions into DFT have been proposed, such as the DFT-D3 methods used in this research.

The total energy of a DFT-D3 calculation is give by:

$$E_{DFT-D3} = E_{DFT} + E_{dispersion} \tag{2.24}$$

where E_{DFT} is the self consistent energy obtained using a normal density functional and $E_{dispersion}$ is the dispersion correction. The dispersion correction is the sum of two and three body terms.[62]

$$E_{dispersion} = E^{two} + E^{three} \tag{2.25}$$

The two body term is the dominant contribution to the dispersion energy and is calculated by equation (2.26).

$$E^{two} = \sum_{AB} \sum_{n=6,8,10,...} s_n \frac{C_n^{AB}}{r_{AB}^n} f_{d,n}(r_{AB}) \tag{2.26}$$

where the first sum is over all atom pairs in the system, C_n^{AB} is the average nth-order dispersion correction for atoms AB, r_{AB} is the separation distance between AB and s_n is a global scaling factor. For DFT-D3 n is truncated at n=8.[62] $f_{d,n}$ is a dampening function to prevent double counting at intermediate distances, the form of the damping function was proposed by Chai and Head-Gordon,[63]

$$f_{d,n}(r_{AB}) = \frac{1}{1+6(\frac{r_{AB}}{s_{r,n}R_0^{AB}})^{-\alpha_n}} \tag{2.27}$$

where $s_{r,n}$ is the order dependent scaling factor of the cutoff radii ${R_0}^{AB}$.

The dispersion correction is calculated using time dependent density functional theory (TD-DFT), using the Casimir-Polder formula[64] with the long range dispersion described using DFT by Gross *et al.*.[65] The value has been taken from the stable hydride of the elements (apart from noble gases) with the removal of the contribution from the reference hydrogen, for a consistent treatment of the dispersion.[62]

$$C_6^{AB} = \frac{3}{\pi}\int_0^\infty d\omega \frac{1}{m}[\alpha^{A_mH_n}(i\omega) - \frac{n}{2}\alpha^{H_2}(i\omega)] \times \frac{1}{k}\left[\alpha^{B_kH_l}(i\omega) - \frac{l}{2}\alpha^{H_2}(i\omega)\right] \tag{2.28}$$

where $\alpha(i\omega)$ is the average dipole polarisability at imaginary frequency ω, m,n,k,l are stoichiometric factors.[62] C_8 coefficient is calculated by:

$$C_8^{AB} = 3C_6^{AB}\sqrt{Q^A Q^B} \tag{2.29}$$

where

$$Q^A = s_{42}\sqrt{Z^A}\frac{\langle r^4 \rangle^A}{\langle r^2 \rangle^A} \tag{2.30}$$

$\langle r^4 \rangle$ and $\langle r^2 \rangle$ are multipole type expectation values from atomic densities which are averaged geometrically to get the pair coefficients. $\sqrt{Z}$ is the nuclear charge dependent factor and used to get consistent interaction energies.[62]

The three body term is calculated through

$$E^{three} = \sum_{ABC} f_{d,(3)}(\bar{r}_{ABC}) E^{ABC} \tag{2.31}$$

where $\bar{r}_{ABC}$ is used as a dampening function, f_d is as in equation (2.27) with α=16, s_r=$\frac{4}{3}$ and E^{ABC} is

$$E^{ABC} = \frac{C_9^{ABC}\left(3\cos\theta_a\cos\theta_b\cos\theta_c + 1\right)}{\left(r_{AB}r_{BC}r_{CA}\right)^3} \tag{2.32}$$

where the θ are the internal angles of the triangle formed from r_{AB}, r_{BC} and r_{CA}. C_9^{ABC} is the triple dipole term and calculated from

$$C_9^{ABC} = \frac{3}{\pi}\int_0^\infty \alpha^A\left(i\omega\right)\alpha^B\left(i\omega\right)\alpha^C\left(i\omega\right)d\omega \tag{2.33}$$

but approximated to[62]

$$C_9^{ABC} \approx -\sqrt{C_6^{AB}C_6^{BC}C_6^{CA}} \tag{2.34}$$

2.7 Potential alignment

The total energy of a system is ill defined due to the divergence of the electrostatic potential when periodic boundary conditions are applied to a system with a net charge. The calculated total energy (E) follows Janak's theorem, with the variation of the occupation of the highest occupied state.[57]

$$\frac{dE\left(n_i\right)}{dn_i} = e_i \tag{2.35}$$

where n_i is the occupation of the highest energy state i and e_i is the eigenvalue of the state.

The energy of the hole at the valence band maximum in a semiconductor host (H) with N electrons is obtained through:[57]

$$\lim_{N\to\infty}\left[E_H\left(N\right) - E_H\left(N-1\right)\right] = e_{VBM} \tag{2.36}$$

Equation (2.36) shows that the energy of a hole equals the eigenvalue of the valence band maximum in a infinite system. This fact means that the eigenvalue e_{VBM} can be used as a reference energy value for the electron reservoir,[57] so that

$$E_F = e_{VBM} + \Delta E_F \tag{2.37}$$

where E_F is the Fermi level and ΔE_F is the position of the Fermi level in the band gap of the material.

The average electrostatic potential within a cell is conventionally set to zero within the pseudopotential momentum-space formalism,[57] i.e. $V_{el}\left(G=0\right) = 0$, the eigenvalues are defined only up to an undetermined constant. For a neutral system the total energy is well defined, the total energy for a charged system depend on the same undefined constants as the eigenvalues.[57]

In order to obtain a physically meaningful formation energy, one can use the total energy calculated for which equation (2.35) holds and then correct for the undetermined offset by ensuring that the undetermined constant in $E_{D,q}$ and in e_{VBM} are consistent.[57] Therefore the relative positions of the average potential need to be restored in the calculations of the defect ($E_{D,q}$) and host (e_{VBM}).[57]

$$\Delta E_{pa}\left(D,q\right) = q.\Delta V_{pa} \tag{2.38}$$

where q is the charge and ΔV_{pa} is the potential alignment between the defect and host calculations.

In practice the atomic-site electrostatic potential (${V_D}^{\alpha}$) is used as a reference potential to make the serving potential. The potential alignment $\Delta V_{pa} = \overline{(V_D^{\alpha} - V_H^{\alpha})}$ is then determined as the average difference between $V_{D,q}^{\alpha}$ in the defect cell and the respective V_H^{α} in the host.[57]

2.8 Bader analysis

The definition of the electron density associated to a specific ion in a system is difficult, the output from a quantum mechanical calculation is a continuous electron density across the system.[66] A proposed method for assigning charge density is to divide the electron density into regions, known as a Bader region.

The gradient path, $\nabla\rho$, through the gradient vector field of charge density for a molecule can be obtained through the intergration of the differential equation,

$$\frac{d\mathrm{x}(s)}{ds} = \nabla\rho\left[\mathbf{x}(s)\right] \tag{2.39}$$

for some initial values $\mathbf{x}(0) = \mathbf{x}_0$.[Biegler-Konig] Alternatively, equation (2.39) can be expressed in terms of the path length, l.

$$\frac{d\mathbf{x}}{dl} = \frac{\nabla\rho(\mathbf{x})}{|\nabla\rho(\mathbf{x})|} \tag{2.40}$$

The essential topological properties of ρ can be summarised by the complete specification of its critical points, where $\nabla\rho = 0$.[Biegler-Konig] There are two types of critical points, at a nondegenerate critical point or a rank-three criticak point, $\mathbf{x}_c$. The Hessian matrix of $\rho, H(\rho) = [H_{ij}(\rho)]$, is of maximum rank,[Biegler-konig]

$$\det\left[H(\rho)\right]_{\mathbf{x}=\mathbf{x}_c} \neq 0 \tag{2.41}$$

with

$$H_{ij}(\rho) = \frac{\partial^2\rho}{\partial x_i \partial x_j} \tag{2.42}$$

Since $H(\rho)$ is of a rank less than three at a degenerate critical point, $\det[H(\rho)]$ vanishes. At nondegenerate point, $\mathbf{x}_c$ is further characterised by it signature σ, defined as the excess number of positive over negative eigenvalues of $H(\rho)_{\mathbf{x}=\mathbf{x}_c}$. Therefore, a nondegenerate critical point is one of the types (3,σ) where σ = -3, -1, +1, +3 amd the first number within the parentheses denotes its rank.[Biegler-konig]

A (3,-3) critical point exhibits the properties which define an attractor of the gradient vector field of the charge distribution: a closed subset $A \subset R^3$ is an attractor of $\nabla\rho$, if and only if

1. it is inveriant to flow of $\nabla\rho$,
2. any trajectory whose origin lies in A is contained in A,
3. there exists an open variant neighbourhood B of A such that any trajectory originating in B terminates in A.

The largest neighbourhood B_{max} satisfying this condition is called the basin of A.[Biegler-konig]

The Only closed subset of R^3 exhibiting these properties are the singletons determined by the local minima in the charge distribution which occurs at the position of the nuclei. The nuclei act as the attractors of the gradient vector field of $\rho(\mathbf{x})$. The result of this identification is that the space of the molecular charge distribution in real space is partitioned into disjointed regions, the basins, each if which contains one and only one point attractor or nucleus. An atom, either free or bound, is defined as the union of an attractor and its associated basin.[biegler-konig]

Chapter 3

MgO and zirconolite - Previous research

In this chapter the previous research of MgO and zirconolite will be discussed. The MgO results discussed will focused on the formation energies of the defects and their mobility, from both experimental and theoretical studies in the literature. These results have been focused on as it will allow a comparison to the results generated in the research. The research into zirconolite discussed here gives an overview description to the material behaviour. This overview is important as there is less detailed research into defects in zirconolite, so the trends observed in the literature are used to judge the accuracy of the DFT results.

3.1 Magnesium oxide

Magnesium oxide (MgO) is considered a model oxide system due to the binary composition and the face-centred cubic (fcc) crystal structure of the compound. In addition to this, experimentally MgO can be synthesised in many different morphologies, such as powders, thin films, single crystals and nanoparticles.[46]Therefore, unsurprisingly, there has been a large number of studies performed on MgO, both experimentally as well as theoretically. However, the oxygen vacancy has received significantly more attention than the other types of defect present in MgO due to the difficulty in observing the interstitial defects[67] and its importance to catalytic processes.

3.1.1 Experimental vacancy migration barriers

The migration barriers of oxygen vacancies have been investigated using the incorporation of gases O^{18} into an MgO crystal. Oishi and Kingery performed this experiment in 1960 using a MgO grain obtained from a low purity MgO single crystal.[68] This experiment gave a migration barrier of 62.4 kcal mol^{-1} (2.71 eV). This migration barrier is in agreement with later experiments by Hashimoto *et al.* on polycrystalline MgO. These experiments were performed between 1050 - 1438°C at 40 Torr. The barrier observed using the polycrystalline MgO was 60.2 kcal mol^{-1} (2.61 eV).[69] Shirasaki and Hama also calculated the migration barrier of oxygen vacancies using polycrystalline MgO across a similar temperature range to Hashimoto *et al.*. The observed barrier in this range was 55.8 kcal mol^{-1} (2.42 eV).[70] Yoo and Wuensch obtained a higher migration barrier of 3.24 ± 0.13 eV for the oxygen vacancy,[71] which is higher than the earlier results. Yoo and Wuensch's sample was a single crystal of MgO^{18} grown on a substrate before being cold-pressed into a pellet prior to annealing the sample. This migration barrier value appears too large compared to the previous result and may be caused by the annealing, which could have removed the surface defects and prevented the dissolution of the O^{18} out of the surface. The presence of vacancies may play an important part in the ecjection mechanism of O_2 from the surface. From the literature, Vieira and Brook have compiled a table of migration barriers of oxygen vacancies in MgO measured using different techniques.[71] The published oxygen vacancy migration barriers using tracer diffusion are in the range 282 - 344 kJ mol^{-1} (2.36 - 3.57 eV),[71] with anomalous values of 126 ± 13 kJ mol^{-1} (1.31 eV),142 ± 16 kJ mol^{-1} (1.47 eV), 178 ± 21 kJ mol^{-1} (1.84 eV) and 430 ± 42 kJ mol^{-1} (4.46 eV).[71] The previous values for the oxygen vacancy diffusion fall into this range of values published by Vieira and Brook,[71] but the large range of these values shows that the sample preparation can have a dramatic effect on the mobility of defects. The diffusion of the Mg vacancies has received less attention than the O vacancy. Sempolinski and Kingery observed a value of 2.28 ±0.21 eV through ionic conductivity.[72] This value is in agreement with the 2.2 eV observed by Duclot and Deportes, using the dilatocoulometric method.[73] These diffusion barriers are smaller than the previously reported barrier by Wuensch *et al.* (2.76 ± 0.08 eV in a MgO single crystal).[74] Vieira and Brook have also compiled a table of Mg vacancy migration barriers, as they did for the oxygen vacancy.[71] The tabulated results appear to fall into two ranges, from 150.6 - 173.6 kJ mol^{-1} (1.56 - 1.80 eV) and 308 - 339.9 kJ mol^{-1} (3.19 - 3.52 eV).[71] These samples are all monocrystals with the diffusion observed with an Mg^{28} isotope. The difference between these samples appears to be the amount of impurities in the MgO sample. The previously observed barriers all lie between these two ranges. This shows that there is no consistent value for the diffusion barrier of the magnesium vacancies from experimental investigations.

3.1.2 Experimental defect formation energies

The Schottky formation energy (E_S) has been measured by Narayan and Washburn using the shrinkage rate of dislocation loops on large polycrystalline samples.[75] Narayan and Washburn obtained an E_S of 3.6±0.22 eV, using the activation barrier of the F^{2+} vacancy observed by Oishi and Kingery.[68] This value of E_S is in excellent agreement with the earlier result obtained by Harding *et al.* who calculated an E_S of 3.4±0.2 eV.[76] These values for E_S are smaller than those predicted by Wuensch, who than suggests the value of E_S in MgO is in excess of 4.5 eV.[77] Wuensch's value is supported by Oishi and Ando who, using oxygen self-diffusion in an undoped MgO sample and values from Gourdin and Kingery[78] as well as simulations of Mackrodt, calculated an E_S of 5.8 eV.[71] This value of E_S is smaller than that measured by Gourdin and Kingery (7.7 eV).

3.1.3 Electron spin resonance

Electron spin resonance (ESR) has been used to understand the structures of the magnesium and oxygen vacancies in MgO, that involve an unpaired electron, the V$^-$, V^0, F$^+$ and F^0 vacancies, respectively. Halliburton *et al.* investigated the V$^-$ defect at room temperature formed by irradiating the MgO sample with X-ray, γ and neutron irradiation. The vacancy gave rise to one signal, with g factors of $g_\perp$ = 2.0385 and $g_\|$ = 2.0032. The presence of one signal implies that the hole was localised on one oxygen ion, with no preferred orientation over the principal axis in MgO.[79] Above 200 K, the width of the V$^-$ ESR signal has an extra contribution other than thermal broadening and this is assigned to the delocalisation of the hole and hopping over the 6 oxygen ions surrounding the vacancy.[79] Rose and Halliburton studied the V^0 vacancy and found that the spin state of this defect is S = 1, signifying a triplet state configuration for the defect.[80] The analysis was performed at 77 K and allowed the hyperfine structure to be observed caused by the Mg^{25} ions next to defective O$^-$ ions. The splitting caused by the axial and equatorial positions can be distinguished by rotating the magnetic field through the defect axis, resulting in a shift in the equatorial splitting while the axial remained constant.[80] The hyperfine structure supports the model proposed by Wertz in 1959 for the two holes to localise on oxygen ions on opposite sides of the vacancy.[80] The Wertz model was based on the $3\cos^2\theta$ law, that implied that the two holes must be trapped at the same vacancy site and that the holes are along a common axis as the holes would repel one another.[81] Wertz *et al.* identified that the V^0 is not as stable as the V$^-$ vacancy, as there were no V^0 vacancies when the sample was irradiated at room temperature instead of at liquid nitrogen temperatures.[81] Wertz *et al.* had previously studied oxygen vacancies formed by heating MgO in Mg vapor to produce a large number of F^+ vacancies in the crystal.[82] The observed ESR line has g = 2.0023, with hyperfine structure if the vacancy has Mg^{25} neighbours.[82] The single g factor shows that the electrons associated with this defect are trapped inside the vacancy, as the spherical symmetry will not be broken into $g_{\perp}$ and $g_{\parallel}$ components. Sterrer *et al.* have found that the same trapping occurs at the surface of MgO. The defects were created by bombardment of the sample with 100 eV electrons. The samples were then analysed using both ESR and STM to gain an accurate description of the geometric properties of the vacancy on the surface by using the principle component of the g tensor.[83]

3.1.4 Simulated defect migration barriers

3.1.4.1 Interatomic potentials

DFT, semi-empirical and interatomic potential calculations have been used to calculate the migration barrier of defects in MgO, using either the constrained minimisation or nudged elastic band (NEB) techniques. Busker *et al.* used Buckingham potentials to study the doubly-charged defects of MgO. The potentials were fitted to the lattice parameters, elastic and dielectric constant, for fully charged and partially charged (±1.7e) systems with the shell model.[84] The migration barrier calculated for the doubly charged oxygen (F^{2+}) vacancy is 2.12 eV using the fully charged model and 1.56 eV for the partial charge model.[84] The fully charged barrier is in better agreement with the experimentally observed barrier for this vacancy, while the partially charged model differs by 35.5% from the experimental value. There is a similar difference between the barriers calculated for the Mg vacancy (V^{2-}), with a barrier of 2.08 eV for the fully charged potentials, and 1.53 eV for the partially charged potentials.[84]The barriers of the vacancies predicted by the different potentials are similar because of the migration pathways the vacancies take. The interstitial migration barriers were also calculated using these different potentials. The difference in the predicted barrier heights was not so significant. The O^{2-} interstitial migration barriers were calculated to be 0.58 eV and 0.47 eV, while the Mg^{2+} interstitial migration barrier was 0.64 eV and 0.46 eV using the fully and partially charged models, respectively. In 2005 Uberuaga *et al.* used Buckingham potentials to study the same defects using the interatomic potentials derived by Lewis and Catlow,[85] which is a fully charged model. The migration barrier was calculated using the NEB method and resulted in a barrier height of 2.00 eV and 2.12 eV for the F^{2+} and V^{2-} vacancies, respectively.[86] These calculated barriers are in good agreement with those calculated by Busker *et al.* when using the fully charged model and the experimental results for the F^{2+} vacancy. Although the vacancy barrier heights are in agreement with these two different potentials, there is a difference when considering the migration of the interstitials. Uberuaga *et al.* has calculated migration barriers of 0.40 eV and 0.32 eV for the O^{2-} and Mg^{2+} interstitials, respectively.[86]The lower barriers calculated by Uberuaga *et al.* could be due to the NEB method implemented to calculate the pathway. As the NEB method optimises the pathway, allowing full relaxation of the saddle point, unlike the method used by Busker *et al.*, it may find a lower energy saddle point.

3.1.4.2 Semi-empirical method

Kotomin and Popov used semi-empirical methods to investigate the diffusion of the oxygen vacancies in different charge states in a 223 atom cluster, using the constrained minimisation technique by fixing the oxygen between the two vacancies along the (110) axis.[87] The semi-empirical method is based on the formulation of Hartree-Fock (HF) and the shell model pair potential. The migration barrier calculated for the F^{2+} vacancy is 2.50 eV, which is higher than that predicted by the interatomic potentials but is in better agreement with the range observed from experiments. This computational technique allows different charge states to be studied, and therefore the migration barriers of the oxygen vacancies with one (F^+) and two (F^0) electrons localised in the vacancy. The migration barrier of the F^+ vacancy was calculated to be 2.72 eV. Therefore, the localised electron results in an increase in the migration barrier of 0.22 eV. Localisation of another electron results in a migration barrier of 3.13 eV, with the second electron resulting in a 0.41 eV increase in the barrier height.[87] There is no explanation as to why the introduction of a second electron causes an increase in the barrier height which is almost double that of the increase caused by one electron. There has been no experimental investigation of the diffusion of the oxygen vacancy with trapped electrons, so there is no way of assessing the accuracy of these semi-empirical calculations. The calculated migration barrier for the V^{2-} vacancy was 2.43 eV,[87] which is also higher than predicted by the empirical potentials. This technique was also used to calculate the migration barriers of the interstitial defects in MgO. The lowest energy pathways for both doubly-charged interstitial species was the ion exchange mechanism, which involves the interstitial moving in the <111> plane and pushing the lattice ion into the new interstitial position while the interstitial takes the lattice site. The migration barrier for the Mg^{2+} interstitial is 0.43 eV.[87] This migration barrier is in agreement with the results obtained by Uberuaga[86] and Busker *et al.*[84] through potentials, which shows that the empirical potentials can give a good description of defects in MgO. The O^{2-} interstitial is also in agreement, with the migration barrier calculated to be 0.54 eV.[87] The ${O_2}^{2-}$ interstitial diffusion barrier was also calculated by Kotomin and Popov using two different methods, a 16 atom supercell using the HF method and a full-potential linear-muffin-tin-orbitals (FP LMTO) method based on the local density approximation (LDA). The calculated barrier is 1.45 eV for the LMTO method and 2.3 eV by the HF method.[87] The difference between the computational methods is accounted for by the difference in simulation cell size and the number of surrounding ions able to relax. However, both simulations found that the ${O_2}^{2-}$ interstitial has an interesting diffusion pathway, involving the rotation of the dumb-bell and diffusion along the cube face. The <111> oxygen dumb-bell rotates to a <110> dumb-bell, with a barrier of 0.09 eV (HF) or 0.15 eV (LMTO). The dumb-bell then breaks and the interstitial then diffuses along the <110> face, with a migration barrier of 2.3 eV (HF) or 1.45 eV (LMTO). The interstitial oxygen then continues along the <110> face until it forms a <110> dumb-bell with another lattice oxygen, which then rotates back to the <111> dumb-bell with the same barriers as before.[87]

3.1.4.3 Density functional theory

The migration barrier of the doubly-charged defects has also been studied through DFT using the LDA. The migration barrier of the V^{2-} vacancy is calculated to be 2.20 eV, which has a smaller migration barrier than calculated for the F^{2+} vacancy of 2.31 eV.[88] The F^{2+} migration barrier is smaller than that calculated by the semi-empirical method[87] but larger than those calculated by classical methods. [86, 84]The reason for the lower migration barrier calculated using DFT than the semi-empirical result could be due to the small simulation cell used by Kotomin and Popov. The doubly-charged interstitials have also been studied using two different sized simulation cells, with three different pathways investigated. The lowest energy pathway for the Mg^{2+} interstitial was found to be the <111> ion exchange pathway, in support of the results obtained through classical results, with a barrier height of 0.83 eV (54 atom cell) and 0.71 eV (128 atom cell).[88] This results shows that the amount of relaxation in the surrounding ions has a significant effect on the migration barrier. The migration barrier of 0.71 eV is significantly higher than the barrier calculated using other computational methods. Whilst the O^{2-} interstitial migration barrier is calculated to be 0.59 eV and 0.44 eV in the 54 and 128 cells, respectively, this agrees with the other computational methods. The barriers calculated by Kotomin and Popov and Uberuaga *et al.* found that the Mg^{2+} interstitial should be more mobile than the O^{2-} interstitial, which disagrees with the results of Gilbert *et al.*[87, 86] The Gilbert *et al.* migration barrier is supported by the fully charged model used by Busker *et al.*, whilst the partial charge model predicts the two interstitials to have equal migration barriers.[84]

3.1.5 Defect formation energies

3.1.5.1 Interatomic potentials

The formation energy of the different defects in MgO have been calculated using different computational methods. Mackrodt and Stewart calculated the Frenkel pair defect energies (E_{FP}) for both constituents, as well as the Schottky energy (E_S) using classical potentials. The calculated E_{FP} for the oxygen pair is 15.2 eV, which is higher than the energy of the magnesium pair, 11.9 eV.[89] The E_S was 7.5 eV, which shows that the formation of the Schottky defect is favoured over the formation of the Frenkel pairs in MgO. The formation energies of the F^{2+} and the V^{2-} vacancies were also calculated. The formation energy of the F^{2+} vacancy was calculated to be 22.9 eV. This is more stable than the V^{2-} defect which has a formation energy of 25.4 eV.[89] Interpretation of these results shows that the Mg interstitial is significantly more stable than the O interstitial. Earlier calculations from Catlow *et al.* using different parameters found different defect stabilities, with the Mg and O Frenkel pairs having similar formation energies, 12.4 eV and 12.1 eV, respectively.[90] The results from Catlow *et al.* suggest that the O Frenkel pair is more stable than the Mg pair, which disagrees with the results from Mackrodt and Stewart. Also, the order of stability of the isolated vacancies is different for these two sets of interatomic potentials, with the V^{2-} vacancy (23.8 eV) more stable than the F^{2+} vacancy (24.7 eV).[90] However, the calculated E_S agree, as Catlow *et al.* calculated a value of 7.7 eV, which compares with Mackrodt and Stewart's value of 7.5 eV. This shows that the differences in the vacancy stability cancels out when the values are combined to calculate E_S. The value of E_S is supported by the recent results of Gilbert *et al.* who calculated the E_S using classical potentials, with the vacancies separated by different distances. Gilbert *et al.* calculated a value of 7.2 eV at the largest separation distance considered (3^{rd} nearest neighbour), in agreement with previous results, while the E_S decreased to 5.7 eV when the vacancies are next to each other.[88] The effect of the simulation cell on E_S was investigated by Vočadlo *et al.*, who calculated E_S using different periodic simulation cells and found that the size of the cell had little effect on the value obtained for E_S. The value of E_S in the largest cell (256 ions) was 7.53 eV, whilst in the smallest cell (32 ions) the value was 7.26 eV.[91] Both values are in agreement with the other results calculated using interatomic potentials. Vočadlo *et al.* also calculated E_S as a function of temperature in the simulation cell of 108 ions. The temperature was increased from 0 K to 1000 K, resulting in a decrease of E_S from 7.43 eV to 6.96 eV.[91] This indicates that E_S has no significant dependence on temperature in the range studied in this work. Busker *et al.* used the two different potentials to calculate the formation energies of the different defects in MgO. The partial charge model resulted in significantly lower formation energies than those predicted by the fully charged model. The method of calculating E_S also had a significant effect on the value obtained, with 8.44 eV using the fully charged potentials when calculating E_S from isolated vacancies but 5.35 eV when the vacancies are next to each other. This compares to values of 6.12 eV and 3.90 eV for the partially charged model.[84] These values are significantly different from the previous result, with the isolated values from the fully charged model being too high and the vacancy pair being lower than the previous value. The calculated Frenkel pair energies (E_FP) by Busker *et al.* show that the Mg pair is more stable than the O pair, which is in agreement with earlier results from Catlow *et al.* but higher in energy, with the Mg E_{FP} being 13.35 eV and 9.58 eV, and the O E_{FP} being 13.81 eV and 9.95 eV, for the fully and partially charged models, respectively. The similarity in formation energy of the two Frenkel pairs is also in agreement with the results from Catlow *et al.* and supports this conclusion over the conclusion of Mackrodt and Stewart. Kittiratanawasin *et al.* recently calculated the Frenkel pair formation energies using Ewald summation and the Fast Multiple Method (FMM) to assess the effect of periodic boundary conditions on the calculated value. These two methods give the same formation energies for both the Mg and O Frenkel pairs when the defects are separated by the nearest neighbour, with values of 11.8 eV and 11.9 eV, respectively.[92] Therefore, the results of Kittiratanawasin *et al.* agree with the earlier conclusion that the formation of Frenkel pairs is similar for both species in MgO. When the defects are separated by 3 nm a difference appears between the calculation methods, with the Ewald summation predicting more stable defects. At the larger separation distance the value for the Mg pair are 13.5 eV and 13.3 eV and for the O pair are 13.1 eV and 12.8 eV for the FMM and Ewald summation, respectively.[92] These results predict that the oxygen Frenkel pair is more stable than the Mg pair at these separations but it is still consistent with the prediction that the Frenkel pairs have similar energies in agreement with the results of Catlow *et al.* and Busker *et al.*[90, 84]

3.1.5.2 Density functional theory

DFT has also been used to calculate the formation of defects in MgO, with Gilbert *et al.* calculating the Frenkel and Schottky defect energies. The calculated E_S is lower than that calculated by the interatomic potentials, with Gilbert *et al.* obtaining value of 5.97 eV in the 180 ion simulation cell.[88] The reason for the lower E_S is due to LDA tending to under predict the cohesive energy, making it easier to remove the MgO unit. The DFT results support the prediction of Mackrodt and Stewart in that there is a difference in the stability of the Frenkel pairs, with the Mg pair being the more stable. Gilbert *et al.* give values for Mg E_{FP} of 10.35 eV and O E_{FP} of 12.17 eV. Again, these values are lower than the results from the interatomic potentials and this is due to the lower charge on the ions in DFT than in the potentials, although the DFT results are higher than the partially charged model of Busker *et al.*, suggesting that these potentials were not correctly fitted for the partially charged model. De Vita *et al.* also used LDA to study the energetics of defects in MgO, including the Schottky defect energy using 16 and 32 ion supercells. The calculated E_S values were 7.78 eV and 6.88 eV for the 16 and 32 ion cells, respectively.[93] These values are significantly higher than those calculated by Gilbert *et al.* and may be due to the smaller simulation cell used in the study by De Vita *et al.*, although De Vita *et al.* claim that convergence tests showed that the defect formation energy quickly converges with the system size. The difference may also be caused by De Vita *et al.* accounting for defect interaction through the periodic repeat while Gilbert *et al.* did not. Accurate quantum Monte Carlo (QMC) calculations have been used by Alfè and Gillan to calculated E_S in MgO, as well as DFT. The calculated DFT result was 6.76 eV using the LDA exchange energy.[93] This value agrees with the earlier DFT result of De Vita *et al.* and shows the value from Gilbert *et al.* to be too low. AlfΓ and Gillan used a simulation supercell of 1024 ions and found that the value for the 54 ion cell was within 0.2 eV.[93] A 54 ion cell was used for the QMC with 50,000 steps. The result from the QMC was 7.5±0.53 eV, which is higher than the E_S calculated by other computational methods, but the confidence range brings it in close agreement with the DFT results.[93]

3.1.6 Comparison between experimental and simulated results

There is good agreement between the different computational methods and the experimental results for the migration barrier for the oxygen vacancy, although the classical potentials generally predict that the barrier to be smaller than those given by experiments. The simulated vacancy migration supports the value of 2.2 eV for the V^{2-} migration observed by both Sempolinski and Kingery, and Duclot and Deportes. However, there is a large discrepancy between the experimental and simulated value for E_S. The simulated value for E_S depends on the method used but predicts that the value is around 7 eV. The early experimental results give a value of 3.5 eV. Although a later experiment gives a value of 5.8 eV, there is still a large and significant difference for the value of E_S. The experimental results are implied from the vacancy diffusion barrier and the simulations show that this method gives the wrong defect stabilities.

3.2 Zirconolite

Zirconolite is the proposed encapsulation matrix for the disposal of Pu by the NNL. Zirconolite has the ability to be used in a number of different waste systems, such as SYNROC, glass ceramics or as a single phase matrix. In all these systems, zirconolite is the main Pu-bearing phase and will therefore be subjected to an increased proportion of the damage sustained in the waste form. Zirconolite has received much attention due to natural analogues that have a high concentration of U and Th. These natural analogues have shown that zirconolite is able to retain actinide species within the structure in an amorphous state, as concentrations of U and Th of 14 wt% and 20 wt% have been found in samples dated to 2.5 billion years old, respectively[11]. This evidence supports the case for the use of zirconolite as an encapsulant; it shows that it can retain Pu as well as the decay products and prevent a distribution into the biosphere. However, these natural analogues have different properties to those of the synthesised zirconolite, with a superior leach rate and radiation resistance, which may be due to the heat treatment the natural analogues have been subjected to. The history of these natural samples is difficult to identify and therefore to replicate on the synthesised samples. The superiority of the leach rate of ceramics over that of glasses is an important part of their interest. Zirconolite has an interesting leach rate property, in that unlike most ceramics where the leach rate increases as the lattice structure becomes amorphous,[15] the leach rate of zirconolite only increases slightly when in an amorphous state compared to the crystalline solid.[94] This has significant implications as the waste form is required to retain the actinide species for up to one million years and it is expected that the host will become amorphous after several hundred years.[95] Therefore, the performance of the waste form in the amorphous state is of significance as for the majority of the time spent in the geological disposal facility (GDF), the structure will be in an amorphous state. The ease of synthesising zirconolite is also one reason behind the NNL favouring it as an encapsulation matrix, as oxides only need to be mixed and heated to form the structure. This means that an automated process can be established, which will reduce the cost of the waste package as the amount of protection needed for staff is reduced. The cost of the waste form is an important contribution due to the amount of Pu that needs to be disposed (currently 100 tonnes in the UK).[96]

3.2.1 Ion beam bombardment studies

The capability of zirconolite to act as an encapsulant has been studied through various experimental techniques. These different techniques allow for the different properties of the waste form to be examined and assessed. Ion beam studies have been performed to simulate the effect of an α recoil event. Many different ion beams have been used to study zirconolite such as Ar, Kr and He ions with various energies.[97, 98, 11] Wang *et al.* have found that bombardment with 1 MeV Kr ions leads to the transformation of the zirconolite crystal structure from monoclinic to cubic pyrochlore, observed via X-ray diffraction (XRD) spot shifts. At higher ion bombardment rates, the structure will convert again to a defect fluorite structure, before becoming fully amorphous.[98] The change in crystal structure is partially supported by the work of Gilbert *et al.* using 2 MeV Kr bombardment which caused the formation of an amorphous region of around 1.1 μm.[11] The bombardment also leads to the formation of a crystalline interface region between the amorphous and undamaged zirconolite crystal, with XRD indicating that it has a different crystal structure to that of zirconolite but it was not assigned. However, when Ewing and Wang[99] bombarded an annealed sample of natural zirconolite with 1.5 MeV Kr ions only a ThO_2 phase was observed, which formed during the annealing process, with the zirconolite becoming amorphous. This difference in behaviour may be due to the fine polycrystalline structure of the annealed sample; the small grains are not large enough to accommodate the new phase along with the amorphous region, as was the case for the Gilbert *et al.* sample. The He ion bombardment does not result in the creation of a new phase as with the Kr irradiation, owing to the smaller energy transferred into the structure for He implantation. Zirconolite was bombarded with 200 keV He ions and only induced visible damage when the flux was at 1×10^{17} cm^{-2}. At this flux, He accumulates but does not amorphorise the structure. This accumulation of He occurs at a depth of 550-750 nm from the undamaged surface.[11]

3.2.2 X-ray diffraction experiments

XRD has been used to determine the evolution of the zirconolite structure after irradiation as well as confirmation of the synthesis of loaded zirconolite. The Pacific Northwest National Laboratory (PNNL) used the technique to show that a phase pure zirconolite was synthesised when loaded with Pu, U and Hf. The XRD patterns also showed the formation of $HfTiO_4$ and the presence of unreacted TiO_2.[9] The time-resolved XRD patterns show that when the monoclinic structure expanded, due to the radiation damage, the expansion occurs predominantly along the *c*-axis. This swelling is in agreement with the work of Wald and Offerman[100] and Strachen *et al.*[101] who previously observed such behaviour. In the PNNL study the zirconolite crystal became amorphous after 741 days after receiving a dose of 2.6 x 10^{18} α g^{-1}. However, when a loaded mixed ceramic is studied (comprising of zirconolite, pyrochlore, brannerite and rutile) the zirconolite structure can still be observed in the XRD patterns taken 960 days after accumulating a dose of 5 x 10^{18} α g^{-1}.[9] The extended survival of the zirconolite crystal in the mixed ceramic is due to the zirconolite crystal incorporating less Pu than the loaded single phase; the zirconolite is in competition with the pyrochlore phase to host the Pu. Therefore the structure obtains the dose at a slower rate, allowing more recovery in the mixed ceramic zirconolite. Sinclair and Ringwood studied natural zirconolite samples using XRD and found that zirconolite retains a high degree of lattice order, even after an irradiation dose, which would be equivalent to 10^6 years for zirconolite as a component of SYNROC.[102] The studied zirconolite showed interesting recovery pathways as samples were initially amorphous but upon heating to 800˚C a cubic defect fluorite pattern was observed. The monoclinic structure was obtained after heating to 1200˚C, although the pattern was reported to be simplified when compared to synthetic zirconolite.[102] These results show that the recovery goes through a two-stage process and may indicate that a similar process happens when the damage is created. Such a process was observed by Wang *et al.* when ion beam irradiation was used. The XRD pattern as a function of dose has been studied and indicates that the angle between (0 0 2) and (6 2 0) directions has increased from 81˚ to 90˚, which is interpreted as the β angle changing from 100.5˚ to 90˚. This leads to the unit cell vectors becoming equal to 11.6 Å as calculated from the ratio between *d* spacings.[103] Upon further irradiation the crystal becomes amorphous. Analysing the diffraction peaks as a function of dose, Wang *et al.* predicted that the amorphisation sequence is: zirconolite, pyrochlore, fluorite and then amorphous.[103] This pattern has been observed previously by Smith *et al.*[104] and Ewing and Headly.[105] Clinard *et al.* found that during a bombardment of between 0.4 and 1.0 x 10^{25} α m^{-3}, the zirconolite structure could be described more accurately by using either rhombohedral or hexagonal symmetry than monoclinic, before becoming amorphous at higher doses.[14] However, the sequence is challenged by more recent studies, PNNL observed no such transition in the XRD patterns, with no (311) pyrochlore peak appearing. Also, Clinard *et al.* found that no disordered cubic phase was detected between the hexagonal to amorphous structures.[14]

3.2.3 Electron diffraction studies

Clinard *et al.* found, using electron diffraction, that a dose of 6.1 x 10^{25} α m^{-3} accumulated over 460 days was needed to amorphorise the fully substituted Pu zirconolite ($CaPuTi_2O_7$).[14] The results obtained in this study were used to confirm the accumulation of an alpha recoil tracks model for damage progression. This model describes four stages in damage production, the first consists of isolated damaged tracks in a crystalline structure. The second stage is reached when these tracks overlap with each other. Stage three is reached when the majority of the structure is in a damaged/amorphous state, and finally when the structure becomes diffraction amorphous stage four is obtained. The effect of temperature on swelling was also studied in this work, with the swelling saturated at 5.4 vol% for this loaded zirconolite at room temperature. The swelling decreased to 4.3 vol% when the temperature rose to 575 K, requiring 50% more damage to reach the saturation limit, while at 875 K only 0.4 vol% swelling occurred due to the sample remaining crystalline.[14]

3.2.4 X-ray absorption studies

X-ray absorption studies (XAS) have been used to study the coordination of ions within the zirconolite surface, using both XANES (X-ray absorption near edge structure) and EXAFS (extended X-ray absorption fine structure) techniques. These experiments were performed at a grazing angle of below 3.4° to make the technique more surface sensitive. An amorphous region (1000 nm thick) was created in a thin film of zirconolite using 2 MeV Kr ions at room temperature. The structure of the XANES pre-edge of the amorphous region in the synthesised zirconolite appears very similar to that of a natural zirconolite sample.[106] However, there are clear differences when the grazing angle is increased to 45°, which examines the bulk sample. This indicates that ion beam irradiation produces the same surface damage as that of natural samples, which can be used to defend the use of accelerated damage samples for use in leaching experiments. Reid *et al.* used a grazing angle of 1.10° and 2.10° to observe the 5- and 6-fold coordinated Ti polyhedra, respectively. These angles show a majority of 5-fold coordinated Ti polyhedra in the damaged region of the synthetic and natural zirconolite compared to the 6-fold coordinated Ti. This result is a reversal of that obtained in the pristine sample, where 6-fold coordinated Ti polyhedra are favoured.[106] These results confirm that the Ti environments are accurately reproduced during ion beam bombardment compared to those produced through U and Th decay.

3.2.5 Leaching tests

The proposed use of zirconolite in the geological disposal facility (GDF) is as the first barrier and introduces a barrier for release, which will slow the rate at which the actinide species can leave the repository. Therefore, studies have been performed to measure the rate at which species are leached from the waste form. Two techniques are used to study the leach rate. The first is a static method which involves the sample being placed in a solution and measurements made over the time frame. The other technique is the flow technique and uses a flow of solution through the experiment, which prevents a build-up of a saturated solvation sphere around the sample and is a more accurate description of the process in the respository. Weber *et al.* used the static method to study the effect of radiation damage on the leach rate of zirconolite. The samples were submerged in deionised water at 90°C for 14 days.[94] The leached species were measured by inductively coupled plasma (ICP) emission and radiochemical analysis. An increased leach rate is reported for the amorphous zirconolite compared to the crystalline sample based on the normalised elemental weight loss. The amount of Ti in the solution for both samples was below the detection limit of the ICP and showed a strong resistance to the leaching from the TiO polyhedra. However, there was an increase in the leaching of Ca and Pu in the amorphous sample, with Ca increasing from 0.72 g m^{-2} to 5.99 g m^{-2}, while the Pu increased from 0.02 g m^{-2} to 0.22 g m^{-2}. Although there is a 10 fold increase in the release of Pu, the increase in total weight loss is minimal due to amorphisation, with the crystalline sample weight loss of 0.02% compared to 0.05% for the amorphous sample.[94] Fillet *et al.* found two dissolution rates for Ca in a Nd-doped zirconolite, an initial release rate and a saturated rate by studying the release of Ca between 50 and 200°C. The initial rate was found to be 10^{-2} g $m^{-2}d^{-1}$ at 100°C and 10^{-1} g $m^{-2}d^{-1}$ at 200°C, with an activation energy for hydrolysis of Ca of 22 kJ mol^{-1} (0.23 eV). The second rate is observed not to vary with temperature and is calculated to be 10^{-6} g $m^{-2}d^{-1}$. This is thought to be due to the formation of an altered layer which limits further release. The formation of a layer is confirmed by scanning electron microscope (SEM) and atomic force microscope (AFM).[107] The initial rate of release of Ca at 100°C is lower then that observed by Weber *et al.* if considered over the same 14 day period. This may be due to the Nd doping which occupied the Ca sites, meaning less Ca is in the structure. Fillet *et al.* have stated that the initial rate lasts only a few hours or up to a day before dropping to the saturated rate, therefore the value of Ca release over a 14 day period will be a combination of the rates reported by Fillet *et al.* and will be even lower than those reported by Weber *et al.*. The effect of radiation damage on the leach rate was also studied by Fillet *et al.* through the use of Pb ion bombardment at a dose of 3 x 10^{14} ions cm^{-2}

and 2 x 10^{16} ions cm^{-2}. The initial rate of leaching was extended to 1-2 days for the amorphous samples, but the rate was within 1.5 times the crystalline rate for both samples. The saturated leach rate was also similar to the final rate, being 10^{-6} $gm^{-2}d^{-1}$. These results allowed Fillet *et al.* to propose that the chemical durability of zirconolite is not fundamentally modified after radiation damage, in agreement with Weber *et al.*.

The effect of pH on the leaching behaviour of undoped and Nd-doped zirconolite was studied by Larguem *et al.* using the static method at 90°C for 1-6 months.[108] It was found that the pH decreases in each sample is due to the formation of metal hydroxides. The result from the deionised water showed that there was preferential leaching of the Ca and Nd ions from zirconolite in agreement with the previous studies.[108] SEM was used to study the surface of zirconolite after the leaching studies and found that the acidic environment led to no visible alterations to the surface. However, this was not the case in the neutral and basic environments which led to significant surface alterations. Elastic Recoil Detection Analysis (ERDA) measurements showed that the basic environment led to the the least surface hydration.[108] The lack of the hydration layer may prevent the protecting layer being formed, meaning that the leach rate may not decrease to the saturation levels; this is significant because the GDF is designed to have a basic environment. However, only a weak pH dependence was discovered by PNNL when studying non-radioactive-doped zirconolite, with the Mo release reaching steady state within 200 days when using the flow technique.[9] Loaded samples were then investigated in various pH environments and it was found that the Pu, Ti, Mo, Gd and U leach rates are similar at pH 2. In solutions above pH 2 there is a decrease of 2 orders of magnitude in the leach rate of Pu and Ti, while the others remains constant. It has been discovered that the rate of dissolution is invariant with experimental set-up also on the Pu loading.[9] The decrease in leaching of Ti has been supported by more recent research by Pöml *et al.* who found that the Ti concentration was an order of magnitude higher in the HCl solvent compared to the other solvents.[109] However, this increase was also observed for the other elements.[109] Strong Ca leaching was observed for all but the basic solution, with concentrations of 10, 8 and 5 μg/g in HCl, NaCl and H_2O, respectively. However, in NaOH and NH_3 the concentration of Ca ions was only 0.2 and 1 μg/g, respectively. In contrast to the results of Weber *et al.[94]* and at PNNL,[9] Pöml *et al.[109]* found that there was a difference in leaching rates depending on the crystalline state of the zirconolite sample. The amorphous zirconolite sample led to a very high concentration of Pu, Ca and Al ions in the solution and resulted in a thick layer of TiO_2 forming on the zirconolite surface, while the crystalline sample was hardly attacked.[109] The results of Pöml *et al.* also disagree with the activation energy for elemental loss calculated by Fillet *et al.* (22 kJ mol^{-1}), as Pöml calculated a value of 8 ± 4 kJ mol^{-1} (0.08 eV), with an activation energy of 15-20 kJ mol^{-1} calculated for Ti leaching. These dissolution energies calculated by Pöml *et al.* appear to be too low to account for the stability of the Ti network and zirconolite substrate (after formation of the protecting layer) found in the other studies. Pöml *et al.* also discovered an apparatus dependency on the concentrations observed. This study used three different reactor vessels, Teflon, nickel and silver, due to temperature restraints and reactivity. The nickel reactor caused a reduction in the concentrations of Ti, Zr and Ce ions compared to those from the Teflon vessel (see above), although the experiments were carried out at a higher temperature, which should increase the rate of release. The reaction was also carried out in a silver vessel to assess the effect of Ni on the reactions. Ag is expected to be more inert than Ni. However, the Ag vessel led to a high concentration of Ca, Ce and Al ions in solution. The particles were then examined under SEM and showed that the zirconolite sample had decomposed into TiO_2 and ZrO_2 precipitates.

Ringwood *et al.* had previously studied the leaching of SYNROC and glass to compare the stability of the waste form in either pure water or 10% NaCl under accelerated conditions, using high temperatures and pressures.[10] Ringwood found that SYNROC A was unaltered in pure water at 1000 bars up to 600°C for 24 hours. However, in the NaCl solution the kalsitite and leucite phase decomposed and led to the release of Cs into solution. When SYNROC B was tested, which does not contain these phases, the samples were unaffected by the same treatment. SYNROC B was then loaded with 1% of U, Sr and Cs (one in each crystal phase). No loss of these ions was observed in the same leaching test, even at temperatures as high as 800˚C.[10] Cs was finally leached at 900˚C at 5 kb when the surface of hollandite crystal altered in TiO_2, while the zirconolite and perovskite phases retained all the U and Sr, even up to 1000˚C.[10] Borosilicate glass was studied under similar conditions and completely devitrified and disintegrated under 1000 bars at 350-400˚C in 24 hours, with losses of 50-90% Cs and 30-90% U.[10] The fact that no U was leached from the zirconolite phase under the extreme conditions is in conflict with the recent studies that have found a low leach rate of dopants from zirconolite in milder conditions. The difference could be due to the 24 hours Ringwood *et al.* used in their experiments compared to the longer window used in the other studies. Oversby and Ringwood[110] also performed leach tests on SYNROC samples and discovered a two rate limit for Ca release in support of the later results of Fillets *et al.*.[107] The time frame required to reach this second rate was dependent on the temperature of the experiment, 3 weeks at 95˚C and 1 week at 200˚C.[110] At these two temperatures it was found that the rate at which Ca ions leached from the SYNROC increased dramatically with temperature, while the Nd release rate decreased, which Fillet *et al.* did not report. The Ti and Zr release rate was low and independent of the temperature, which agrees with the more recent studies. Oversby and Ringwood also performed leach tests on natural zirconolite samples to compare the results of the synthetic samples and found that the radiation dose has a small effect on the durability of the sample in agreement with PNNL findings. The release of U ions from the heavily damaged zirconolite was 5 times larger than the less damaged zirconolite, although the heavily damaged sample had received a dose 100 times higher than the other sample, with leach rates of 2.1 x 10^{-7} g cm^{-2} d^{-1} and 4.1 x 10^{-8} g cm^{-2} d^{-1}, respectively.[110]

3.2.6 Positron annihilation

Positron annihilation has been used to study the charge compensation in zirconolite, resulting from the doping of Ce, Np and Pu ions on Ca sites and Al on Ti sites. Hadley *et al.* doped a zirconolite structure with 0.2 formula unit of Ce with either 0 or 0.4 formula unit Al for charge balance. When no Al was added, the charge balance was expected to arise from cation vacancies. However, the use of ESR and thermogravimetric measurements showed that the Ti acted as the charge balance by forming Ti^{3+} to prevent the introduction of vacancies.[111] However, if the sample was oxidised it was found that the positron lifetime increased by 20%, indicating that oxidised doped zirconolite introduced cation vacancies to act as charge balance. No vacancies were introduced in the zirconolite structure when the Al acted as the charge balance. If a 0.1 formula unit of Ce was introduced with no Al compensation then the positron lifetimes indicated that cation vacancies were present. Reduction of the sample resulted in a decrease in positron lifetime, meaning that vacancies were absent and the charge balance was accomplished through Ti^{3+} ions again.[111] This study was followed up with the substitution of Gd into zirconolite at three different concentrations, 0.02, 0.1 and 0.2 formula units. Hadley *et al.* discovered that for the 0.1 and 0.2 Gd doped samples, the partial charge balancing was achieved through the substitution of Gd at Zr sites as well as Ca, in combination with the formation of Ca vacancies.[112] It was also proposed that the 20% increase in positron lifetime in these doped zirconolite samples is due to the presence of 0.05 formula unit cation vacancies to balance the excess charge on the dopant.

3.2.7 Computational simulations

There have been a limited number of theoretical studies on zirconolite, due in part to the complicated structure. The studies that have been performed have focused on classical cascade simulations, which simulate the impact of the recoil nucleus with a lattice ion. Veiller *et al.* studied the recoil of an U ion in the bulk of zirconolite with different initial velocities and studied the residual damage generated as a function of these velocities. The Buckingham potentials used in the simulation were fitted to the lattice parameters and the atomic positions of the structure obtained by XRD experiments performed by Rossell[2] and splined to Ziegler, Biersack and Littmark (ZBL)[113] potentials at small separation distances. The displacement energies (E_d) were calculated for each element and ranged between 15 eV for O to 48 eV for Zr.[114] The damage resulting from the cascade is divided into two regions. The first region is centred on the recoil track and is the creation of a quasi-amorphous region. The second region comprises of isolated point defects which are separated from the track.[114] The structure of the amorphous region was compared to observations made from experimental EXAFS measurements, which identified trends in the amorphous structure. The simulated amorphous structure agreed only with the experimental results for the disorder of the cation's first coordination shell. The decrease in coordination of Ca is observed in the simulations but not for the Ti ions, as found in the experiments. In contrast to experiment observations there is no observed change in the second neighbour bond distance. However, Veiller *et al.* believe that the amorphous structure obtained in the simulation will still capture the different trends in the behaviour of the crystalline and amorphous structures.[114] Chappell *et al.* also studied the same loaded zirconolite system but with more realistic kinetic energies of 70 keV, with the U substituted for a Zr ion.[115] The potentials were fitted to the bulk structure but also to amorphous structures obtained from DFT relaxation of classical MD calculations run at 5000 K. These potentials should give a more accurate description of the healing that occurs within zirconolite as the potentials will not be biased towards the crystalline state. The highly repulsive ZBL potentials were also used in these simulations. The simulations show that the oxygen ions are the most mobile within zirconolite, followed by calcium. The Zr lattice position is the most stable site in the structure, with the lowest number of defects normalised to the number of displaced O. It is proposed that this is due to the size of the Zr ion and therefore the amount of energy to displace it from the lattice site, which is supported by the E_d calculated by Veiller *et al.*. Analysing the coordination of the Ti polyhedra in the damaged region, it was found that the common coordination was 2, 3 or 4 oxygen ions. This is in disagreement with the experimental XAS studies that found that in amorphous zirconolite the favoured Ti coordination was 5.[106] The resulting structure of the U recoil cascade can be divided into two regions, which agrees with Veiller *et al.*. However, the first region is comprised of a large number of point defects in a crystalline structure, not amorphous as predicted by Veiller *et al.*. There is agreement with the structure of the second region being comprised of isolated point defects at a distance from the U track.[115]

Chappell *et al.* also extended their work to look at multiple cascade events occurring within the same simulation cell. This was achieved by initiating a second 70 keV cascade from the structure obtained from the single cascade simulation. The residual damage from the dual cascade is larger than that obtained from the single cascade event. The resulting crystal structure is also changed as the end of the track is now amorphous instead of a highly damaged crystal.[115] The dual cascade led to an interesting defect distribution, with, as predicted, a large number of Ca and O defects. However, the second cascade led to a significant reduction in the number of Zr and Ti residual defects.[115] Despite this, there is a 7% increase in the residual damage from the dual cascade compared to two single cascades. This has led Chappell *et al.* to predict that damage recovery is much more difficult in an already damaged structure and that this may lead to the tendency for amorphisation to be higher than expected.

3.3 Summary

This chapter shows that there is good agreement between the experimental and theoretical studies in MgO for the defect properties, although there is significant differences between the formation energy of Schottky defects. The computational simulations are also able to give an answer to conflicting experimental results, such as the Mg vacancies. The vast amount of experimental results in the literature means that the computational models are able to check accuracy and therefore make useful and accurate predictions.

The current understanding of the defects in zirconolite have come from experimental studies, with the limited computational results in agreement with the behaviour of the bulk under irradiation. The coordination changes of the titanium polyhedra are the most prominent changes in the bulk due to an irradiation event, observed both experimental and theoretically, as well as the ease in formation of the Ca defects, seen in the leaching studies and the cascade simulations.

Chapter 4

Point defects in MgO

4.1 Introduction

Radiation events, such as the decay of encapsulated radio-nuclides, produce high energy particles, such as alpha particles, and recoil nuclei with energies of the order of several tens of keV. The high velocity nuclei and particles exchange energy with the host atoms and create regions of local dynamic disorder in the lattice. The disordered system recrystallises over a period of a few tens of picoseconds but residual defects remain and it is the long timescale evolution of these residual defects that will eventually modify the microstructure of the material.[116, 117] The initial radiation event can be successfully modelled by molecular dynamics cascade simulations but long timescale methods, such as kinetic Monte Carlo[92] and rate theory,[118] are required to investigate microstructure evolution.

The interaction of the alpha particle with the host matrix results in the loss of energy via two mechanisms, elastic and inelastic collisions (figure 4.1). The energy loss due to the elastic collisions with atoms is known as nuclear stopping, S_n. The dissipation of energy into the atomic system causes the dynamic disorder associated with radiation damage. The energy loss due to inelastic collisions with electrons is known as electronic stopping, S_e. The S_e results in the excitation of electrons as the energy is absorbed from the alpha particle. This results in the formation of excited electrons, holes and excitons, which are able to diffuse through the material and become localised in the lattice (self-trapping) or at defect/impurity sites (trapping). The energy of an alpha particle ejected from an actinide is around 5 MeV,[15] at these energies there is an average of three orders of magnitude difference between S_e and S_n for a ceramic material. Therefore, more energy will be dissipated into the electronic system before sufficient energy has been removed from the alpha particle for S_n to dominate. This is shown by the alpha particle causing about 100 atomic displacements in zircon compared to the 1000 created by the recoil particle.[15]

Radiation damage simulations have traditionally employed classical methodologies because the length and timescales required are orders of magnitude higher than those feasible for *ab initio* methods. The cascade simulations that are usually performed give a good description of S_n but take no account of S_e and therefore they neglect the contribution to radiation damage from electronic excitations. There has been a recent revival of interest in attempting to understand and include these effects, with notable progress in metallic materials.[119, 120, 121] Electronic excitations in insulating materials are more complex than those in metals as the band gap results in a range of additional processes, including the trapping and self-trapping of electrons, holes and excitons.[122] The trapping of electrons and holes at defects in ionic crystals is particularly relevant to radiation damage,[123] as the trapped carriers will effectively change the net defect charge and this will have a strong effect on defect migration energies, and hence the microstructure evolution. Such effects cannot be reliably

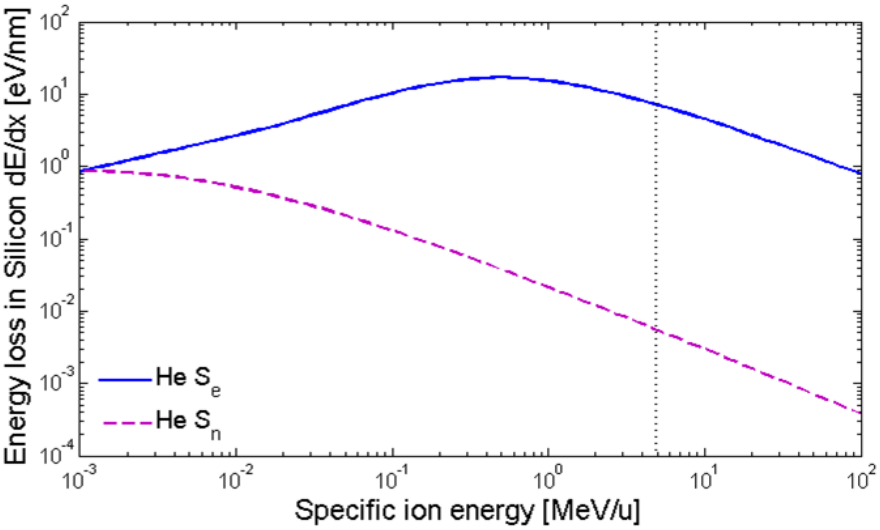

Figure 4.1: A comparison of the nuclear and electronic stopping power in silicon. The vertical dashed line shows the average energy of an α particle emitted from an actinide element. Graph calculated by SRIM.[4]

studied using classical methods. Trapped electrons and holes will also affect the defect formation energies in ionic crystals.

MgO has been studied because it is considered to be a model oxide because it is a binary oxide with the simple face centred cubic crystal structure. MgO has also received a large amount of attention, both experimentally and theoretically, allowing a comparison of the results to the literature. The comparison with the literature is important as it will allow the confidence in the modelling of the different charge states, meaning the obtained results are not an artifact of inaccurate models. The doubly charged ions in MgO make it more suitable for this research than another model oxide, NaCl, as it allows more charge states to be studied and thus allows a wider set of conclusions to be drawn on the effect of charge localisation on defect properties.

Electrons are known to localise on O vacancies in MgO and holes can localise on O interstitials. We focus on oxygen defects because of the stronger charge localisation. We investigate the effect of charge localisation on oxygen vacancy and interstitial formation energies in MgO. We calculate defect formation energies for O vacancies with zero (F^{2+}), one (F^{+}), and two (F^{0}), trapped electrons and O^{2-} interstitials with zero, one and two trapped holes. These energies are used to calculate Frenkel defect energies for neutral, singly charged and doubly charged defect pairs along with the corresponding migration barrier energies for the vacancies and interstitials. Frenkel pairs are created by radiation events in crystals and it is the creation and migration of these defects that dominate the long timescale evolution of the microstructure.

4.2 Computational method

The defect formation energies and the migration energies were calculated using density functional theory (DFT) with the Vienna *ab initio* simulation program (VASP) plane wave code.[124, 125] The generalised gradient approximation (GGA) with Perdew and Wang (PW91) exchange correlation potentials,[50] projected augmented waves (PAW) and a plane wave basis set cutoff of 700 eV were used with Γ point sampling of the Brillouin zone. A simulation cell with 3x3x3 unit cells of MgO (216 ions) was constructed and the cell was relaxed until the energy difference was less than 0.01 eV per atom, which resulted in an MgO lattice parameter of 4.14 Å. This compares with the experimental value of 4.24 Å.[126] A vacancy was created in the cell by removing an Mg or an O atom. The number of electrons was adjusted to give the required charge state of the defect. A geometry optimization, with the cell parameters fixed, was performed until the forces were less than

0.01 eV Å^{-1}. Interstitial energies were calculated by adding an O or an Mg atom to the cell in two distinct configurations and adjusting the number of electrons to obtain the required charge state. In one configuration the interstitial configuration was initiated with the extra atom in the centre of a cube of atoms and in the other a dumb-bell interstitial, oriented in the <110> direction, was created by adding the interstitial atom close to a lattice atom.

The 3x3x3 super cell was selected for this research after checking conversion of the vacancy formation energy. The conversion of the cell size was checked though the vacancy defect energy in three different supercells, 3x3x3 (216 ions), 4x4x4 (512 ions) and 5x5x5 (1000 ions). The F^0 defect energies are 10.10 eV and 10.12 eV for the 3x3x3 and 4x4x4 supercells, respectively. While the 5x5x5 required to much time too converged the forces, so was dismissed. Also the 3x3x3 supercell had been used previously by Carrasco *et al.*[127] to calculate the migration of the neutral oxygen vacancy in MgO, therefore allowing the accuracy of the simulations to be checked.

The migration energies were calculated using the standard nudged elastic band (NEB) functionality of VASP.[60] The initial and final configurations of the defect migration path were optimised and used as the end points for the NEB calculations. The initial configuration was selected so that the defect occurred near the centre of the simulation cell. The final configuration was achieved by the same defect configuration in another position in the lattice, for the vacancies it was across the *xy* plane. The interstitials were shifted into the next unit cell. The initial guess of the migration pathway was a linear interpolation between these two configuration. The migration path was then optimised through the NEB calculation. A spring constant of 5 eV Å^{-2} was used with five images along the path. Each image was optimised until the forces were less than 0.01 eV Å^{-1}.

The neutral (Schottky and Frenkel pair) defect combination energies are calculated from the isolated point defect energies using equation 4.1. The Schottky defect energy (E_s) is defined as:

$$E_s = (E_{vMg} + q_{vMg}\Delta V) + (E_{vO} + q_{vO}\Delta V) - \left[(2N_{MgO} - 1)\frac{E_p}{N_{MgO}}\right] \tag{4.1}$$

here E_{vMg} is the energy of the cell containing a magnesium vacancy, E_{vO} is the energy of the cell containing an oxygen vacancy, $q\Delta V$ is the potential alignment correction,[57] N_{MgO} is the number of MgO units in the perfect cell (108 in this case) and E_P is the total energy of the perfect cell.

The Frenkel defect energy (E_F) is defined as:

$$E_F = (E_v + q_v\Delta V) + (E_i - q_i\Delta V) - 2E_p \tag{4.2}$$

here E_i is the energy of the cell containing the interstitial ion.

4.3 Results and discussion

4.3.1 Defect formation energies

The defect formation energies were calculated for oxygen vacancies and interstitials in three different charge states and the doubly charged Mg vacancy (V^{2-}). The formation energies for the isolated defects were combined to obtain the Schottky and Frenkel defect energies for comparison with previous calculations. Since only the doubly charged Mg vacancy energy could be reliably calculated, the Schottky defect energy (equation (4.1)) was calculated for the doubly charged defects only and the result is shown in table 4.1. The calculated value for the Schottky defect energy is 5.05 eV. This is lower than the corresponding values for the Schottky defect calculated using a range of classical potentials.[88, 90, 89, 84, 91] The reason for the lower defect energy than the classical potential may be due to the lower charge on the ions than in the DFT calculation (±1.6) than the

Table 4.1: Schottky defect energy for the doubly charged vacancy pair.[1]

Schottky pair	Schottky energy (eV)		Literature results (eV)
	With correction	Without correction	
F^{2+} + V^{2-}	5.05	5.23	7.2[88] 7.5[89] 7.5-7.9[90] 7.53[91] 8.44[84] 8.2[128] 5.97[88] 6.88[93] 6.99[129]

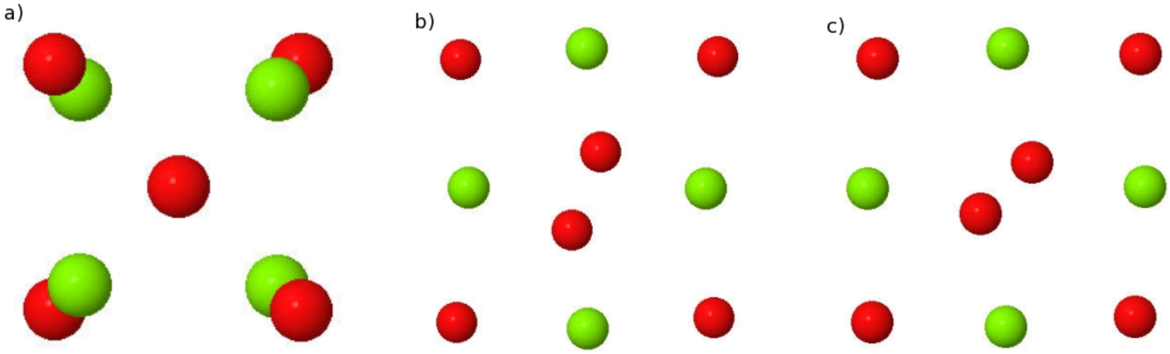

Figure 4.2: Relaxed configurations of the a) O^{2-}, b) ${O_2}^{3-}$ and c) ${O_2}^{2-}$ interstitials viewed in the (001) projection. The red spheres show oxygen ions and green spheres show magnesium ions.[1]

classical simulations (±2). The lower charge on the ions reduces the Coloumbic repulsion of the remaining ions surrounding the vacancies, thus reducing the energy cost of creating the vacancies. This is due to the structure of MgO, as the creation of the doubly charged vacancy make that site either positive or negative with respect to the lattice, depending on the vacant species. This charged site is then surrounded by similar charged ions as the site, causing the relaxation of these ions away from the vacancy site. Doubly charged Schottky defect energies have previously been calculated using *ab initio* techniques using the Hartree Fock embedded cluster method[128] and periodic DFT[93, 88, 129] using 32, 128 and 180 ion cells, respectively, with LDA pseudopotentials. De Vita *et al.[93]* and Alfe and Gillan[129] employed Γ point sampling of the Brillouin zone and obtained a value of 6.88 eV and 6.99 eV, respectively, while Gilbert *et al.*[88] used a 6x6x6 k-point mesh with a localised orbital methodology and obtained a defect formation energy of 5.97 eV. The lower value for the Schottky defect energy calculated here can be explained by the GGA methodology used in this research, which tends to predict lower cohesive energies[130] and thus lower defect energies, than the LDA methods employed in previous publications. The Hartree Fock value obtained by Grimes and Catlow is 8.44 eV[128] and is the highest value for the Schottky formation energy. The previous *ab initio* calculations have not used a potential alignment correction and this means that the vacancy energies obtained to calculate the Schottky defect formation energy are not offset to the same zero energy. Therefore, Lany and Zunger propose that these values are not physically meaningful.[57]

4.3.1.1 Oxygen interstitials

The energies of O interstitials with three different charge states were calculated by relaxing from two different starting configurations for each charge state, as described in the previous section. The configurations with the lower energies were identified and these are shown in figure 4.2. For the O^{2-} interstitial, the preferred interstitial site was found to lie in the centre of a cube of atoms, as was seen in previous classical simulations. Bader analysis showed that the O^{2-} interstitial, which is located in the centre of a cube of ions, has 0.1e less charge than the lattice oxygen ions (-1.5). The density of states (DOS) of the O^{2-} show that two defect levels are created in the band gap, at 1.88 and 1.90 eV above the valence band. These defect levels are both occupied

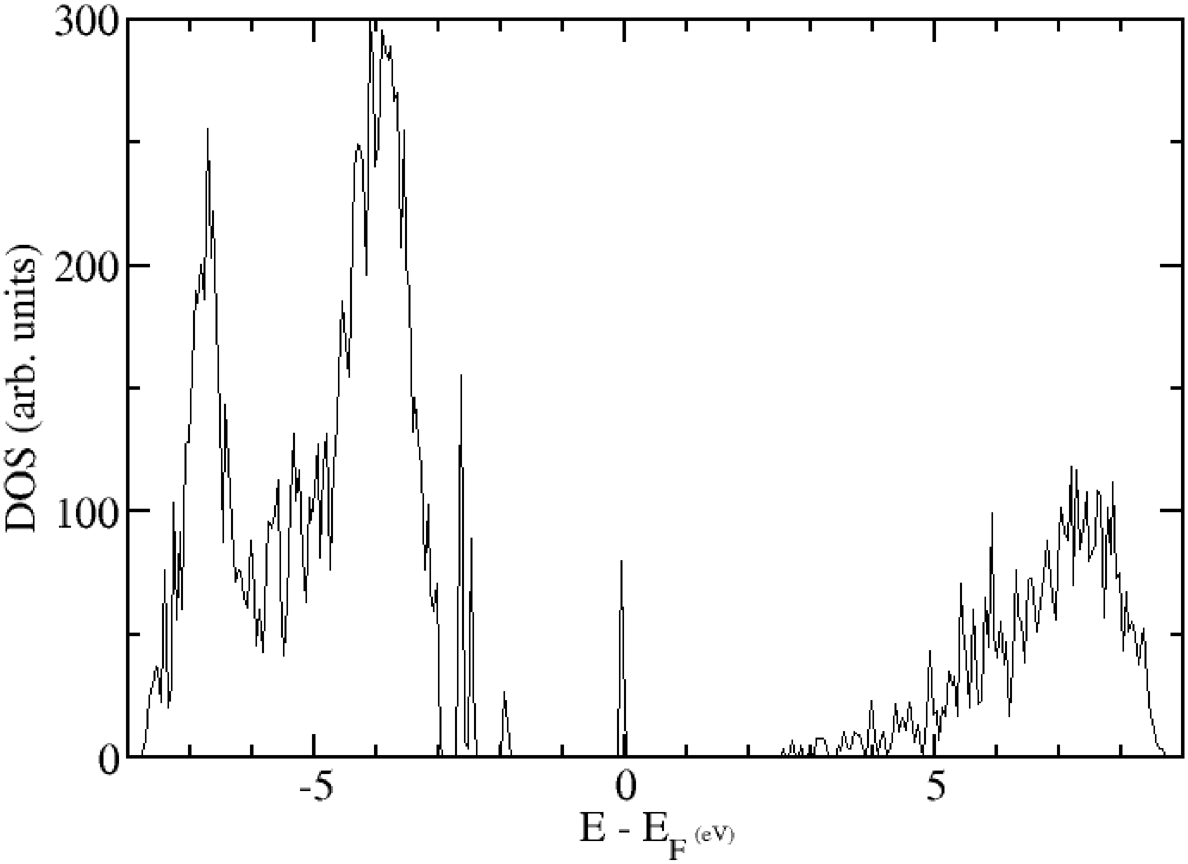

Figure 4.3: Electronic DOS of the cell containing the O^{2-} interstitial. The two defect levels are smeared into one level located around the Fermi level.

by two electrons. These defect levels are constructed from *p* orbitals of the interstitial.

The $O_2{}^{3-}$ defect favoured a <110> dumb-bell configuration (figure 4.2b) with the split interstitials separated by 1.87 Å. In this structure, Bader analysis showed that electron density was transferred from the lattice O ion to the interstitial and the surrounding O ions, giving an equal -1.22 charge on the dumb-bell atoms. The DOS has shown the formation of this dumb-bell defect created two defect levels in the band gap. These levels are 0.28 and 1.00 eV above the valence band. These defect levels are both occupied and occur in the spin-up and spin-down configurations.

The neutral interstitial ($O_2{}^{2-}$) relaxed into a <111> dumb-bell configuration with a separation of 1.42 Å between the split interstitial ions (Figure 4.2c). The semi-empirical calculations of Brudevoll *et al.*[131] also found this to be the favoured dumb-bell configuration for the neutral interstitial. It was previously assumed by experimentalist[132] that the dumb-bell was orientated in the <110> direction but the calculations presented here suggest that the lowest energy configuration is the <111> dumb-bell. The Bader analysis of the neutral split interstitial gave a charge of -0.8 on both oxygen ions. This shows that 0.8e were transferred from the lattice ion to the neutral interstitial, leading to the strong dumb-bell formation. The larger electron transfer for the $O_2{}^{2-}$ interstitial accounts for the smaller dumb-bell separation, as the higher shared electron density forms a stronger covalent bond than for the $O_2{}^{3-}$ interstitial. Analysing the DOS shows that there are four defect levels in the band gap, caused by the presence of the $O_2{}^{2-}$, two in the spin-up configuration and two in the spin-down configuration. The two spin-up defects states occur at 0.32 and 0.72 eV above the valence band, while the

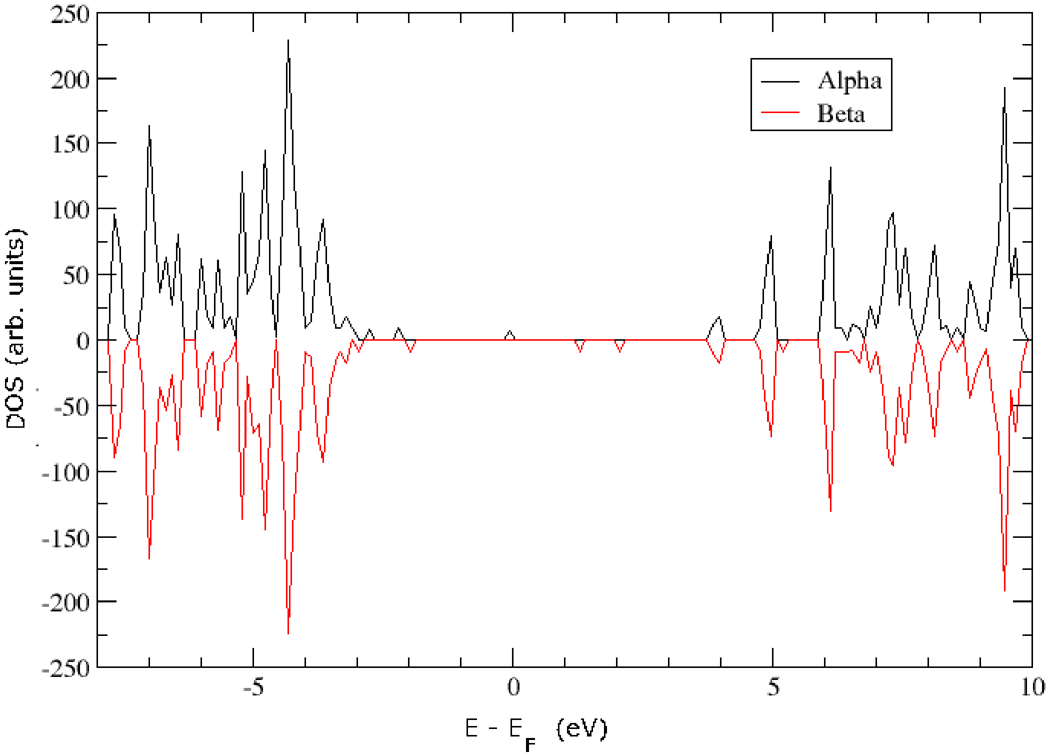

Figure 4.4: Electronic DOS of the O_2^{3-} interstitial in the <110> dumb-bell. Alpha shows spin-up states, beta shows the spin-down states.

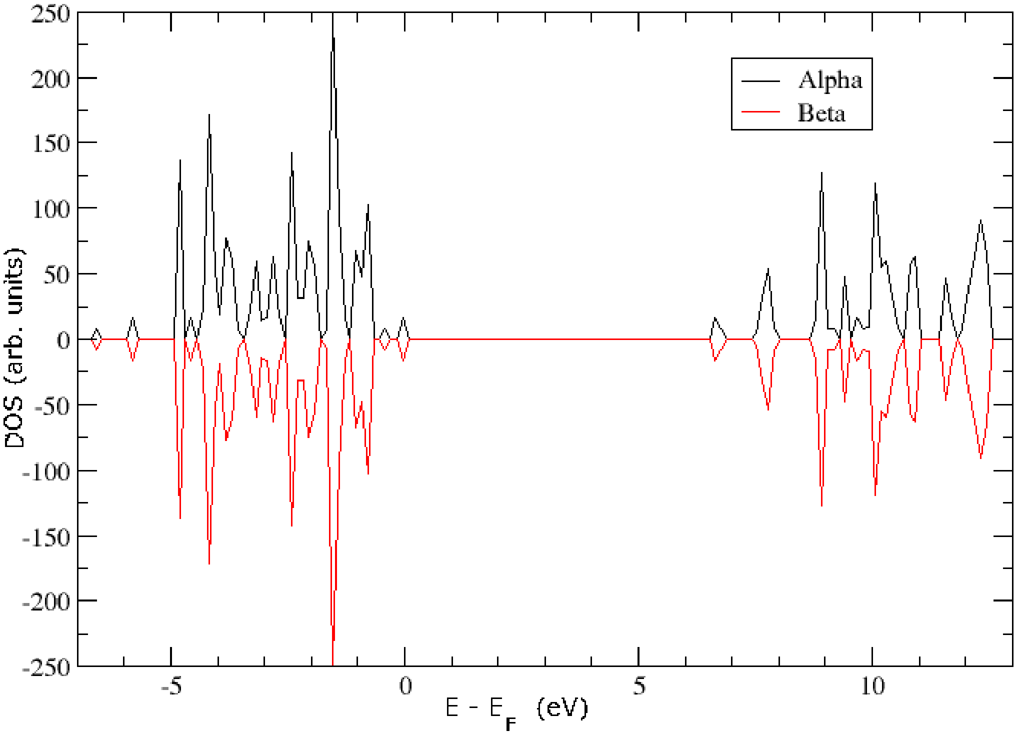

Figure 4.5: DOS of the O_2^{2-} interstitial in the <111> dumb-bell configuration.

Table 4.2: Frenkel pair energies for the oxygen ions with various oxidation states and the doubly charged Mg ions.[1]

Frenkel pair	Frenkel energy (eV)		Literature results (eV)
	With correction	Without correction	
$O_2{}^{2-}$ + F^0	10.28	10.28	
$O_2{}^{3-}$ + F^+	11.93	11.89	
O^{2-} + F^{2+}	13.32	13.28	13.57[86], 15.2[89], 13.81[84], 12.2[88], 13.6[88]
Mg^{2+} + V^{2-}	10.41	10.37	10.35[88], 14.1[88], 14.1[86]

spin-down levels are at 0.32 and 0.72 eV above the valence band.

4.3.1.2 Magnesium interstitials

The magnesium was inserted into the lattice in the same positions as the oxygen interstitials, to locate the lowest energy site. Zero, one or two electrons were added to the system to simulate the different charge states. The favoured site for the Mg^{2+} was in the centre of the 8 membered cube, similar to the O^{2-}. Bader analysis shows that the interstitial has a charge of +1.50. The centre of the 8 membered cube was also the favoured site for the other Mg interstitials considered. However, upon performing Bader analysis on the Mg^{+} and Mg^{0} interstitial configurations, the charge of these interstitials were +1.50 and +1.49. In both of these cases the excess electrons inserted into the simulation cell were delocalised over all the oxygen ions. The Mg^{2+} interstitial does not localise electrons because the conduction band of MgO is constructed from the *s* orbital of the magnesium ions,[133] so the addition of the electron is delocalised over the conduction band.

4.3.1.3 Magnesium vacancies

The magnesium vacancies were studied in three charge states, the V^{2-}, V^{-} and V^{0} with zero, one and two holes localised on oxygen ions adjacent to the vacancy, respectively. The V^{2-} caused the displacement of the surrounding lattice oxygen ions by 0.12 Å from the bulk positions. The V^{-} vacancy was simulated by moving an oxygen ion away the vacancy by 0.12 Å, to break the symmetry around the vacancy to allow the hole to localise. The isosurface of the V^{-} unpaired electron is shown in figure 4.6, this shows that the hole is delocalised over all 6 oxygen ions surrounding the vacancy. This is the incorrect structure of the V^{-} as ESR experiments show that the hole is localised on a single oxygen ion next to the vacancy. This incorrect structure is caused by the self interaction error in DFT. ESR results show that the V^{0} vacancy localises the two holes on oxygen ions 180º apart. However, the isosurface of the V^{0} vacancy has the holes delocalised over the six oxygen ions, as for the V^{-} vacancy.

4.3.1.4 Frenkel defect pairs

The calculated O interstitial formation energies were combined with the vacancy formation energies to calculate Frenkel energies (equation (4.2)) for three oxidation states and the results are summarised in table 4.2. Only the doubly charged Mg pair is considered here because of the reliability of the results of the Mg defects in the other charge states. The available classical and other *ab initio* results are also included in this table. There is good agreement between the DFT results and the classical results for the O^{2-} Frenkel defect, indicating that empirical potentials give a good description of the doubly charged defects in MgO. There is a wide scatter in the results obtained using empirical potentials, with values ranging from 13.57-15.2 eV.[86, 84, 89] Previous DFT calculations give Frenkel defect energies of 12.17 eV and 10.35 eV for the oxygen and magnesium ions respectively, using a 180 ion cell with localised orbitals and LDA pseudopotentials.[88]

There are no previous calculations for $O_2{}^{2-}$ and $O_2{}^{3-}$ Frenkel defects in MgO. Our calculations indicate that the neutral $O_2{}^{2-}$ Frenkel defect has a formation energy which is 3 eV lower than the O^{2-} Frenkel defect

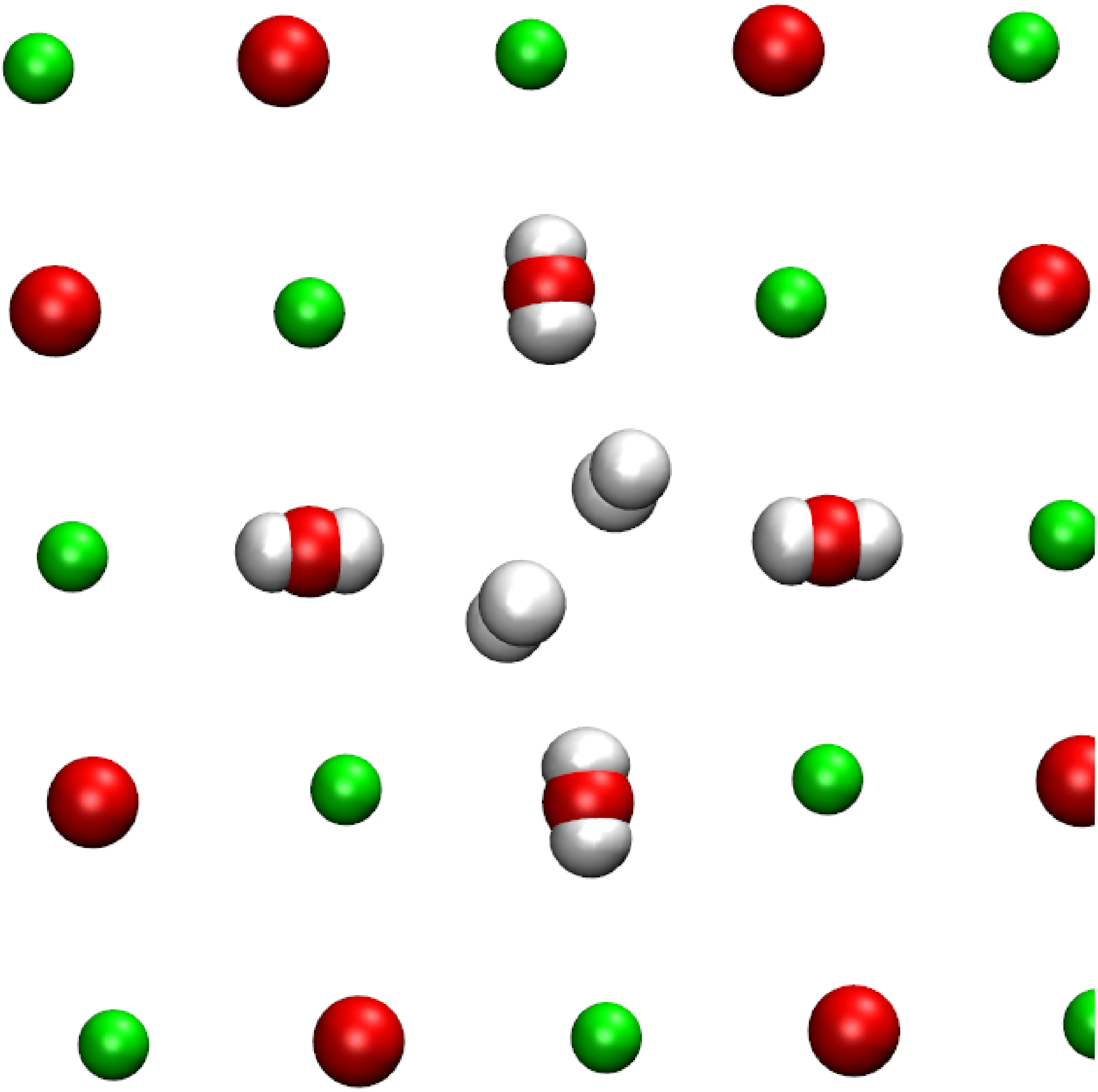

Figure 4.6: Isosurface of the unpaired spin at 0.04 e Å^{-3}, showing the delocalisation of the hole associated with the V$^-$ vacancy.

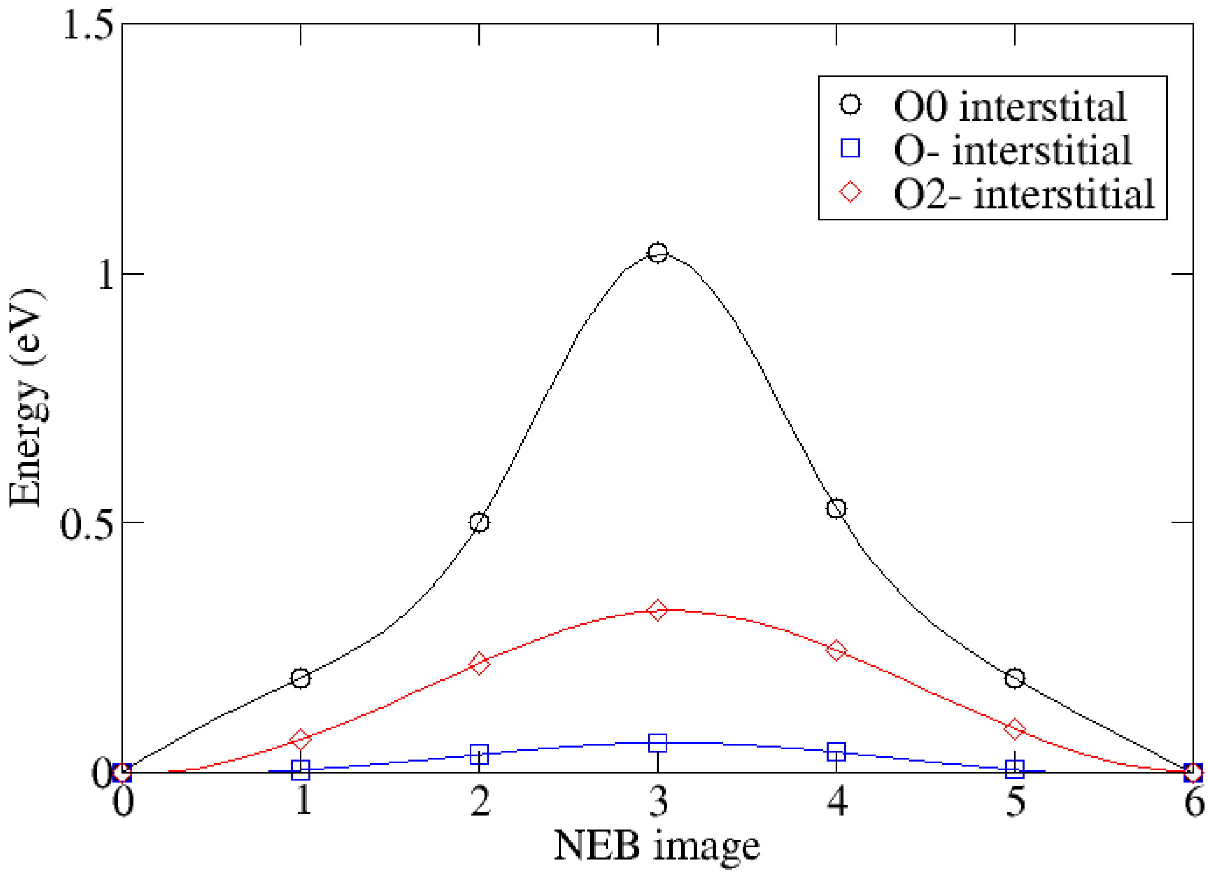

Figure 4.7: Migration barrier of the O^{2-} (diamonds), O_2^{3-} (squares) and O_2^{2-} (circles) interstitials in MgO.[1]

energy. This has significant implications for radiation damage because the number of oxygen Frenkel pairs created by a radiation event could be much higher than predicted from classical simulations.

4.3.2 Defect migration energies: interstitials

The migration barrier energies of the three oxygen interstitials were calculated by NEB (5 images), with the points fitted with a cubic spline in figure 4.7, and the results are summarised in table 4.3. The barrier for the O^{2-} interstitial is lower than those predicted by classical simulations[86] and previous LDA DFT calculations.[88, 131] The barrier is lower than the classical simulations because of the lower charge on the interstitial oxygen in this simulation (-1.5) than the formal charge in the classical simulation (-2), which results in a lower Coloumbic repulsion between the two dumb-bell oxygen ions at the saddle point in the DFT simulations. The saddle point for the O^{2-} interstitial migration is the <111> dumb-bell configuration, with a split interstitial distance of 2.27 Å, as shown in figure 4.10a. The electron density of the interstitial does not change significantly during migration.

The O_2^{2-} interstitial migration energy was lower than that found previously, although the same migration pathway was found in both studies. The lower barrier found in this study is due to the larger lattice constant and larger unit cell compared to those used in the LDA simulations of Brudevoll *et al.*.[131] Brudevoll *et al.* used a simulation cell of 16 ions, with the lattice constant set at the experimental value of 4.21 Å.[131] Brudevoll *et al.* calculated the migration barrier through constrained minimisation using a full potential linear-muffin-tin-orbtal (FP LMTO) approach. The migration path for the O_2^{2-} interstitial was calculated to be along the diagonal of the face of the cube of ions, with the saddle point shown in figure 4.10c. The migration involves the rotation

Table 4.3: Migration of the oxygen interstitials with two, one and zero trapped holes.[1]

Defect	Barrier (eV)	Literature results (eV)
${O_2}^{2-}$	1.04	1.45[131]
${O_2}^{3-}$	0.06	
O^{2-}	0.33	0.40[86], 0.44[88], 0.54[131]

of the <111> dumb-bell to a <110> dumb-bell, the motion along the <110> direction, the formation of another <110> dumb-bell and, finally, rotation to the <111> dumb-bell configuration, this is shown in figure 4.8. Bader analysis shows that there is a redistribution of the electron density as the oxygen interstitial passes through the saddle point. The interstitial ion loses 0.09e compared to the initial structure giving a charge of -0.78, while the lattice oxygen from the dumb-bell gains 0.44e as the dumb-bell is broken giving a charge of -1.26. The extra electron density comes from the lattice ion that will become part of the dumb-bell, with the loss of 0.35e compared to the initial configuration resulting in a charge of -1.27. This redistribution of the electron density results in both lattice oxygen ions involved in the migration process having the same number of electrons at the saddle point. The migration barrier predicted for this pathway is 1.45 eV compared to my value of 1.04 eV; the reason for the larger barrier obtained from Brudevoll *et al.* is the small simulation cell. The small cell is responsible for the larger barrier because the transition state is highly strained with the oxygen ion migrating through the cubic face. The limited cell size may prevent the full relaxation of the saddle point configuration, resulting in the higher energy.

The singly charged interstitial was found to have a significantly lower migration barrier (0.06eV) than the other charged states. In order to check the accuracy of the calculation, the number of NEB images was increased to 11 but this was found to have no effect on the barrier height. The saddle point for the ${O_2}^{3-}$ interstitial migration path (figure 4.10b) has the interstitial slightly out of the <010> plane. There is a redistribution of the electron density at the saddle point, with the lattice ion from the initial dumb-bell regaining 0.16e of the 0.2e it initially donated to the dumb-bell giving a charge of -1.25. This electron density is donated from the lattice oxygen the interstitial is moving towards, with this oxygen losing 0.14e compared to the initial configuration resulting in a charge of -1.58. There is no significant change in the electron density associated with the interstitial during migration.

4.3.3 Defect migration energies: vacancies

The energies along the migration paths, calculated from the nudged elastic band images, are plotted for the O vacancies with three different charge states in figure 4.11. The activation energies for the three oxygen vacancies were calculated by fitting the points using a cubic spline and the migration barriers are summarised in table 4.4, along with the values calculated using other methods. Figure 4.11 shows that the migration path was independent of the charge state of the vacancy, as the saddle point occurs at the same point each charge state. The saddle point is where the diffusing lattice oxygen is between the two Mg ions in the cube face. The saddle point of the F^+ vacancy involves the delocalisation of the localised electron between two vacant lattice sites, as shown in figure 4.12. The saddle point of the F^0 is consistent with that of the F^+ vacancy, as it involves an electron in each of the vacant sites. We note that for each extra electron that is trapped at the vacancy the activation energy increases by approximately 1 eV. The F^0 and F^+ migration energies are significantly higher than the results obtained previously using semi-empirical methods (3.1 eV and 2.7 eV, respectively) but the F^0 migration energy is consistent with the previous DFT result of 4.2 eV. Carrasco *et al.* used the PW91 implementation of GGA to calculate the F^0 vacancy migration barrier via a constrained search for the saddle point.[127] The difference in barrier heights between this work and Carrasco *et al.* is larger than one would expect, as both results are obtained using PW91. Three differences have been identified between the calculation

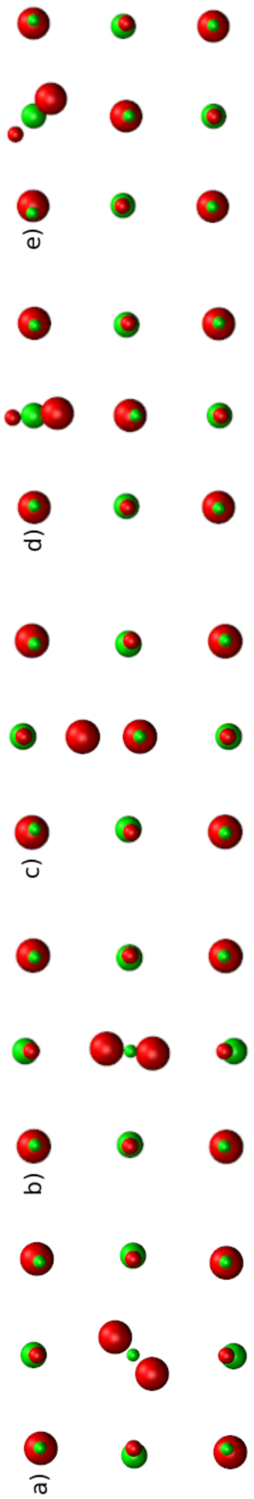

Figure 4.8: Migration path of the O_2^{2-} interstitial. Showing the a) <111> dumb-bell, b) <110> dumb-bell, c) saddle point through the <110> face, d) <110> dumb-bell and e) <111> dumb-bell. The smaller spheres show the layer above the interstitial.

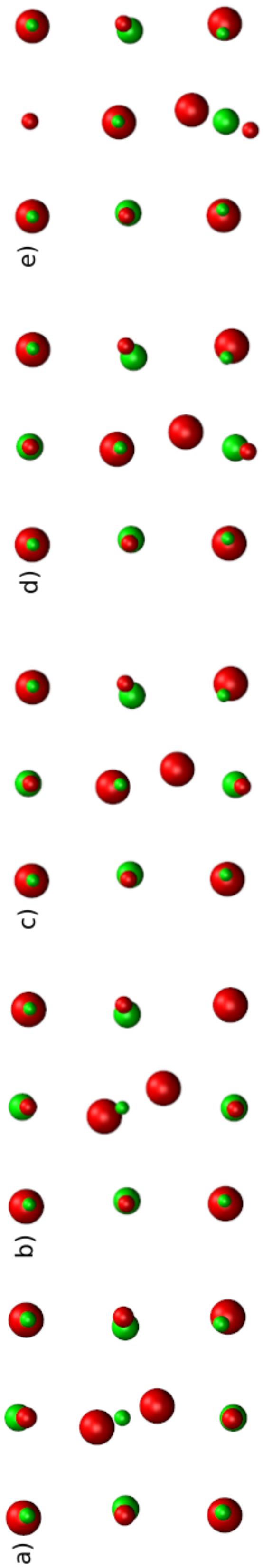

Figure 4.9: Migration path of the $O_2{}^{3-}$ interstitial. The smaller spheres show the layer above the interstitial.

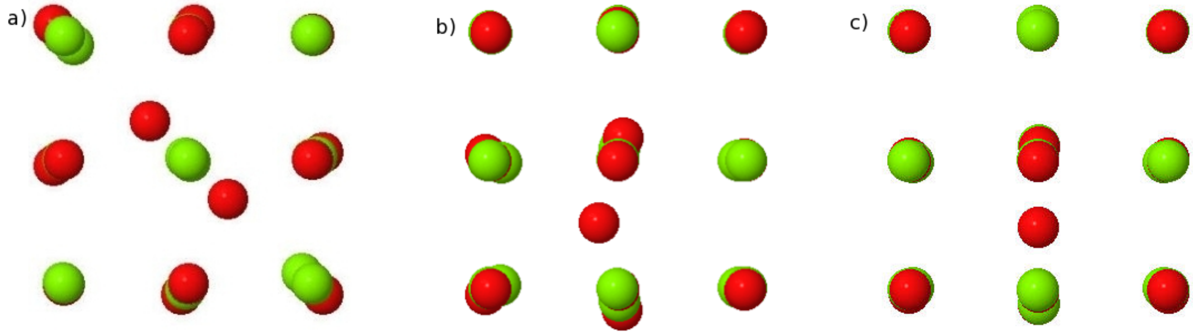

Figure 4.10: Saddle point configurations of the a) O^{2-}, b) $O_2{}^{3-}$ and c) $O_2{}^{2-}$ interstitial migration paths.[1]

Table 4.4: Migration barriers of the oxygen vacancies with two, one and zero trapped electrons.[1]

Defect	Barrier (eV)	Literature review (eV)
F^0	4.81	4.2[127], 3.1[134]
F^+	3.68	2.7[134]
F^{2+}	2.38	2.0[86], 2.12[84], 2.5[134], 2.48[93], 2.71,[68] 2.61,[69] 2.42[70]

that may account for this, the number of k points used to sample the Brillouin zone, the pseudopotential used to described the inner electrons of the oxygen ions and the method to calculate the migration barrier. Carrasco *et al.* employed a 2x2x2 mesh sampling of the Brillouin zone compared to the Γ point sampling of the Brillouin zone employed in this research. Also a different plane wave cut off is used by Carrasco *et al.* which indicates that a different pseudopotential for the inner electrons of the oxygen ions had been used compared to this work. The hard oxygen pseudopotenials used here give a more accurate description of the inner-electron wavefunction than those used in Carrasco *et al.* calculations. These differences have limited effect on the formation energy of the F^0 vacancy with respect to the oxygen atom in the cell as a reference state, as the result of 10.09 eV from Carrasco *et al.* is in good agreement with the value of 10.10 eV obtained in this work. However, there is a significant effect on the lattice parameter obtained in these calculations. The Carrasco *et al.* result of 4.24 Å is the same as the experimental result of Schmahl and Eikerling,[126] while a value of 4.14 Å obtained here has an error of 2.36%. The error associated with this calculation although small has possibly arisen from the use of Γ point sampling of the Brillouin zone. The higher diffusion barrier obtained from this work compared to Carrasco *et al.* is the result of the smaller lattice parameter, as at the transition point there will be more steric hindrance as the oxygen ion passes between the magnesium ions, resulting in a less favorable transition. Also the method of calculation of the barrier height is different, with the NEB method used in this research being more accurate. The F^{2+} migration barrier is in good agreement with experimental results obtained from the exchange rate of oxygen between the gas phase and the solid oxide using oxygen isotopes, which range between 2.42 eV and 2.71 eV.[70, 69, 68]

The observed trend in barrier height is supported by embedded DFT calculations performed by Reveles *et al.*, who studied the diffusion of oxygen vacancies in different charged states on the [100] surface of MgO.[135] Reveles *et al.* obtained a migration barrier of 2.84 eV for the F^0 vacancy and barriers of 2.18 eV and 0.94 eV for the F^+ and F^{2+} vacancies, respectively.[135] This shows that there is a significant difference in barrier heights for the migration of vacancies in the bulk and at the surface, although the charge state trend is maintained. The lower migration barriers at the surface is due to the lower coordination of the surface ions, this is seen in the diffusion pathway observed by Reveles, where the diffusing oxygen ion moves out of the surface to migrate over the two Mg ions at the saddle point. This diffusion out of the surface plane will lower the strain at the transition point, compared to the bulk diffusion, resulting in a lower barrier height.

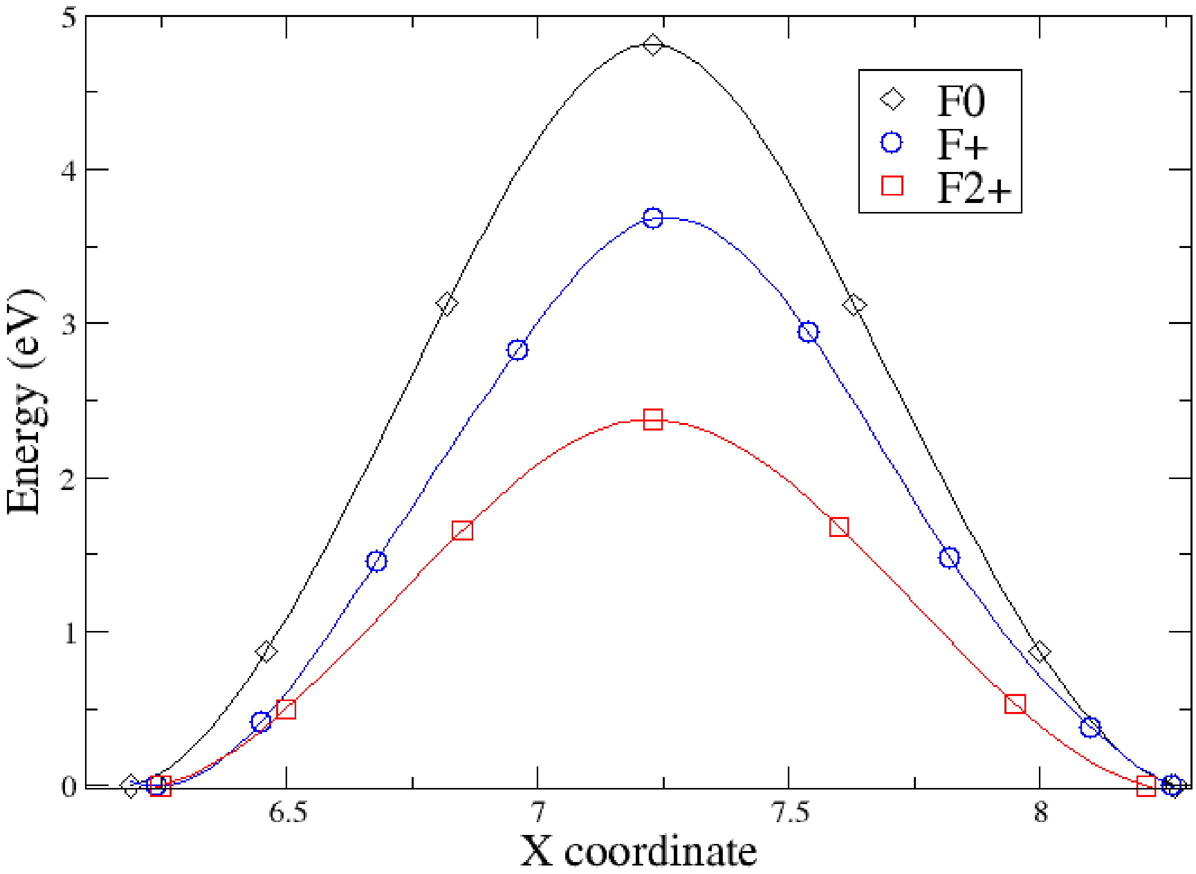

Figure 4.11: Migration barriers for the doubly charged (squares), singly charged (circles) and neutral (diamonds) oxygen vacancies in MgO.[1]

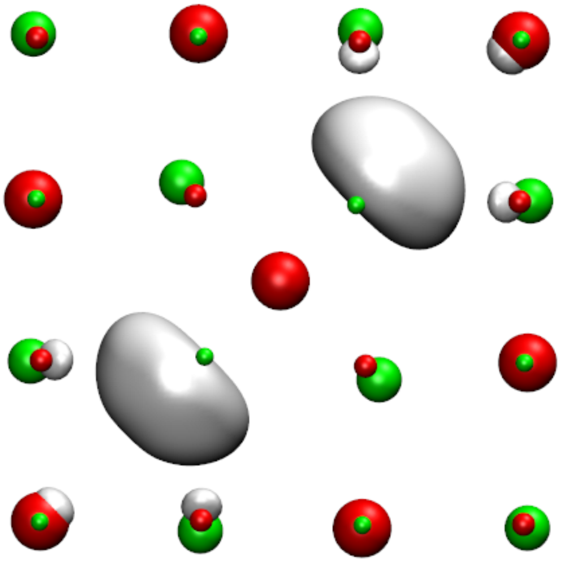

Figure 4.12: The saddle point in the migration of the F^+ vacancy. The isosurface (0.03 e Å^{-3}) shows the electron delocalised between the two vacant lattice sites. The large sphere show ions in the plane of the vacancy, the small spheres show ions in plane above the vacancy.

Table 4.5: Migration barriers of the Mg vacancies in two different charged states.

Charge state	Migration barrier (eV)	Literature results (eV)
V^0	2.25	
V^{2-}	2.23	2.12[86], 2.39[93]

The diffusion of the Mg vacancies was studied using constrained minimisation, to check whether the incorrect description of the hole localisation prevented the charge state effects. The results for two different charge states are summarised in table 4.5. Table 4.5 shows that the migration barriers are consistent for both charge states of the vacancy. Therefore, the incorrect description of the localisation of the holes associated with the vacancy means that the standard DFT methodology cannot be used to study the charge effects on the migration of the magnesium vacancies. The migration barrier of the V^{2-} vacancy is in agreement with the previously calculated barriers for the defect. The De Vita *et al.* barrier of 2.39 eV was obtained through constrained minimisation using LDA in a 32 ion cell and this is in agreement with the classical value from Uberuaga *et al.* of 2.12 eV.

4.4 Conclusions

The effects of charge localisation on oxygen point defect properties in MgO were investigated using periodic DFT. The charge state was found to have a strong effect on the minimum energy configuration of O interstitials, with ${O_2}^{2-}$ and ${O_2}^{3-}$ interstitials relaxing to dumb-bell configurations whereas the minimum energy configuration for the O^{2-} interstitial was found to be in the centre of a cube of ions. The dumb-bell formed by the ${O_2}^{2-}$ interstitial resulted in more charge transfer from the lattice ion (0.8 e) and a shorter split interstitial separation (1.4 Å) than the ${O_2}^{3-}$ dumbbell (0.2 e and 1.9 Å). The relaxed configuration has a significant effect on the migration pathway of O interstitials and, therefore, the migration barriers for the different oxidation states. The O interstitial showed enhanced radiation diffusion, with the trapping of a hole on the O^{2-} interstitial resulting in a surprisingly low migration barrier. The O interstitial formation energies were combined with O vacancy formation energies to calculate Frenkel defect energies for three oxidation states. It was found that the neutral Frenkel pair had a formation energy 3 eV lower that the doubly charged Frenkel pair and that the singly charged O Frenkel pair had an energy 2 eV lower than the doubly charged Frenkel pair.

The charge state was also found to have a large effect on the migration barriers for the oxygen vacancies. The F^0 vacancy was found to have a migration barrier 2 eV higher than the F^{2+} vacancy and the F^+ vacancy was found to have an intermediate barrier height between the F^0 and F^{2+} vacancies.

The results presented in this chapter have significant implications for radiation damage simulations of MgO and other oxide materials, such as UO_2. Radiation damage simulations have been traditionally carried out using empirical potentials with formal charges, thus only charged defects are created in these simulations. However, if the neutral defects are more stable, as suggested by the DFT calculations, then many more oxygen defects may be created than classical methods predict. In addition, the neutral oxygen defects will have significantly higher migration barriers than doubly charged defects, therefore the diffusion rates to sinks and clusters will be lower. The results suggest that O defects could survive longer as isolated point defects than Mg defects, which have much weaker charge localisation, and this will have a dramatic effect on the microstructure evolution of oxide materials subjected to radiation damage.

Chapter 5

Interstitial clusters in MgO

5.1 Introduction

Monte Carlo simulations are a common method of extending the length and time scales of molecular dynamics (MD) cascade simulations towards experimental time and length scales. The Monte Carlo calculations, as well as the other accelerated methods, like rate theory, usually only take account of the migration of the isolated defects and dimer clusters. The assumption is made that larger defect clusters are immobile and therefore, do not take part in the evolution of the damage in the system.

Temperature accelerated dynamics (TAD) simulations were performed by Uberuaga *et al.* to examine the long time evolution of radiation damage in MgO.[86] Cascade simulations were performed for a few picoseconds and used as the input for the TAD calculations. The TAD method is an accelerated molecular dynamics technique, allowing larger timescales to be studied than possible in MD. The TAD method involves running MD simulations at a higher temperature (T_{high}) than the temperature the simulation of interest is run at (T_{low}), while constraining the dynamics to the current potential well. The time of events observed at T_{high} are then extrapolated to T_{low}. Once a TAD cycle is complete, the first event to occur at T_{low} is taken and the system moves into the new potential well and a new TAD search begins in that well.

The TAD simulations found that the defects created by the initial cascade aggregated together to form larger defect clusters than the dimers seen in the cascade simulation. The TAD results also showed that the migration barriers increased as the interstitial cluster size increased, in agreement with the assumption made in Monte Carlo simulations. However, after 4.1 second in the TAD simulation a hexa-interstitial was formed by the diffusion of a di-interstital to an immobile tetra-interstitial cluster. This hexa-interstitial was found to be highly mobile along the <110> direction, with a migration barrier height of 0.24 eV compared to the isolated oxygen interstitial barrier of 0.40 eV.[86] The hexa-interstitial migration barrier was checked using DFT and the barrier increased to 0.33 eV but it was still smaller than the barrier for the isolated interstitial.[86] The octa-interstitial also showed a low migration barrier of 0.66 eV, lower than the barrier of the di-interstitial.[86] It has subsequently been shown that the penta-interstitals also showed enhanced mobility, with a barrier height close to that of the di-interstitial.[136] These results show that the assumption used in extended dynamic simulations to assume that defect clusters are immobile are invalid, meaning that these simulations may miss important effects caused by these clusters on the evolution of defects in the material.

We have shown that there is a significant effect of charge localisation on the structure and mobility of oxygen interstitials. The enhanced mobility of the O^{-} interstitial was proposed to increase the rate at which the interstitial would diffuse to defect sinks, such as grain boundaries and defect clusters. This could lead to the growth of the large defect clusters being faster than that seen in the TAD simulations. Also, a pre-existing defect cluster could act as a trap for an excited electron or hole, adjusting the charge state of the cluster accordingly. The effects observed in the isolated point defects could also occur in the larger defect systems. Therefore, the highly mobile hexa-interstitial cluster has been studied in different charge states to observe if charge localisation has an effect in larger clusters.

The predicted durability of a ceramic waste form could be overestimated from simulations if charge localising effects were present in the larger clusters. The mobility of large defect clusters that is observed in the TAD calculations, which is ignored in Monte Carlo simulations, means that the evolution predicted by Monte Carlo simulations is inaccurate. The mobility of large defect clusters could have a significant effect on the durability of the material, affecting the shear strength of the waste form.

The structure of the hexa-interstitial cluster has been studied in three charge states, $(MgO)_3{}^0$, $(MgO)_3{}^+$ and $(MgO)_3{}^{2+}$, to determine if there is a dependence similar to that found for the isolated defects. The migration barrier for each of these charge states has been calculated for comparison to the isolated oxygen interstitial defects.

5.2 Computational method

Plane wave density functional theory has been used to calculate the structure and mobility of the clusters using Vienna *ab initio* simulation package (VASP). The Perdew and Wang (PW91) implementation of the generalised gradient approximation (GGA) was used with projected augmented waves (PAW) pseudopotentials and Γ point sampling of the Brillouin zone. A 3x3x3 super cell, consisting of 216 + defect ions, was used for this research with a simulation cell vector of 12.60 Å. This cell vector was selected as the same cell size was used to confirm the structures and migration barriers obtained through TAD via DFT in reference [86].

The initial structure of the $(MgO)_3$ interstitial cluster was taken from the structure obtained from TAD simulations and was relaxed until the force on each ion was less than 0.01 eV $Å^{-1}$. One or two electrons were then removed from the relaxed structure for the singly and doubly charged cluster, respectively, and relaxed until the force on each ion was less than 0.01 eV $Å^{-1}$.

The migration barriers were calculated using the standard nudged elastic band (NEB) method in VASP. The end point of the path was optimised prior to the NEB calculation using the transition point structure obtained through TAD calculations, using the same method as the initial structure. The NEB calculations were performed using 5 images with a spring constant of 5 eV $Å^{-2}$. Each image was optimised until the forces were less than 0.01 eV $Å^{-1}$.

5.3 Results and discussion

The charge state was found to have a strong effect on the relaxed structure of the interstitial cluster. The neutral interstitial cluster has a relaxed structure (figure 5.1) which is similar to the TAD result. The Bader charge associated with the interstitial ions has a value of ± 1.6, which is consistent with the charge on the lattice ions. The relaxed configuration of the transition point structure is shown in figure 5.2. Figure 5.2 shows the cluster occupying an interplane location, with the cluster becoming more symmetric. Bader analysis shows that no change in charge localisation has occurred in this configuration compared to the initial structure.

The electronic density of states (DOS) of the neutral cluster is shown in figure 5.3. The DOS shows the presence of the interstitial results in the formation of a shallow occupied defect level in the band gap at 0.31 above the valence band maximum (VMB).

The localisation of a hole onto the cluster causes a displacement as an interstitial oxygen forms a dumb-bell with lattice oxygen ($O_2{}^{3-}$) (figure 5.4). The $O_2{}^{3-}$ has an O-O distance of 2.11 Å and analysis of the Bader charges shows that the lattice oxygen donated 0.27e to the interstitial oxygen to form the bond, resulting in a

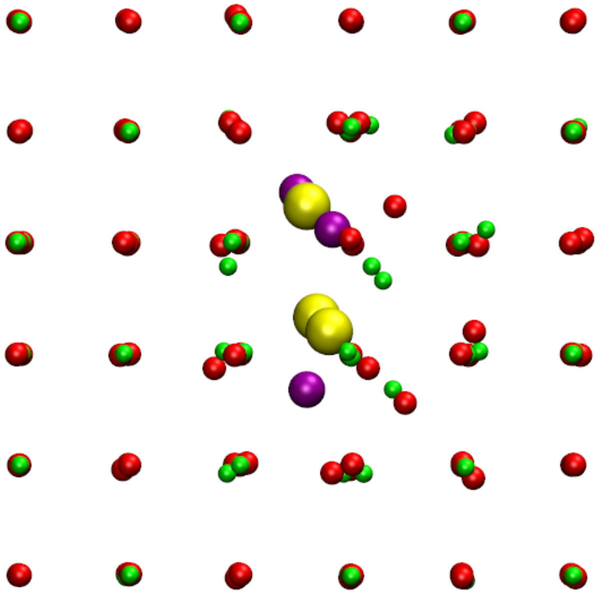

Figure 5.1: Relaxed configuration of the interstitial cluster in the initial position. The red spheres show lattice oxygen ions, green spheres show lattice magnesium ions, yellow spheres show interstitial oxygen ions and purple spheres show interstitial magnesium ions.

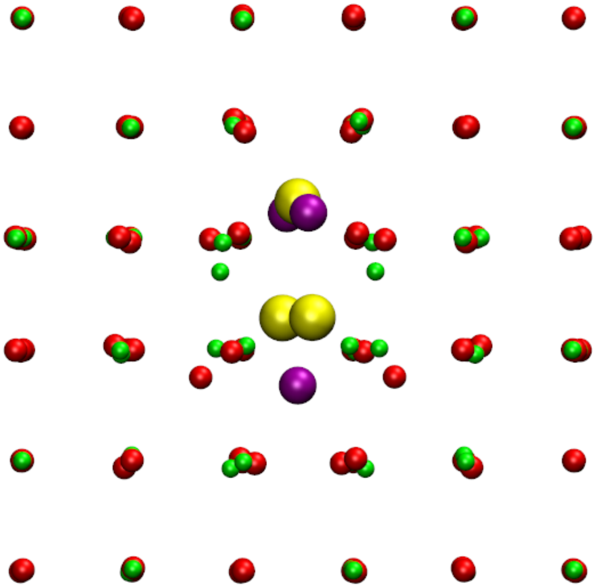

Figure 5.2: Relaxed configuration of the neutral interstitial cluster in the transition point structure.

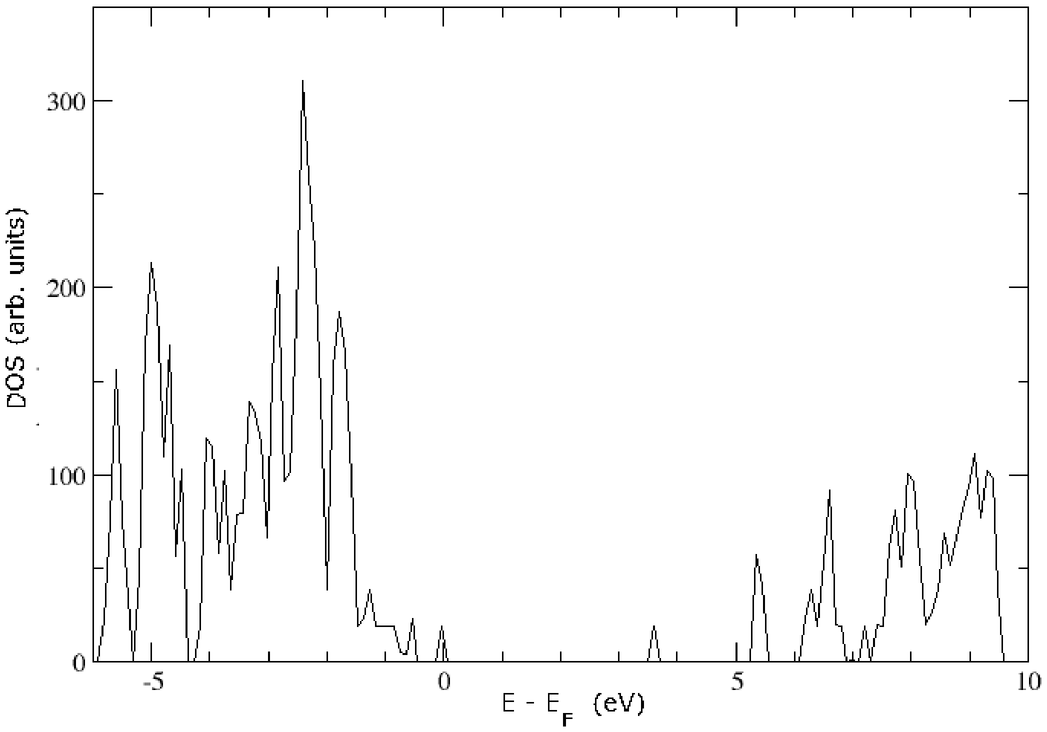

Figure 5.3: The electronic DOS of the neutral interstitial cluster in the initial position, showing the presences of the defect levels at the Fermi level.

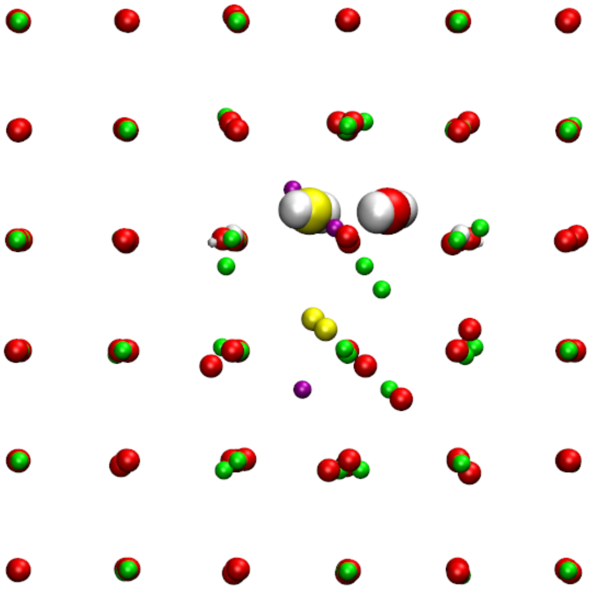

Figure 5.4: Relaxed configuration of the $(MgO)_3{}^+$ interstitial cluster, with isosurface (0.23 e Å^{-3}) showing the localised hole.

charge of -1.3 on each oxygen ion. The effect of charging the cluster results in the relative stability of the initial and transition point structure to become equal, with the transition point structure having the same energy as the initial structure. The transition point structure has the hole localised on the two oxygen halves of the cluster with a dumb-bell formed between the lattice oxygen and an interstitial oxygen, with an O-O separation distance of 2.03 Å.

The DOS for the singly charged cluster (figure 5.5) shows that there are 3 defect levels in the band gap and all three are occupied. The defect levels behave differently in the different spin states, with two of the levels merging in the up-spin state, whereas they remain separated in the down-spin state. The up-spin defect levels ate 0.42 and 1.00 eV above the VBM, while the down-spin states occur at 0.34, 0.57 and 0.91 eV above the VBM. The localisation of the whole on the cluster results in a small shift in the position of the defect levels in the band relative to the neutral cluster. The defect level at 0.34 eV above the VBM in the singly charged cluster increased in energy by 0.03 eV compared to the position in the neutral cluster.

The localisation of two holes has the effect of changing the lowest energy configuration of the cluster, with the transition point structure becoming the most energetically stable structure. In this configuration the two holes lead to the formation of two $O_2{}^{3-}$ between two interstitial oxygen ions and two lattice oxygen ions, on the same half of the cluster (figure 5.6). The split interstitial distance is 2.04 Å for both dumb-bells. Bader analysis shows that 0.29e and 0.26e were donated from the lattice oxygen ions to the interstitials in the formation of the bond. This increase in electron density donated is the reason for the shorter bond distance compared to the singly charged dumb-bell. The equality in the $O_2{}^{3-}$ bond lengths is the reason for the change in the lowest energy configuration, as the initial structure has the $O_2{}^{3-}$ with an O-O separation distance of 2.03 Å and 2.20 Å. Bader analysis shows that 0.22e was donated by the lattice oxygen ions leading, therefore, to the larger split distances of the dumb-bell because of the weaker covalent bond formed.

Figure 5.7 shows the DOS for the doubly charged cluster, with 3 defect levels in the band gap, in which two are occupied and one unoccupied. The localisation of the two holes changes the position of the defect levels, with defect levels at 0.20, 0.55 and 1.21 eV above the VBM. The second and third levels appear only in the down-spin state. The defect level has decreased in energy by 0.11 eV compared to the position of the level in

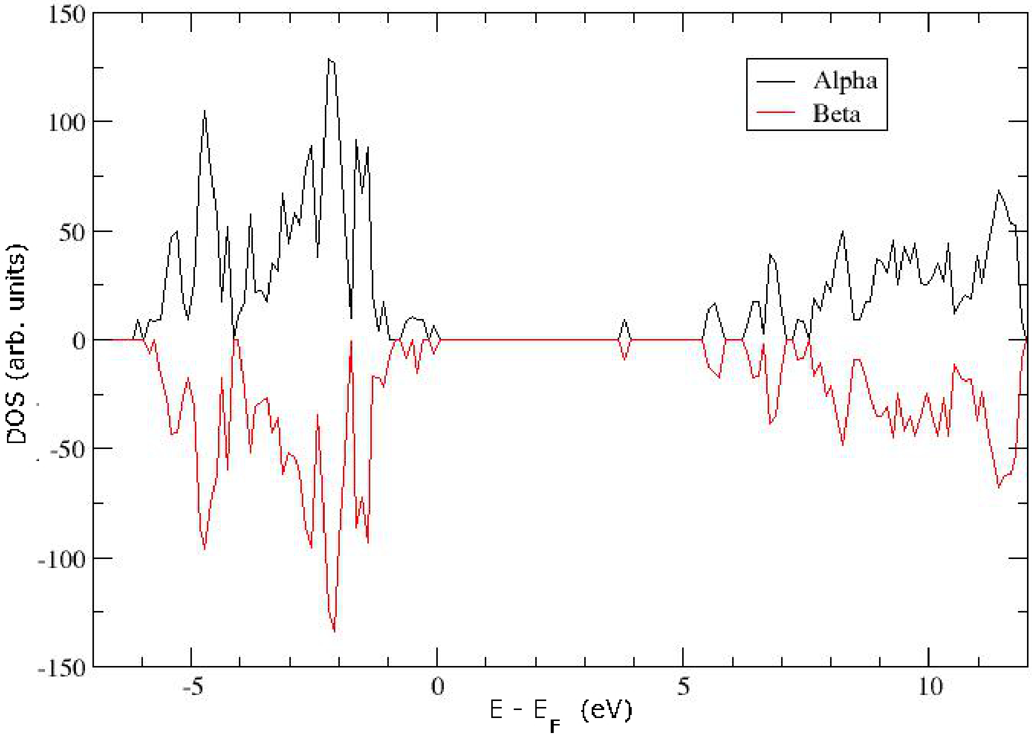

Figure 5.5: The electronic DOS of the singly charged interstitial cluster. Alpha show spin-up states, while beta show spin-down states.

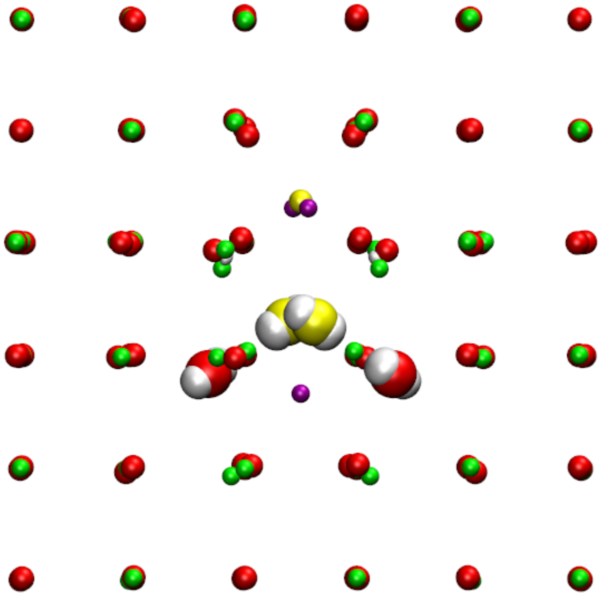

Figure 5.6: The relaxed configuration of the $(MgO)_3{}^{2+}$ interstitial cluster in the lowest energy position. The isosurface (0.29 e Å^{-3}) shows the localisation of the two holes by the cluster.

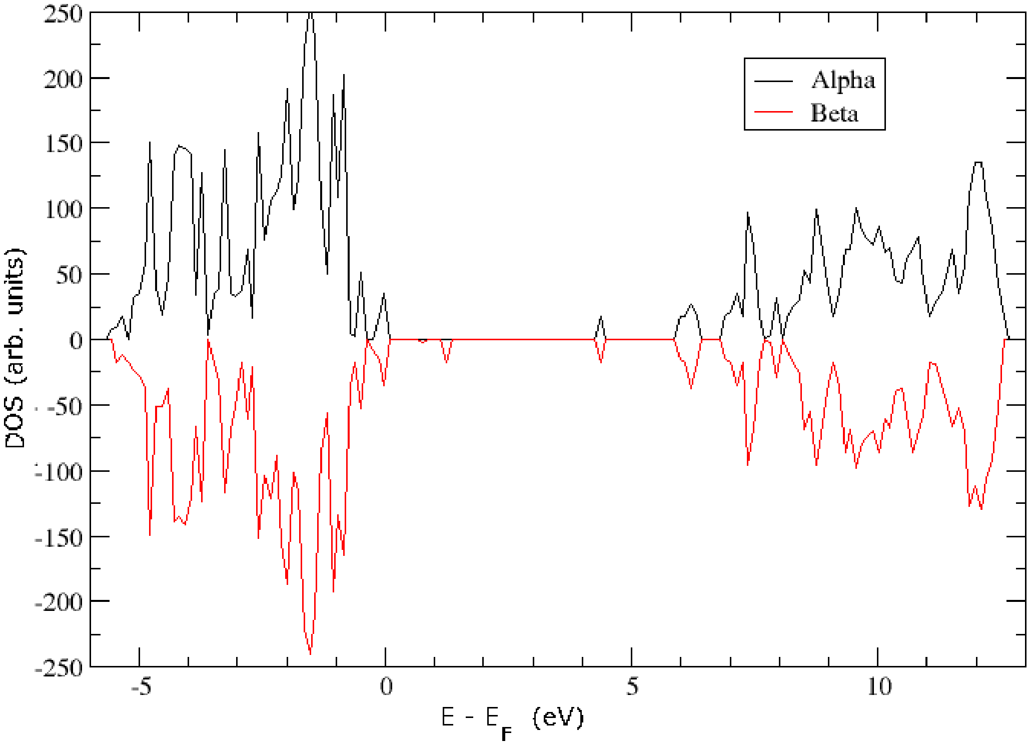

Figure 5.7: The electronic DOS of the doubly charged interstitial cluster.

Table 5.1: Comparison of the cluster structure as a function of charge state.

	$(MgO)^0{}_3$	$(MgO)^+{}_3$	$(MgO)^{2+}{}_3$
6-1-2 (º)	168.59	174.20	172.29
3-4-5 (º)	99.27	98.79	95.44
6-1 (Å)	1.88	1.88	1.87
1-2 (Å)	1.85	1.87	1.87
3-4 (Å)	1.94	1.97	2.01
4-5 (Å)	2.00	2.00	2.00
2-3 (Å)	1.95	1.96	2.17
5-6 (Å)	2.43	2.54	2.19

the neutral cluster.

A comparison of the effect of the localisation of the hole(s) on the structure of the interstitial clusters is made in table 5.1. Figure 8 shows the key to the labels used in the description of the interstitial clusters.

As table 5.1 shows, there is little alteration in the cluster structure caused by charging of the cluster. The only significant change is that the separation between the two halves of the cluster are now equal on both sides of the cluster with the 2-3 distance extending slightly, while the 5-6 distance has significantly reduced.

5.3.1 Hexa-interstitial cluster migration

The migration pathway was taken from the pathway identified through the TAD simulations and it was assumed that the pathway was consistent for each charge state of the cluster. This assumption may not be valid because the pathway was found to be charge state dependent for the isolated oxygen interstitials. However, due to the expense of the NEB calculations and the complicated potential energy surface of the system, it was necessary to assume charge state independence of the pathway for the cluster. A 7-image NEB calculation was performed on the whole path of the neutral cluster to confirm the symmetry in the barrier as observed through TAD (figure 5.9). The barrier was equal either side of the transition point and so to get a more detailed description of the pathway, only the barrier between the initial and the transition structure was calculated in the NEB calculations, figure 5.10.

The migration barrier of the neutral cluster is 0.32 eV, compared to the 0.33 eV barrier observed through the TAD simulations. A barrier of 0.33 eV was achieved if 7 images were used in the NEB calculations, however the extra computational cost for 0.01 eV was not considered necessary. The pathway involves the movement of the central ions of the cluster via a pivot into the transition point configuration. Figure 5.11 shows the initial, saddle point and transition point structure along the pathway of the neutral cluster. There was no change in the electronic distribution at the transition point compared to the initial structure.

The localisation of the hole on the cluster leads to a decrease in the migration barrier, with a barrier of 0.18 eV for the singly charged interstitial cluster. Figure 5.12 shows the initial, saddle point and transition point structures for the pathway. Analysis of the Bader charge shows that there is a redistribution of electron density at the transition point with $O_2{}^{3-}$ in the initial configurations breaking. The lattice oxygen of the dumb-bell regains 0.22e that it had donated to the interstitial resulting in a charge of -1.38, with the interstitial oxygen returning to the charge of the neutral cluster. The hole has been transferred to the half of the cluster with the two oxygen ions, with the formation of another $O_2{}^{3-}$ between a lattice and interstitial oxygen ions. At the transition point the lattice oxygen only donates 0.12e to the interstitial oxygen.

The localisation of the second hole on the cluster results in an increase of the migration barrier, as the migration barrier for the doubly charged cluster is 0.39 eV. This trend of increasing barrier height when the second hole is localised was also seen for the isolated oxygen interstitials, although the increase is not as dramatic for the cluster as it was for the isolated interstitial. Studying the isosurface shows that the saddle point

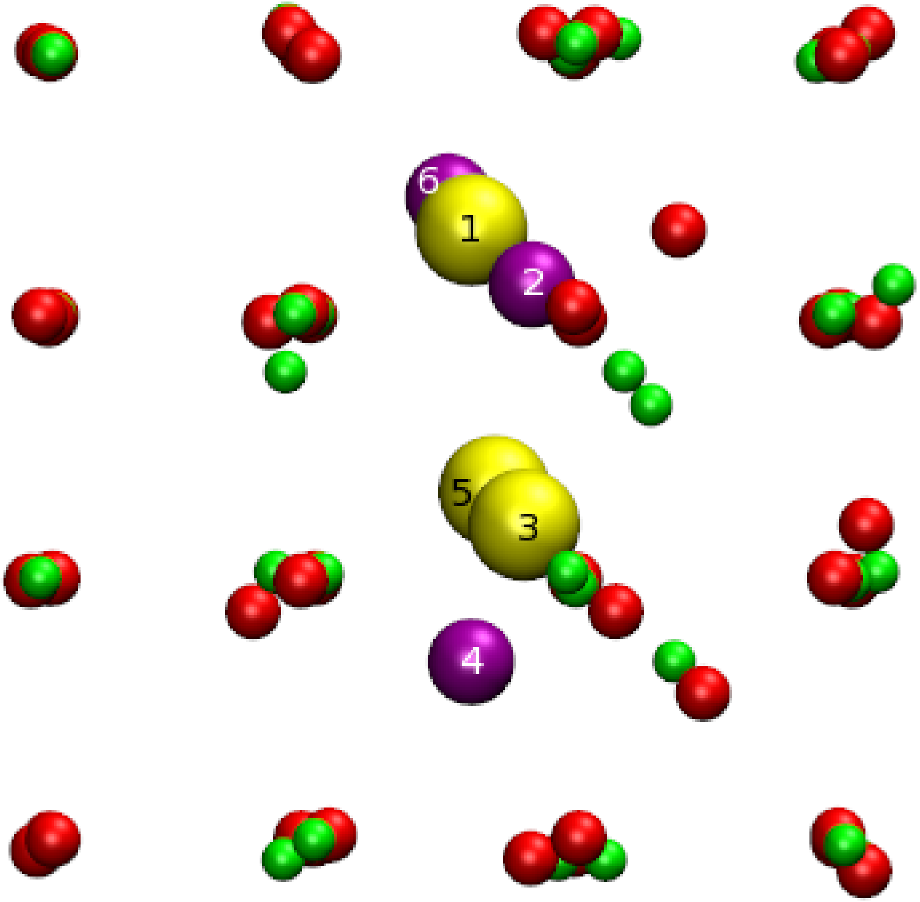

Figure 5.8: Labels of interstitial ions for table 5.1

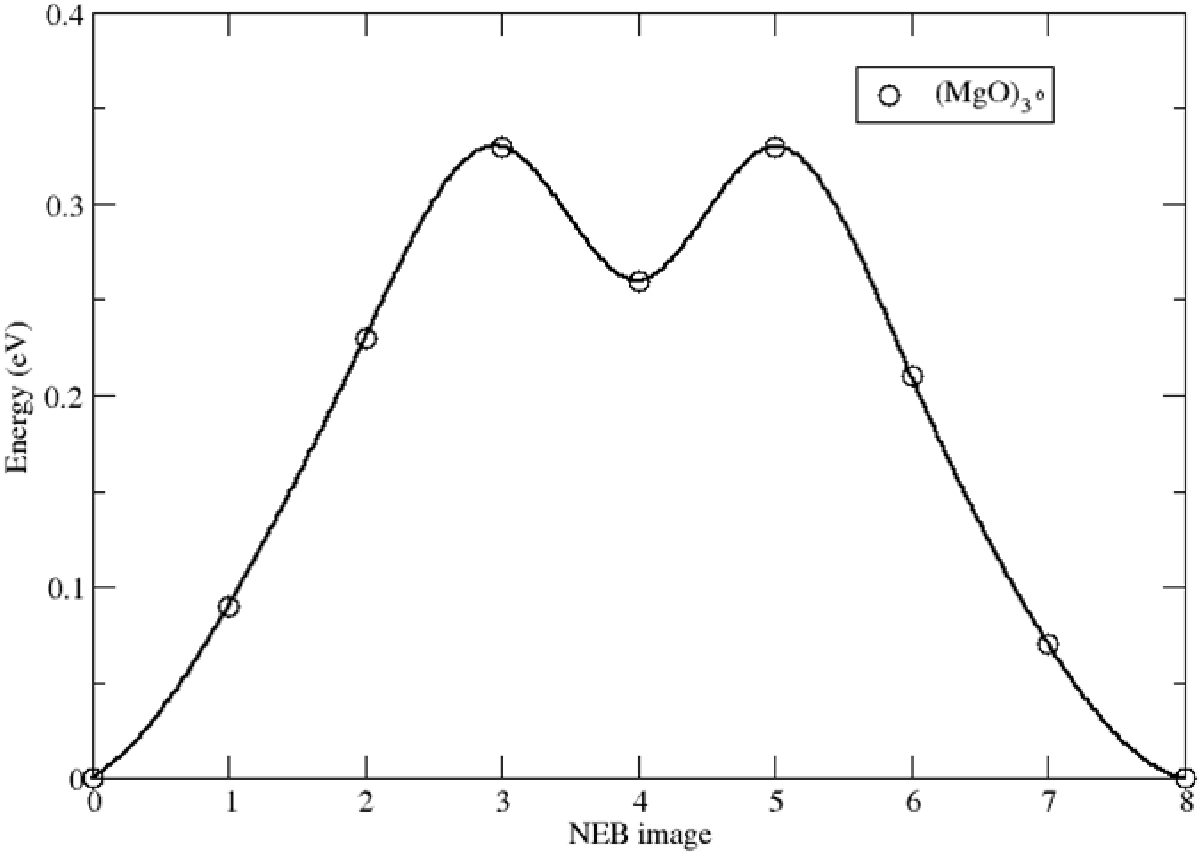

Figure 5.9: Migration barrier of the neutral interstitial cluster through the whole migration path.

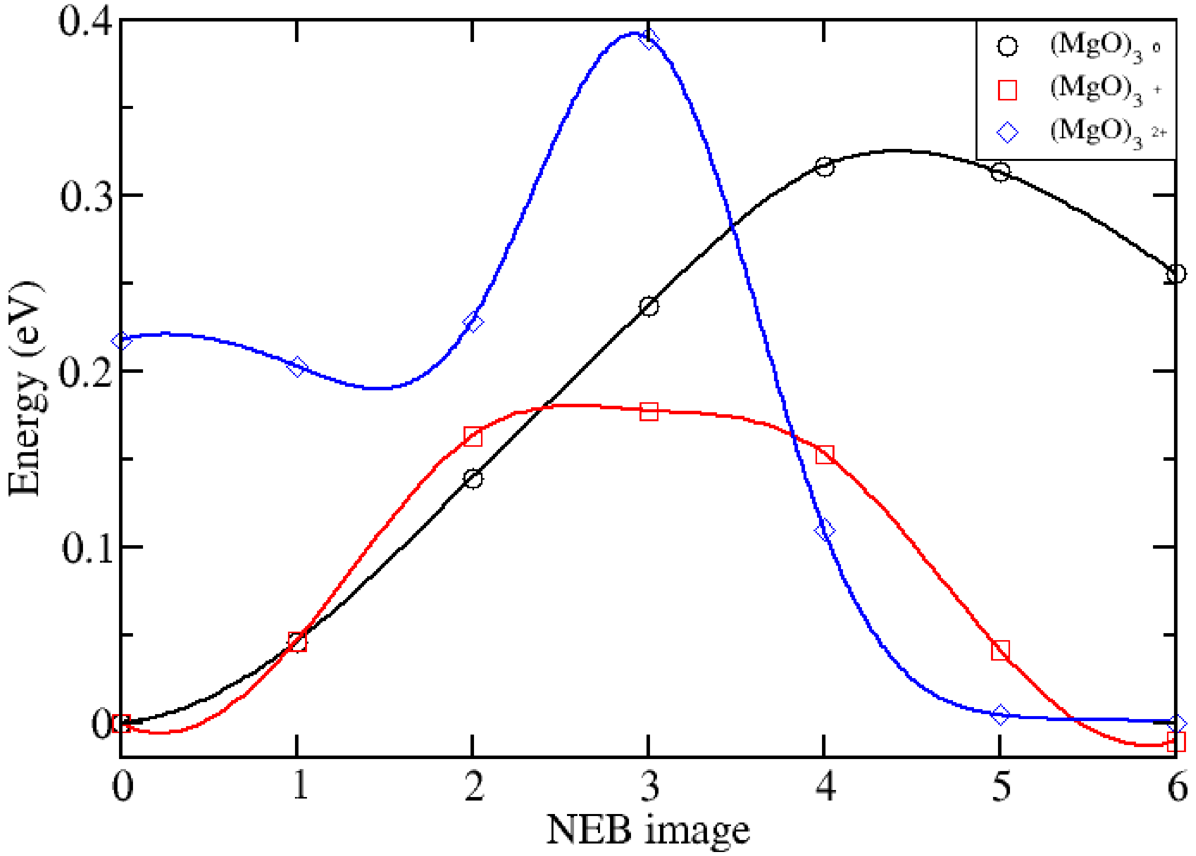

Figure 5.10: Migration barriers of the $(MgO)_3{}^0$(circles), $(MgO)_3{}^+$(circles), $(MgO)_3{}^{2+}$(circles) interstitial clusters.

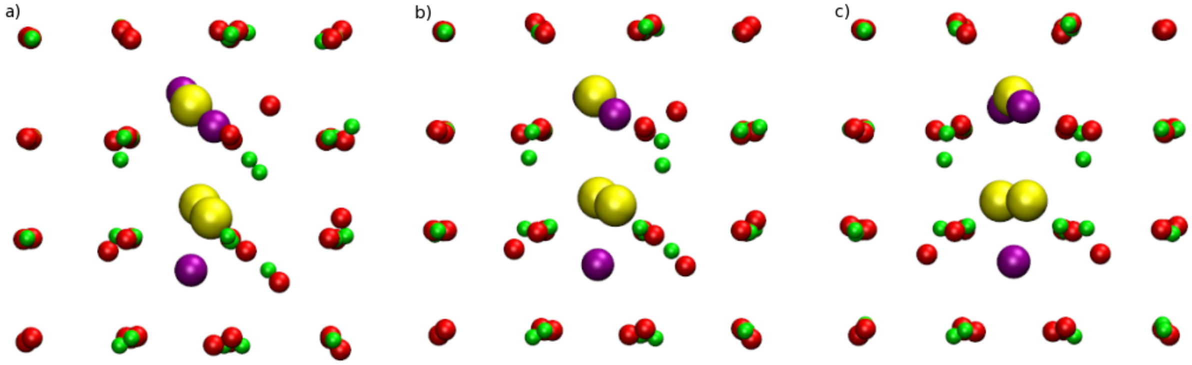

Figure 5.11: The migration pathway of the $(MgO)_3{}^0$ cluster, showing a) the initial, b) saddle point and c) final structures.

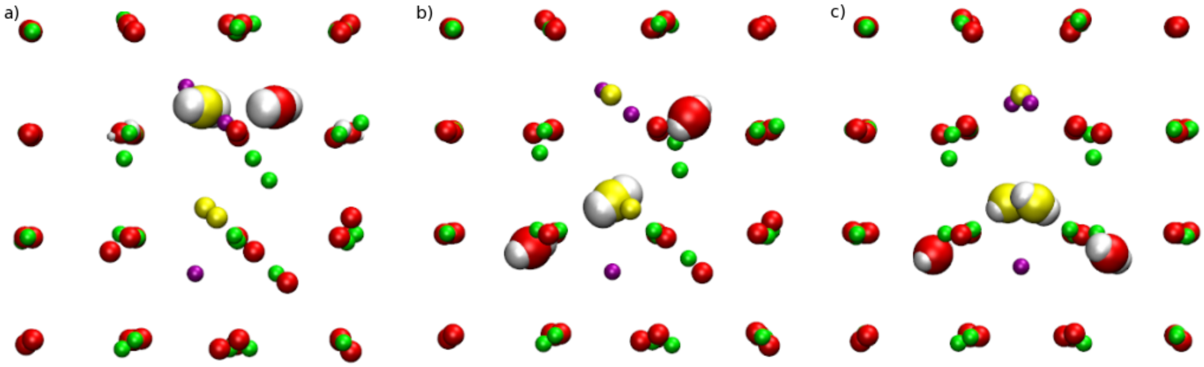

Figure 5.12: The migration pathway of the $(MgO)_3{}^+$ cluster, showing a) the initial, b) saddle point and c) final structures with isosurface at 0.23 e Å^{-3}.

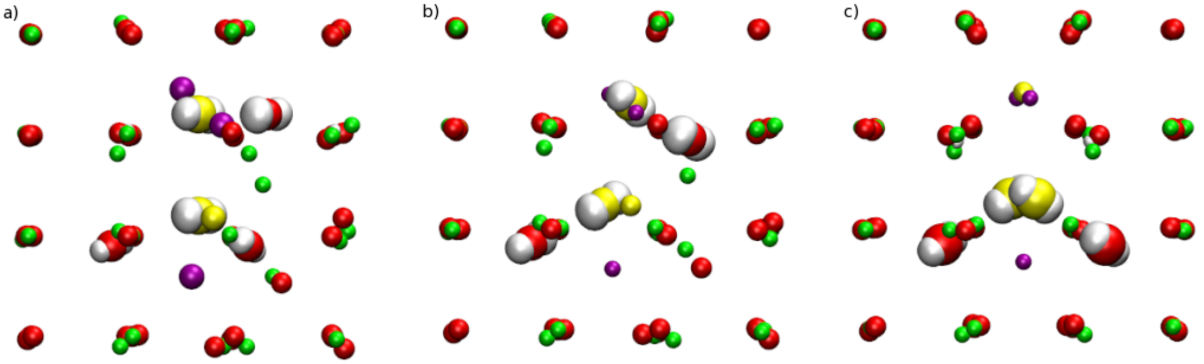

Figure 5.13: The migration pathway of the $(MgO)_3{}^{2+}$ cluster, showing a) the initial, b) saddle point and c) final structures with isosurface at 0.29 e Å^{-3}.

structure corresponds to the configuration when the $O_2{}^{3-}$ on the one oxygen half of the cluster breaks and the hole transfers to the two oxygen half of the cluster, so both holes are localised on the same half of the cluster. The transfer of the trapped hole can be observed in the Bader charges, with a loss of 0.32e and 0.27e on the interstitial and lattice oxygen, respectively, where the hole now localises. This coincides with the gain of 0.29e and 0.25e on the interstitial and lattice oxygen from the breaking of the $O_2{}^{3-}$, respectively. The Bader analysis indicates that the hole is transferred before it is observed in the spin density calculation. This is due to the method of calculating the Bader charge and the division of the charge density into different atomic regions. The spin density is more diffuse in the transition state geometry than in the images either side of the transition point and it is believed that this may be the cause of the disagreement. Figure 5.10 appears to show the presence of a local minimum between image 1 and 2 of the NEB calculation, to investigate this local minimum the number of images was increased to 7 with an image in the position of the minimum. This larger NEB gave the energy of that configuration of 0.20 eV, so shows that the local minimum was a function of the cubic spline used to illustrate the barrier.

The TAD simulations observed that the hexa-interstitial cluster could become pinned by a trivalent ion in the lattice, such as Al, preventing the cluster from diffusing.[136] This led to the statement that the effect of the mobile cluster would be insignificant in a real crystal, because of impurities of Al in experimental samples of MgO. However, if the hole localises on the oxygen ion of hexa-interstitial binding to the Al impurity, it would reduce the binding between the Al and O.

5.4 Conclusion

The effect of the charge localisation on the structure and mobility of the hexa-interstitial cluster in MgO was investigated using DFT. It was found that the charge state had an effect on the relative stability of the different configurations of the interstitial cluster, with the neutral cluster having a 0.26 eV difference between the initial and transition state structure. These configurations had the same energy after the localisation of a hole on to the cluster and the localisation of a second hole on the cluster reverses the order of stability found for the neutral cluster, with a difference of 0.22 eV.

The charge state was also found to have a significant effect on the migration barriers of the interstitial cluster. The $(\mathrm{MgO})^{0}{}_{3}$ cluster was found to have a migration barrier of 0.32 eV, in agreement with the barrier observed from TAD simulations, while a migration barrier of 0.18 eV was found for the $(\mathrm{MgO})^{+}{}_{3}$ cluster and the barrier for $(\mathrm{MgO})^{2+}{}_{3}$ was 0.39 eV. The same trend was observed for the isolated oxygen interstitials, with the singly charged defect having the lowest migration barrier.

These results show that the assumption that the large interstitial clusters are immobile used in Monte Carlo simulations is invalid. This implies that the material durability perdicted by Monte Carlo simulations and rate theory are incorrect, as the rate of cluster growth seen will be wrong if these large interstitial clusters are also able to diffuse through the material. Also the rate of defect diffusion towards grain boundaries will also be larger then that seen in the Monte Carlo simulations due to the effects of charge localisation on the defects.

Chapter 6

Point Defects in Zirconolite

6.1 Introduction

The long timescale durability of the ceramic matrix encapsulating the nuclear waste will depend on the evolution of the microstructure over periods of hundreds or even thousands of years, well beyond the timescale of experimental measurements. A detailed understanding of the properties of defects is, therefore, a necessary starting point for the prediction of the long-term durability of the encapsulating ceramics. The observed effects of charge localisation in MgO on both isolated and extended defects, will have a significant effect on the evolution of damage in a material. Therefore, to understand if similar effects are present in an encapsulation ceramic, the effect of charge localisation on defect properties was studied in a real system. The proposed ceramic for the disposal of waste plutonium is zirconolite ($CaZrTi_2O_7$). Zirconolite is proposed as an encapsulation matrix as it is able to accommodate Pu into its lattice structure, on a Ca site, as well as neutron poisons, such as Hf and Gd on a Zr site.

There have been few modelling studies of zirconolite to date due to the complex crystal structure. Classical molecular dynamics simulations of low energy cascades have been performed on uranium loaded zirconolite and displacement energies have been calculated.[114] Experimental analysis of the material has included electron microscopy of natural zirconolite containing actinide species,[97] X-ray diffraction (XRD) of synthesised zirconolite containing Pu or its surrogate Ce,[137, 95] ion beam studies,[95, 98, 11] X-ray absorption studies (XAS),[106] leaching studies[107, 94] and the behaviour of He inside the crystal.[31, 138]

The experimental results, in agreement with natural analogues, have shown that there is little healing of the zirconolite lattice after an irradiation event.[139, 114] This lack of self healing does not affect the retention of the actinide species, with the amorphous state having a similar leaching rate as a crystalline sample.[94] The limited healing of the zirconolite lattice may imply that the Frenkel defects created during the irradiation event are relatively stable, and are therefore low in energy as the driving force for recombination is not present.

Density functional theory (DFT) has been used to calculate the fundamental properties of intrinsic point defects (vacancies and interstitials) in zirconolite. The complex crystal structure of zirconolite makes it challenging to predict the stable configurations of interstitial ions, therefore we use the *ab initio* random structure search (AIRSS) technique. AIRSS has been used successfully for locating novel crystal structures[140, 141, 142] and has been shown to be proficient in deducing point defect structures.[143, 144] We investigate the effects of trapped charge on the defect conformations and formation energies.

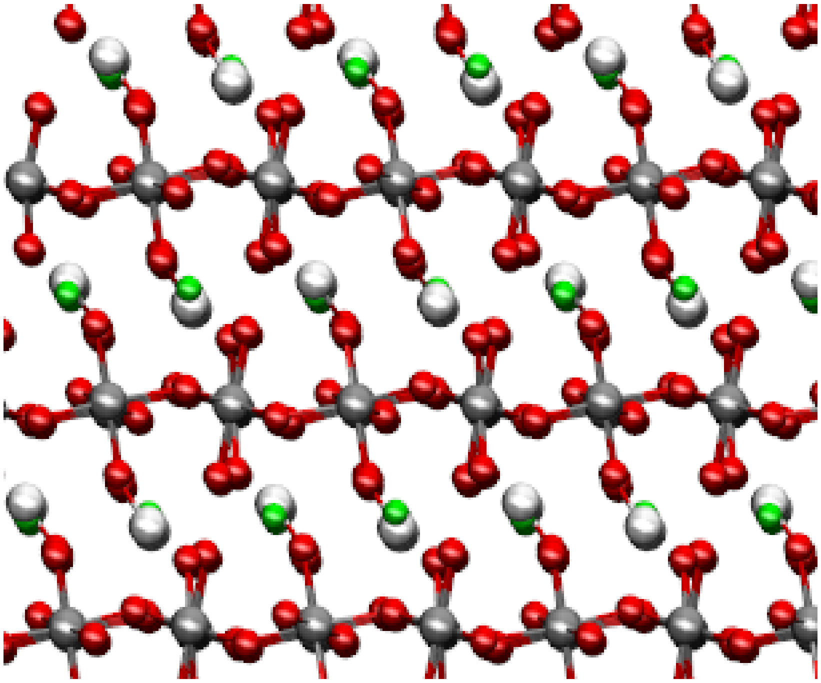

Figure 6.1: Structure of bulk zirconolite projected in the [010] direction. Red spheres show O ions, grey spheres show Ti ions, white spheres show Zr and green spheres show Ca ions. [3] Copyright 2011 by the American Physical Society.

6.2 Computational method

Zirconolite has a monoclinic crystal structure consisting of rows of 6- and 5-fold coordinated Ti-O polyhedra separated by alternating layers of Ca and Zr ions (figure 6.1).

The crystal structure was obtained from XRD experiments performed by Rossell.[2] Zirconolite can exist in a number of different stoichiometries,[2, 145] $CaZr_xTi_{3-x}O_7$, where $0.80 < \; < 1.37$, but a value of x=1 has been used in this research to minimise the size of the simulation cell. Experimental studies of zirconolite have detected a 5-fold coordinated Ti ion instead of the 4-fold coordinated Ti ion in the DFT structure. Our DFT calculations shows that the coordination of the third Ti ion could be increased by altering the stoichiometry of the zirconolite structure. Substituting one Zr ion per unit cell by Ti (= 0.875) results in the substitutional Ti ion becomes 5-fold coordinated. A unit cell with an excess of Zr (= 1.125), created by substituting one Ti ion per unit cell by a Zr ion, results in the two 4-fold coordinated Ti polyhedra in the same layer as the extra Zr ion becoming 5-fold coordinated. Therefore $CaZr_{1.25}Ti_{1.75}O_7$ must have the excess two Zr ions in different Ti layers to remove the 4-fold coordinated Ti polyhedra. However, this was not the case for the DFT-D3 calculations, with the third Ti ion having a 5-fold coordination with x=1 in agreement with the experimental result. The incorrect structure predicted by DFT method is believed to be caused by the structure becoming trapped in a local minimum during the cell optimisation and was therefore unable to locate the global minimum.

6.2.1 DFT method

The periodic plane wave DFT calculations were performed using the VASP code[124, 125] with the Perdew-Burke-Ernzerhof (PBE) exchange-correlation functional,[146] as it gave better agreement with the observed lattice parameters than the PW91 implementation. Projector Augmented Wave (PAW) pseudopotentials were used with a single k point sampling of the Brillouin zone at the Γ point, corresponding to a Brillouin zone sampling of 0.07Å^{-1} with a basis set containing plane waves up to an energy of 600 eV. The k point mesh was

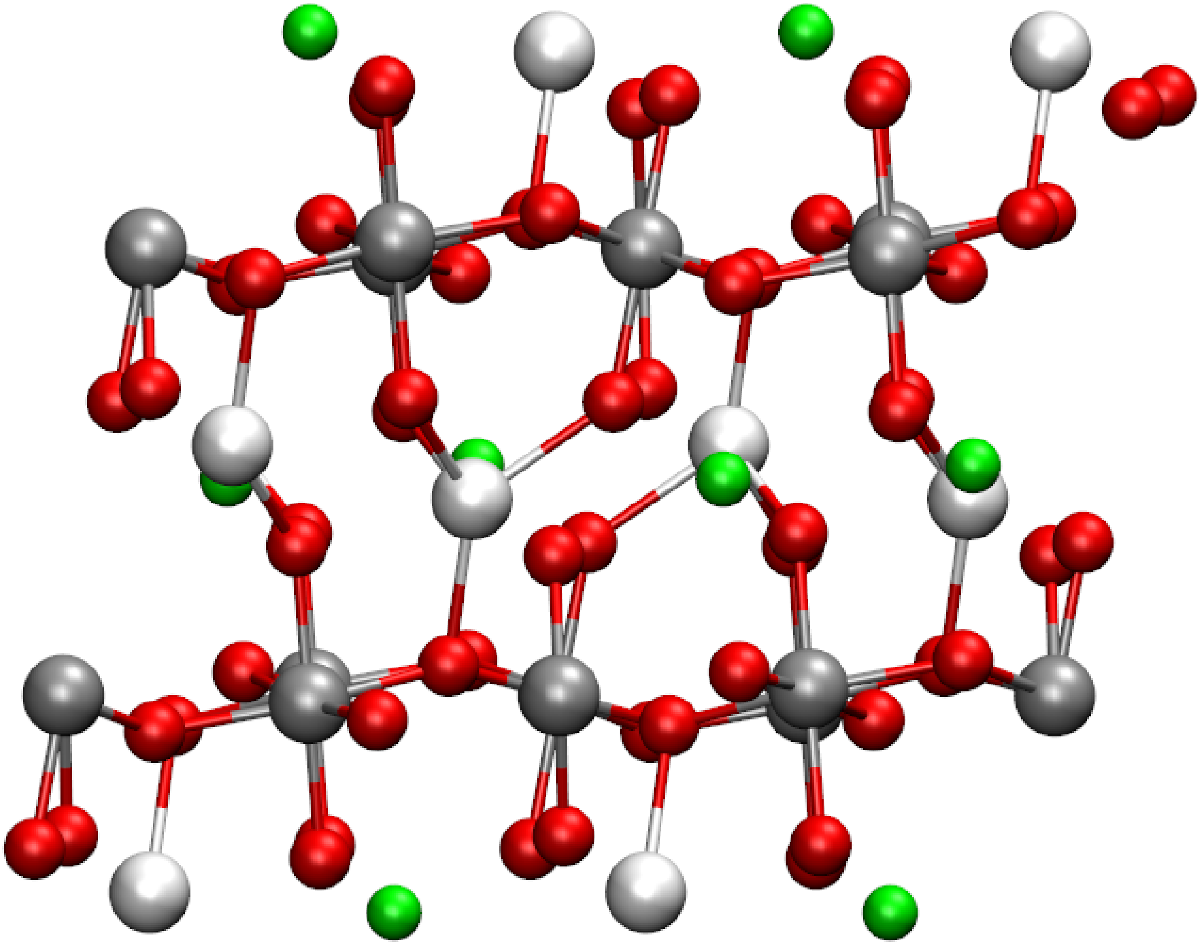

Figure 6.2: 176 ion supercell used in the DFT calculations

converged by running the geometry relaxation with three different k point meshes, the results are summarised in table 6.1. As Table 6.1 shows, the structure relaxation is converged at the Γ point and the energy difference is small enough for the computational cost saving to justify the use of Γpoint sampling. A 1x2x1 supercell containing 176 ions was used in this work (figure 6.2). Relaxation of the cell volume resulted in relaxed lattice parameters that are in reasonable agreement with those obtained by Rossell using XRD experiments, (table 6.2).[2] The defects were then introduced into this cell and the structure relaxed with the lattice parameters fixed.

6.2.2 DFT-D3 method

The 88 ion unit cell was used in this work. The structure was relaxed using the periodic DFT CP2K code,[61] the revised PBE functional along with Grimme's D3 dispersion correction[62] and DZVP basis sets.[61] Struc-

Table 6.1: Convergence of zirconolite *k* point mesh.

Mesh	Energy (eV)	Largest displacement from experimental structure (Å)
1x1x1	-1496.553	0.651
2x2x2	-1496.689	0.648
3x3x3	-1496.618	0.647

tures were considered to be relaxed when the forces on all atoms were less than 0.025 eV $Å^{-1}$. The CP2K code uses Γ point sampling of the Brillouin zone. The relaxed cell vectors were in good agreement with the XRD experiments (table 6.2).[2]

6.2.3 Interstitial defects

The complicated crystal structure of zirconolite presents problems for modelling interstitial point defects because it is difficult to predict the stable configurations. In this study, an efficient random search technique (AIRSS) was employed to identify energy minima for the DFT method only. Interstitial atoms were placed randomly within the simulation cell and the ionic positions are structurally relaxed within VASP . Once a local minimum is located the process is repeated until the required number of minima are found, then the local minima are sorted by energy. The lowest energy interstitial sites were identified from 100 random searches for each interstitial defect. This involved insertion of an additional atom, with the number of electrons corresponding to the desired charge state, at randomly generated coordinates, in an 88 ion unit cell. The 89 ions were relaxed until all the forces were less than to 0.1 eV $Å^{-1}$. The 20 lowest energy configurations resulting from the 100 searches were identified and these were further relaxed until the forces were less than 0.01 eV $Å^{-1}$. The lowest energy interstitial configuration was identified from these 20 searches. The interstitial was inserted into the larger 176 ion supercell and the ions relaxed until the forces were less than 0.01 eV $Å^{-1}$ using the small core pseudopotentials for the Ca ions and a harder O pseudopotential. The interstitial energies from this larger cell were used to calculate the Frenkel defect energies.

6.2.4 Vacancies

6.2.4.1 DFT

The vacancies were created by removing the corresponding lattice ion from the 176 ion cell before relaxing all the ions, with the lattice vectors fixed, until the forces were less than 0.01 eV $Å^{-1}$ on each atom. The number of electrons in the cell was adjusted to obtain the required oxidation state. Each of the vacancy species was studied with a charge ranging from 0 to the formal charge of the vacancy (i.e. for the Ti vacancy the Ti atom was removed and 0, 1, 2, 3 or 4 electrons added to the cell). The VASP code introduced a neutralising background charge when the system was not charge neutral.

6.2.4.2 DFT-D3

The vacancy structures were obtained by the removal of the corresponding atom from the unit cell with the addition of a ghost atom inserted into its place. The purpose of the ghost atom is to avoid basis set superposition error (BSSE), which is introduced when energies are derived from the comparison of calculations which have used different number of basis functions. The introduction of the ghost basis set keeps the same number of basis functions in the vacancy and bulk calculations, allowing accurate defect energies to be calculated from the difference between the energies of the two calculations. The charge state and multiplicity of the vacancy was specified prior to the optimisation. A He ghost basis set was placed in the lowest energy He interstitial position during the bulk and the vacancy defect optimisations. The position of the ghost atoms were kept fixed. We note that the effect of the ghost basis is very small as the basis sets used were developed to have a small BSSE through the inclusion of rather diffuse Gaussian primitives.

6.3 Results and discussion

The band gap calculated for zirconolite in the DFT simulations was 2.8 eV, which is 0.8 eV less than the experimentally obtained value of 3.6 eV.[147] This compares to a band gap of 3.0 eV predicted in the DFT-D3.

Table 6.2: Lattice parameters calculated by DFT and DFT-D3, compared to experimental XRD values obtained by Rossell.[2]

Lattice parameter	DFT (Å)	DFT-D3 (Å)	Experimental (Å)	% error of DFT	% error of DFT-D3
a	12.09	12.42	12.45	2.89	0.24
b	7.07	7.42	7.27	2.82	2.06
c	11.08	11.42	11.39	2.72	0.26
Volume (Å^3)	931.41	1035.92	1014.06	8.15	2.16

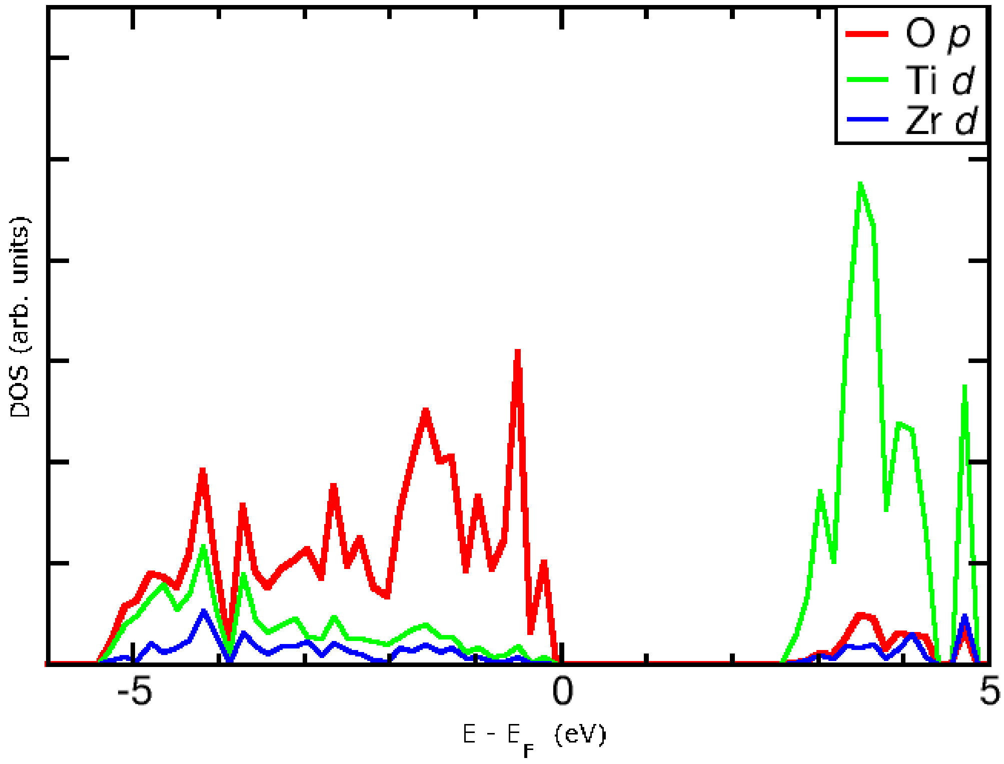

Figure 6.3: Partial DOS of bulk zirconolite. Red shows oxygen *p* orbitals, green shows titanium *d* orbitals and blue shows zirconium *d* orbitals. [3] Copyright 2011 by the American Physical Society.

This is in line with the general tendency of DFT to underestimate band gaps in insulators.[57, 148] A study of the partial DOS from DFT has shown that the edge of the valence band is constructed from the *p* orbitals from the oxygen ions, while the conduction band edge is constructed from Ti *d* orbitals (figure 6.3). This is in agreement with the DOS calculated from the DFT-D3 calculations. The zirconolite band gap is close to the band gap of TiO_2, which is 3.0 eV for rutile and 3.2 eV for anatase,[149] compared to 5.32 eV for ZrO_2[150] and 7.03 eV for CaO.[151] These different band gaps of the constituents explain the relative positions of the Ti and Zr *d* orbitals in zirconolite. The dominance of the band gap edges by Ti and O orbitals may imply that the electronic behaviour of zirconolite should be similar to TiO_2.

6.3.1 Interstitials

The lowest energy configuration of the neutral oxygen interstitial is dependent on the size of the simulation cell and, therefore, the defect concentration. A <111> ${O_2}^{2-}$ interstitial was the lowest energy configuration identified within the 88 ion cell, with a lattice oxygen from a 6-fold coordinated Ti polyhedron forming the second atom of the split interstitial (figure 6.4a). The ${O_2}^{2-}$ has also been identified as the lowest energy configuration for a neutral oxygen interstitial in MgO (figure 4.2) and a number of other oxides.[152, 153, 154] In zirconolite the oxygen atoms of the ${O_2}^{2-}$ have a separation distance of 1.5 Å. Bader analysis[66] of the relaxed structure shows that 0.48e is transferred from the lattice oxygen to the interstitial, resulting in a charge of -0.57 on both oxygen atoms of the dumb-bell. The split dumb-bell distance is larger than the dumb-bell in MgO, which had a bond distance of 1.42 Å. The shorter distance for the MgO ${O_2}^{2-}$ is due to the larger amount of electron density donated (0.8e compared to 0.57e) from the lattice oxygen to the interstitial ion. The formation of the ${O_2}^{2-}$ creates a defect level which resides 0.29 eV above the valence band maximum (figure 6.4c). However, a different interstitial configuration was formed in the 176 ion cell. In the larger cell, the

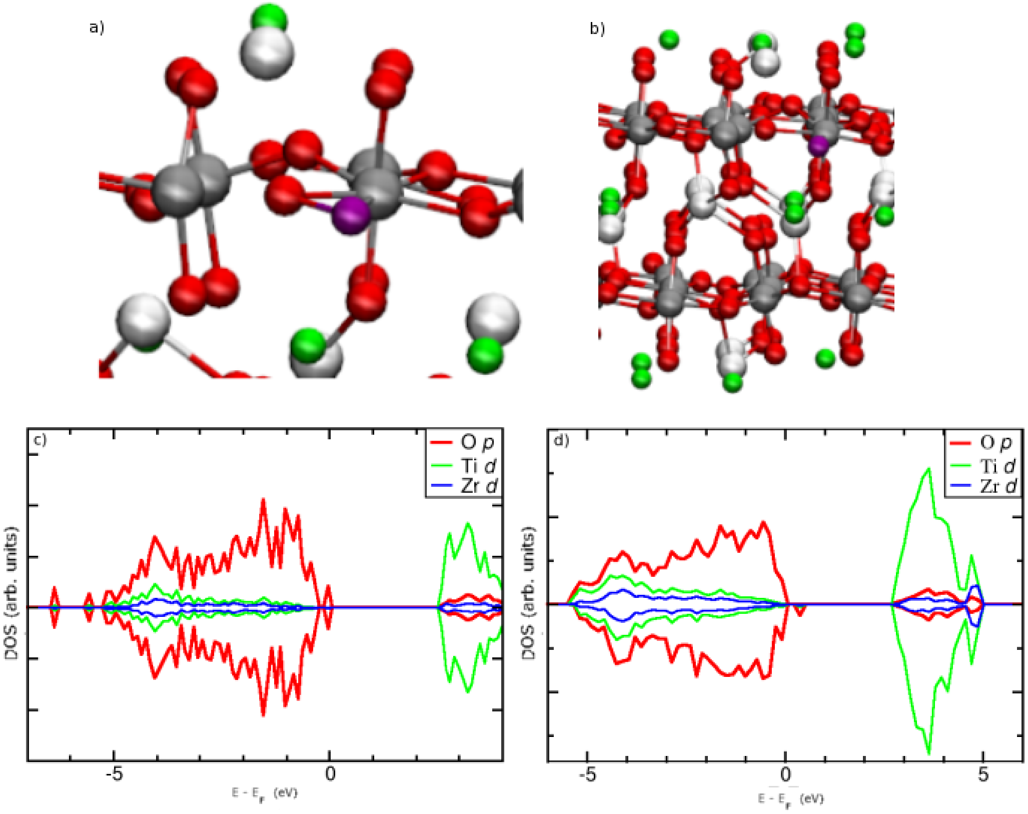

Figure 6.4: The relaxed configuration of the O^0 interstitial in a) an 88 ion unit cell and b) a 176 ion supercell. The purple sphere shows the interstitial. Partial DOS from c) the 88 ion unit cell and d) the 176 ion supercell. The upper and lower parts of the DOS plots represent values for spin-up and spin-down electrons, respectively. [3] Copyright 2011 by the American Physical Society.

interstitial results in the increase in the coordination of two 6-fold coordinated Ti ions to 7-fold coordinated, with the maximum Ti-O bond length defined as 2.2 Å. The interstitial also increased the coordination of all of the 4-fold coordinated Ti, with three increasing to 6-fold coordination and the remaining five to 5-fold coordination (figure 6.4b). Two unoccupied defect levels form in the band gap, 0.40 eV and 0.69 eV above the valence band for this defect configuration (figure 6.4d).

AIRSS located a defect structure for the singly charged oxygen interstitial that was not dependent on the cell size. The oxygen ion binds to a 4-fold coordinated Ti polyhedron producing a defective 5-fold coordinated Ti polyhedron (figure 6.5a). Bader analysis shows that no significant electron density is redistributed due to these displacements. The defect level created by the O^- interstitial is 0.54 eV above the valence band (figure 6.5b). The doubly charged oxygen interstitial was found to be unstable, as it relaxed to the same configuration as the singly charged interstitial, with the extra electron delocalised over the cell.

The calcium interstitial was inserted in two different charge states, the neutral and +2, but Bader analysis of the resulting configuration shows that the neutral interstitial lost its electrons, giving a charge state of +1.4, indicating that the calcium interstitial is only stable in the doubly charged state. The doubly charged interstitial also had a charge of +1.4, 0.2e less than the lattice Ca ions. The Ca interstitial resides in the <010> channels which run through zirconolite (figure 6.6a). The formation of the calcium interstitial does not result in the formation of a defect level in the band gap of zirconolite.

The titanium interstitial was also studied in the neutral and the formal charge (+4) states. However in both of these cases the electron distribution was such that the resulting interstitial had a charge of +2, with the neutral

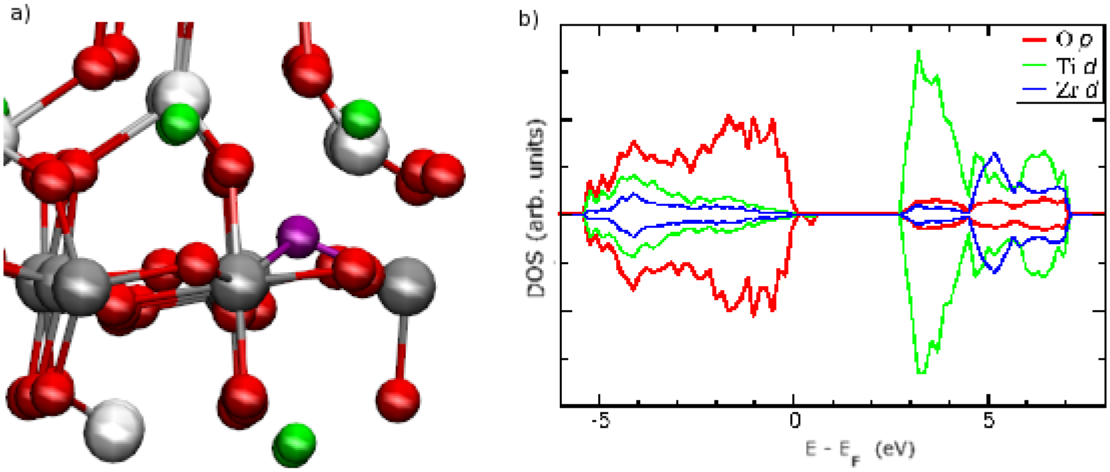

Figure 6.5: a) The relaxed configuration of the O^- interstitial in the 176 ion supercell and b) the partial DOS. [3] Copyright 2011 by the American Physical Society.

interstitial electron density equal to +1.4 and the quadruply charged +1.8. AIRSS was then performed on the doubly charged Ti interstitial and the stable interstitial site was found to be in the <010> channels (figure 6.6b) close to the position of the Ca interstitial, with a Bader charge of +1.6. The Ti interstitial results in the formation of two singly occupied defect levels in the band gap, 2.04 eV and 2.23 eV above the valence band (figure 6.7).

A similar procedure for the zirconium interstitial found that it too exists only in the doubly charged oxidation state, with Bader charges of +1.7 and 2.2 for the neutral and quadruply charged interstitials, respectively. However, in this case AIRSS located an interesting lowest energy structure. The additional zirconium ion displaces a 6-fold coordinated Ti ion from its lattice site and resides on the Ti site. The displaced Ti lattice ion becomes an interstitial ion (figure 6.8). This displaced Ti ion resides in the same position as the Ti interstitial (figure 6.6b) and both have the same Bader charge of +1.61. The bond distances within the polyhedron increase with the substitution of a Zr for a Ti ion (maximum 11.6 %), with one of the O ions displaced away from the polyhedron causing the Zr to be 5-fold coordinated. The substitution of a Ti ion by a Zr ion has been observed previously in pyrochlores[155] and Zr doped TiO_2.[156] The substitutional Zr/Ti interstitial configuration is 0.27 eV more stable than the next lowest energy configuration, which is the Zr interstitial located in the <010> channel.

6.3.2 Vacancies

There are seven different oxygen chemical environments in zirconolite, and vacancies in four of these environments have been studied to observe trends in the oxygen vacancy behaviour. The four environments studied were an oxygen ion which bridges two 6-fold coordinated Ti polyhedra in the <010> direction, an oxygen ion which bridges a 6-fold coordinated Ti polyhedron and a Zr ion (1.99 Å Zr-O), another oxygen ion from a 6-fold coordinated polyhedron bridging a Zr ion (2.14 Å Zr-O) and finally a 3-fold coordinated oxygen ion which bridges two 6-fold coordinated polyhedra in the <100> direction and a Zr ion. The bridge between the two polyhedra localises the excess electrons similarly to anatase (TiO_2) for the neutral and singly charged oxygen vacancy. One of the two excess electrons localises on one of the Ti ions that the oxygen was bridged to, and the other electron is localised on a Ti ion in an adjacent row. The singly charged vacancy localised the excess electron on one of the Ti the oxygen ion was bridging. The DFT partial DOS has been calculated for the three defect charge states and a defect level in the band gap is only present for the neutral vacancy and exists 2.66 eV above the valence band. The defect level is constructed from Ti *d* orbitals. Analysis of the energy levels from this vacancy shows that another defect level exists but is only 0.28 below the conduction band, constructed from

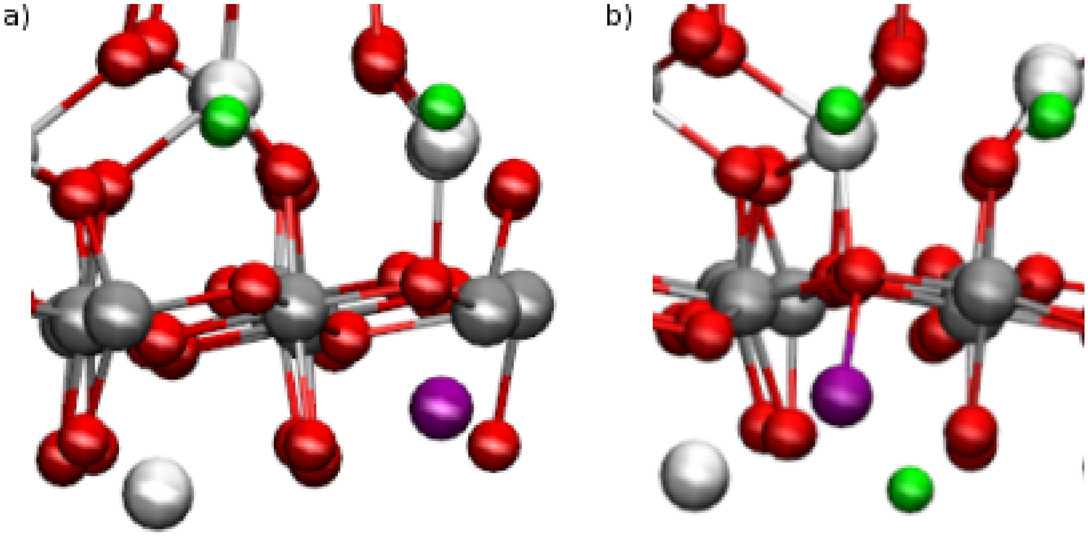

Figure 6.6: The relaxed configuration of a) the Ca^{2+} and b) the Ti^{2+} interstitials located in the <010> channel. [3] Copyright 2011 by the American Physical Society.

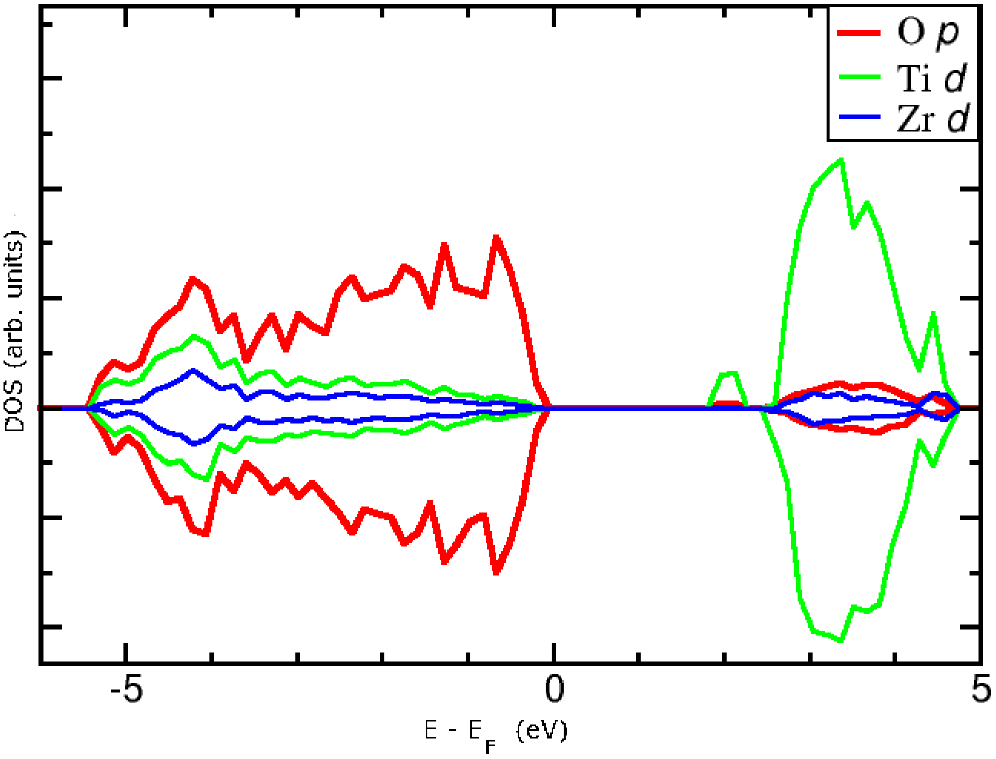

Figure 6.7: Partial DOS of the Ti^{2+} interstitial. [3] Copyright 2011 by the American Physical Society.

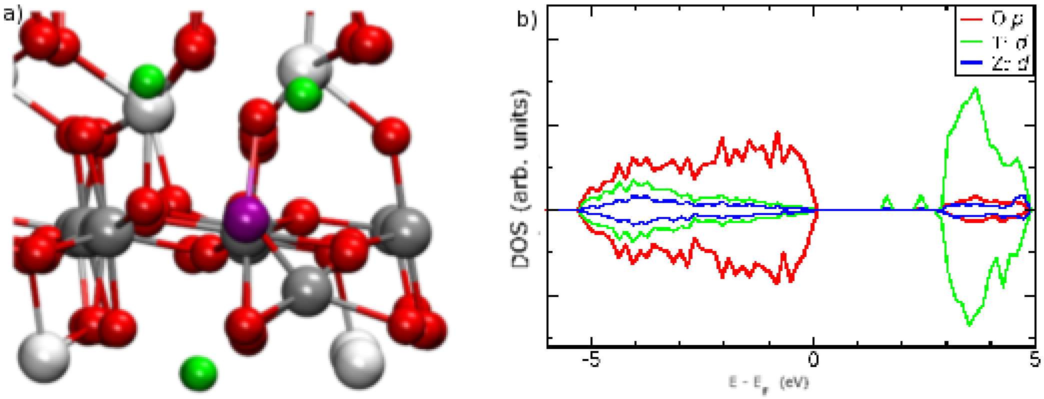

Figure 6.8: a) The relaxed configuration of the Zr^{2+} interstitial, where Zr has displaced the Ti ion into the <010> channel. b) The partial DOS for this defect configuration. [3] Copyright 2011 by the American Physical Society.

Ti *d* states, but is hidden due to the smearing used in the calculation of the DOS.

The second environment, short Ti-Zr bridge, localised the electrons differently for the neutral and singly charged vacancy in DFT. The neutral-vacancy electrons were localised in the same way as the previous environment for both DFT and DFT-D3, where the two electrons localised on two different Ti ions. However, the excess electron from the singly charged vacancy in DFT localises between the Ti and Zr ions, where the oxygen ion was. It is assumed that this is caused by the need to reduce the Coulombic repulsion between the positively charged Ti and Zr ions, however the distance between the ions increases by 2.76%, from 3.62 Å to 3.72 Å due to the presence of the vacancy. This was not the case for the neutral vacancy because the electron had localised on the Ti ion, reducing its charge. The singly charged vacancy in DFT-D3 localises the excess electron on one Ti ion, similar to the first oxygen environment. The neutral vacancy is the only charge state that causes a defect level to be present in the band gap, which resides at 2.25 eV and another level which shoulders the conduction band, 2.68 eV above the valence band. DFT shows both are constructed from Ti *d* orbitals.

The removal of the long Ti-Zr bridge resulted in the neutral vacancy localising the two electrons on two different Ti ions from the same row in the DFT result, while DFT-D3 has the electrons localised in different rows. The singly charge vacancy also localised the unpaired electron on the Ti ion to which it was bonded to, in both DFT and DFT-D3 results. Analysis of the DOS from DFT has showed that there is no defect level present in the band gap for any of the vacancy charge states.

The fourth environment studied, the 3-fold coordinated bridge allowed the assessment on whether the chain direction has an important effect of the structure of the defect. The chain direction does have an effect on the structure of the neutral defect in DFT, as the iso-surface shows that one of the unpaired electrons localises on the Ti ion next to the Ti to which the oxygen was bonded, while the other electron localises between the Ti and Zr ions similar to the second environment, although no bond existed between these ions (figure 6.9). The localisation of the electron between the two ions results in a decrease in the distance between the ions of 1.89%, from 3.18 Å to 3.12 Å. A defect level is present at 2.01 eV above the valence band, the level is constructed from Ti *d* orbitals and also has a contribution from the *d* orbitals of the zirconium ion between which the electron is localised (figure 6.10). The electronic structure from the DFT-D3 calculation has the two electrons localised on two Ti ions in different rows, the same structure as the other oxygen vacancies. The singly charged vacancy localises the unpaired electron on one of the Ti ions the oxygen ion was bridging, in both DFT and DFT-D3 calculations. This localisation has been observed in all of the singly charged oxygen vacancies studied, involving bonding between titanium and oxygen ions only and is therefore expected in the other oxygen vacancies not studied. The localisation of the electron on the Ti ion does not create a defect level

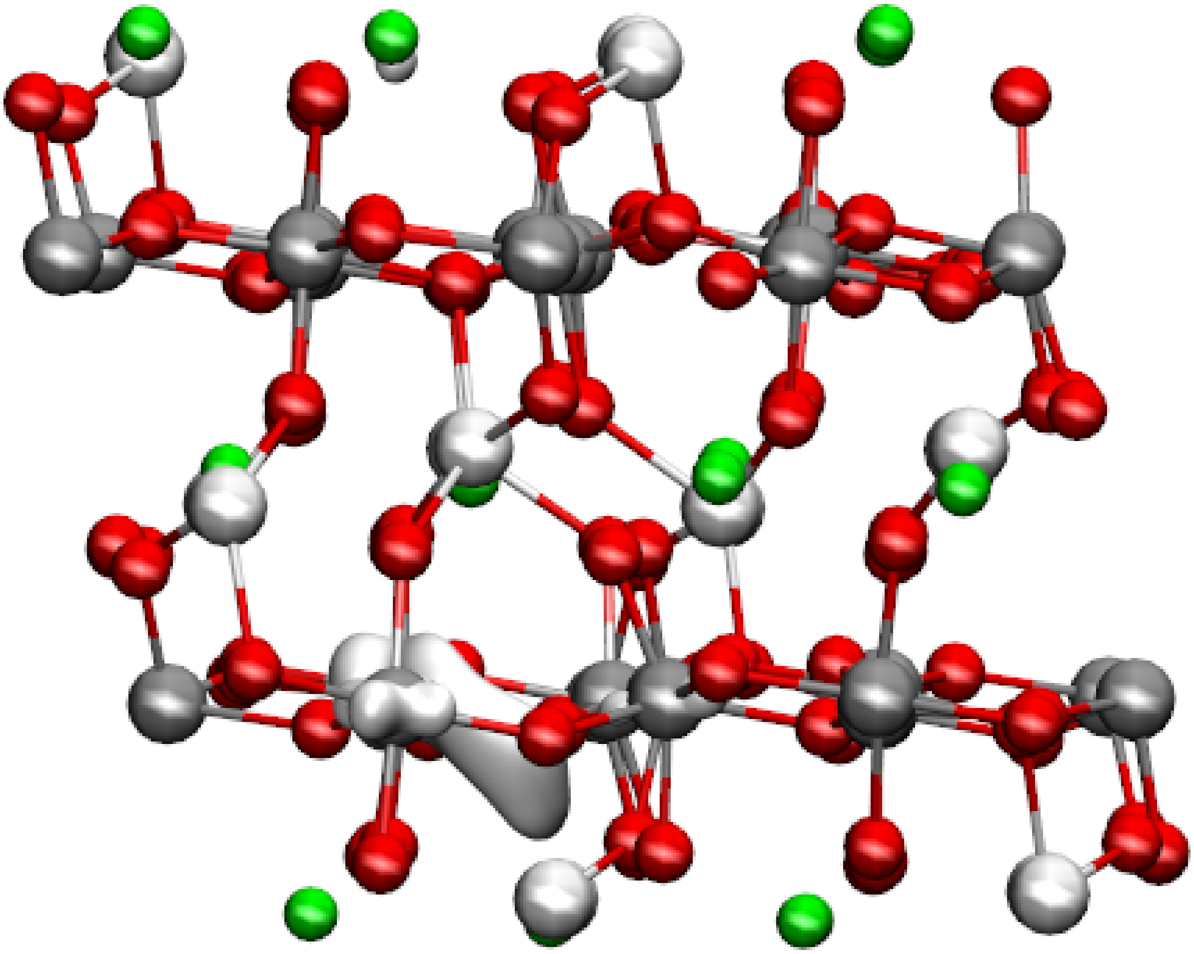

Figure 6.9: The 0.06 e Å^{-3} iso-surface of the neutral oxygen vacancy in the fourth environment. Showing the localised electron between the Ti and Zr ions. [3] Copyright 2011 by the American Physical Society.

in the band gap of zirconolite.

The neutral calcium vacancy localised the two holes present on two oxygen ions in both methods. One of the oxygen ions is next to the vacancy site, while the other oxygen ion is the top of a 6-fold coordinated polyhedron, in which the bottom of the polyhedron is next to the vacancy site. Both of these oxygen ions are 2-fold coordinated. There are no defect levels created in the band gap due to the presence of the vacancy. The singly charged vacancy also localises the hole state on a 2-fold coordinated oxygen in DFT. Whilst the DFT-D3 result has the hole delocalised over two 2-fold coordinated oxygen ions away from the vacancy site, figure 6.11. The localisation of the hole does not result in a defect level being created in the band gap nor is a defect level present for the doubly charged vacancy.

The zirconium vacancy showed significant charge state dependence on the observed defect structure in the DFT calculation, summarised in table 6.3. The neutral defect results in the formation of an oxygen molecule below the vacancy site. The bond distance in this O_2 molecule was 1.24 Å, which compares to 1.22 Å for a free O_2. The phonon frequency of this molecule is 37.99 THz compared to 45.18 THz for the free molecule (1267 cm^{-1} and 1507 cm^{-1}, respectively) showing that the molecule has a weaker covalent bond than the free O_2 molecule. Analysis of the iso-surface showed that there was electron density between the two oxygen atoms, similar to that shown in figure 6.13, indicating that a covalent bond has formed. The vacancy also leads to the displacement by 0.83 Å of a 4-fold coordinated Ti polyhedron out of the Ti row towards the vacancy. The defect

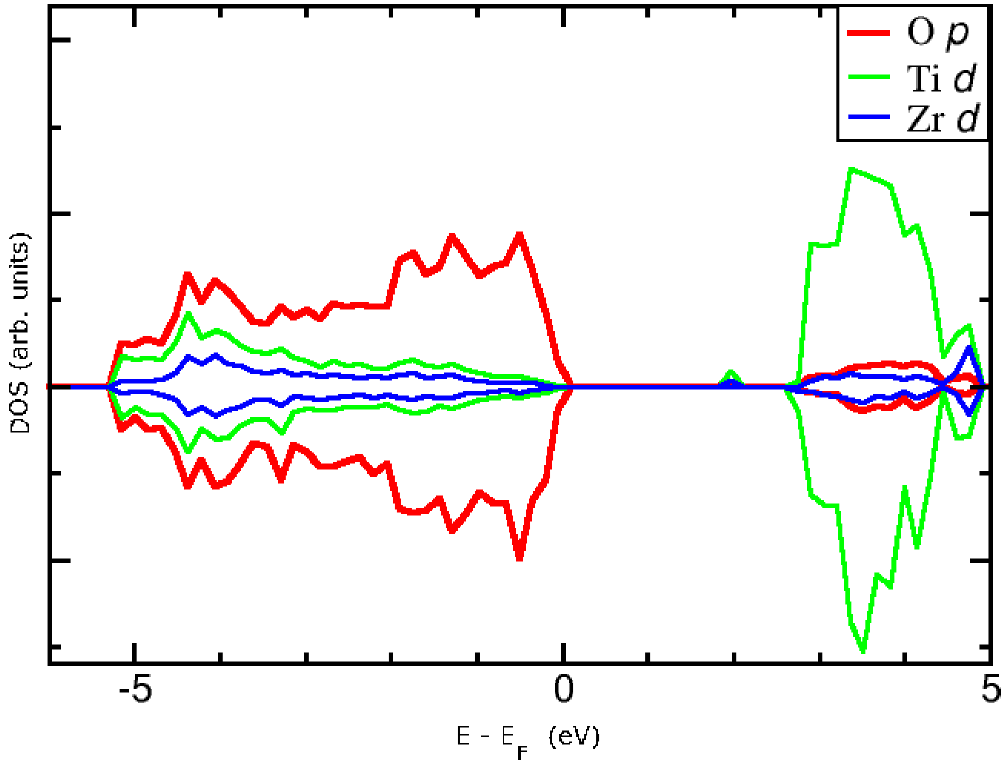

Figure 6.10: Partial DOS of the neutral oxygen vacancy in the fourth environment. [3] Copyright 2011 by the American Physical Society.

structure results in the creation of a defect level 2.28 eV above the valence band constructed from Ti *d* orbitals (figure 6.12). The oxygen molecule gives rise to a defect level 2.36 eV below the valence band. In the results from the DFT-D3 calculation there is no O_2 molecule formed. The four associated holes are localised on four oxygen ions from 6-fold coordinated Ti polyhedra. The oxygen ions are all 2-fold coordinated, 3 are Ti-Zr long bridges and the other is bridging two 6-fold coordinated Ti ions. These oxygen ions are over 5 Å away from the vacancy site. The vacancy does not lead to the large displacement of the 5-fold coordinated Ti ions, as in the DFT calculation. There is however, a displacement of 0.25 Å towards the vacancy by a 6-fold coordinated Ti ion in the row of 6-fold coordinated Ti ions under the vacancy site.

The charged Zr vacancies do not result in the formation of an oxygen molecule. The 6-fold coordinated polyhedron below the vacancy has become 5-fold coordinated, with the oxygen ion moving towards the vacancy site for the singly charged vacancy in the DFT calculation. The distance between the Ti and O ion has increased from 1.89 Å in the bulk to 2.65 Å in the defective structure. DFT-D3 shows that the three holes are localised on three Ti-Zr long bridges. Again these oxygen ions are over 5 Å from the vacancy site.

For DFT the doubly charged vacancy delocalises the two holes on four oxygen ions surrounding the vacancy. These four oxygen ions are all 2-fold coordinated in the defect structure, bridging a 6-fold coordinated Ti and a Zr ion. On the other hand DFT-D3 delocalises the two holes over three oxygen ions. These oxygen ions are all Zr-Ti bridges, two long and one short bridge. The localisation of the hole onto the short Ti-Zr bridge causes the Ti-O bond to break. The Ti ion is displaced 0.24 Å, similar to the neutral vacancy but the oxygen ion is not displaced with it. The Ti-O distances has increased from 1.97 Å in the bulk to 2.27 Å in the defect structure, an increase of 15%.

The triply charged defect delocalises the hole over two 2-fold coordinated oxygen ions, which bridge a Ti and Zr in both DFT and DFT-D3 calculations. The localised holes are on oxygen ions which are the same side

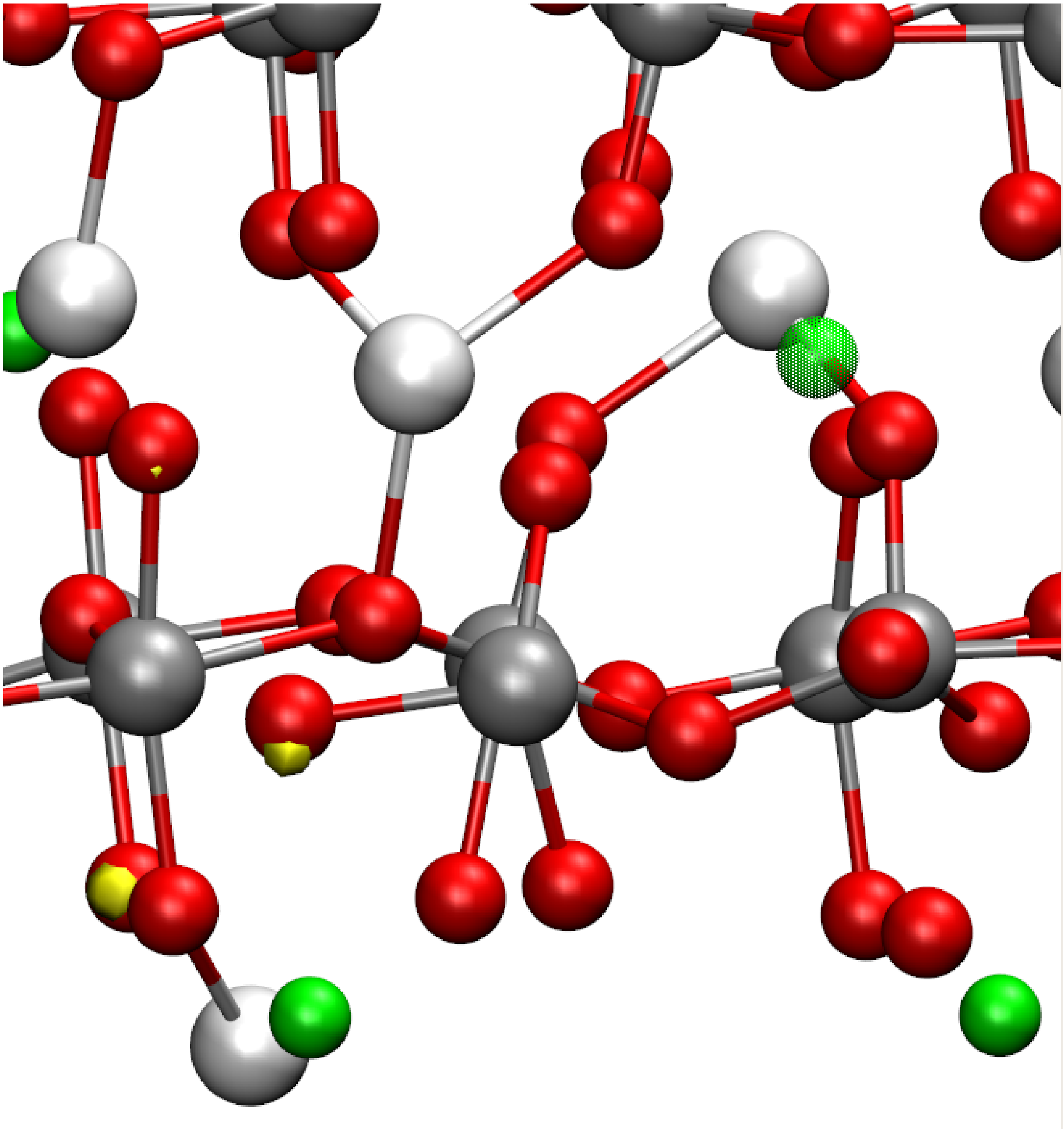

Figure 6.11: Charge density of the Ca$^-$ vacancy at 0.15 e Å^{-3}, showing the delocalisation of the hole over two oxygen ions. The dotted green sphere shows the vacant Ca position.

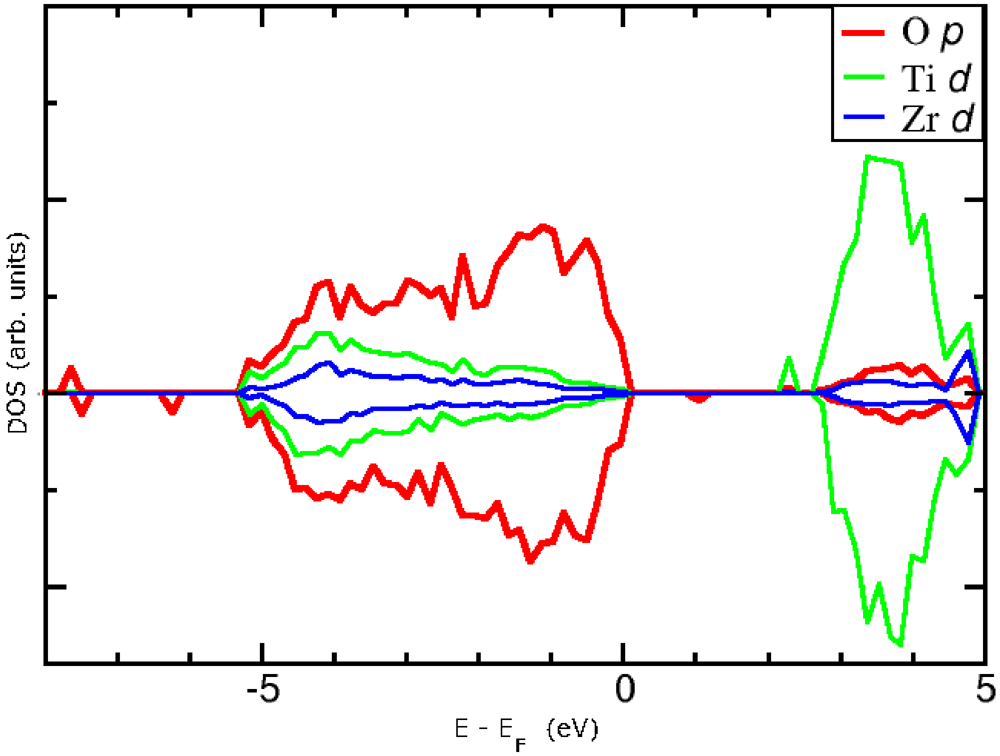

Figure 6.12: Partial DOS of the neutral Zr vacancy. [3] Copyright 2011 by the American Physical Society.

Table 6.3: Summary of the effects of charge localisation on the defect structure of the Zr vacancy. [3]

Charge state	Defective structure
$V^0{}_{Zr}$	O_2, 6 x 5-fold coordinated Ti, 1 x 6-fold coordinated Ti
$V^-{}_{Zr}$	5 x 5-fold coordinated Ti, 2 x 6-fold coordinated Ti
$V^{2-}{}_{Zr}$	5 x 5-fold coordinated Ti, 1 x 6-fold coordinated Ti
$V^{3-}{}_{Zr}$	6 x 5-fold coordinated Ti
$V^{4-}{}_{Zr}$	5 x 5-fold coordinated Ti

of the vacancy and are separated by the vacancy row for DFT. DFT-D3 also has the localised holes separated by the vacancy row but on different sides of the vacancy. The quadruply charged vacancy has no holes associated with this vacancy and thus a delocalised state is prevented. In the DFT-D3 calculation the breaking of the Ti-O bond occurred as it did for the doubly charged vacancy, with the separation of 2.27 Å between the ions. In the DFT results the 4-fold coordinated polyhedron is displaced from the Ti row in these charged vacancies by 0.69 Å, 0.68 Å, 0.69 Å and 0.85 Å for the singly, doubly, triply and quadruply charged vacancy, respectively. This displacement does not occur in the DFT-D3 calculations. There are no defect levels present in the band gap for any of these charged vacancies.

The defect structures observed in DFT have a strong dependence on charge state while the DFT-D3 shows no dependence on the charge state, apart from the Ti-O bond length in two charge states. These differences in the defect structures of the Zr vacancies are due to the different simulation cell used. The neutral Zr vacancy in the unit cell was calculated using DFT and no O_2 molecule was formed, similar to the DFT-D3 result. This shows that the defect structures are dependent on system size and therefore, defect concentration.

There are three different chemical environments for the titanium ions and the relaxed vacancy structure is strongly dependent on the environment, as table 6.4 shows for the DFT results. In the first environment the neutral and singly charged vacancies result in the formation of an oxygen molecule within the vacancy site, similar to that of the neutral zirconium vacancy, with bond lengths of 1.25 Å and 1.24 Å, respectively. The phonon frequencies of these molecules are 37.05 THz and 37.59 THz (1236 cm^{-1} and 1254 cm^{-1}) for the neutral and singly charged vacancies, respectively. The iso-surface of the neutral vacancy is shown in figure 6.13 at -0.01 eV Å^{-3} and shows electron density in the middle of the two oxygen atoms. This build up of electron density indicates that a covalent bond has formed. The molecule formed by the singly charged vacancy has a similar electron density to that of the neutral vacancy O_2 molecule. The higher charged vacancies do not result in the formation of an oxygen molecule, however, the triply and quadruply charged vacancies lead to the formation of a 5-fold coordinated Ti polyhedron at the expense of the 4-fold coordinated polyhedron next to the vacancy.

DFT-D3 shows little charge dependence, similar to the Zr vacancies, with no oxygen molecule formed for the neutral vacancy. The four holes are delocalised over five oxygen ions; two long Ti-Zr bridges, one short Ti-Zr bridge, a 3-fold coordinated O and a two 6-fold coordinated Ti bridge. The presence of the vacancies cause the displacement of the two axial oxygens of the vacant Ti polyhedron by 0.23 Å and 0.38 Å away from the vacancy site (figure 6.14). The singly charged vacancy does not cause the formation of an oxygen molecule either, the three holes are localised on oxygen ions over 6 Å away from the vacancy site on Ti-Zr bridges. The two axial oxygens from the vacancy polyhedron are displaced by the same amount as the neutral vacancy. The defect structure is similar for the doubly charged vacancy, with the holes both localised on two 6-fold coordinated Ti bridges. The axial oxygens are displaced by 0.31 Å and 0.37 Å in this defect structure. The triply charged vacancy causes the displacement of the axial oxygens by 0.23 Å and 0.37 Å. The hole is delocalised over two oxygen ions, a long Ti-Zr bridge and a 3-fold coordinated O, while the quadruply charged vacancy displace the axial oxygens by 0.29 Å and 0.38 Å.

In the DFT results the vacancy in the second Ti environment causes the formation of a 6-fold coordinated Ti polyhedron from the 4-fold coordinated polyhedron next to the vacancy site in all the charge states. The quadruply charged vacancy gives rise to defect levels in the band gap formed from oxygen *p* orbitals at 0.15 eV and 0.28 eV above the valence band (figure 6.15).

The presence of the vacancy causes the displacement of the oxygen ions of the vacant polyhedron, with a larger displacement of an axial oxygen from the vacancy polyhedron by 0.24, 0.21, 0.17, 0.15 and 0.20 Å in the neutrally, singly, doubly, triply and quadruply charged DFT-D3 results, respectively. The singly and quadruply charged vacancy also results in the other axial oxygen being displaced 0.24 and 0.26 Å, respectively.

The 4-fold coordinated vacancy results in the formation of a 5-fold coordinated Ti polyhedron from the other 4-fold coordinated Ti polyhedron in the Ti row for all vacancy charge states. An additional 5-fold coordinated Ti polyhedron is formed in the Ti row below the vacancy in the neutral and doubly charged state. The presence of the doubly charged or lower charged vacancies forms an oxygen dumb-bell in the adjacent Ti row by two bridging oxygen ions at the expense of a 6-fold coordinated polyhedron. The presence of the 4-fold coordinated Ti vacancy results in the formation of three 5-fold coordinated Ti polyhedra when the vacancy is neutral or doubly charged.

The 5-fold coordinated Ti vacancy caused the formation of a 5-fold coordinated Ti polyhedron at the expense of a 6-fold coordinated Ti in the neutral vacancy. Also the vacancy displaces an axial oxygen 0.28 Å away from the vacancy site. The singly charged vacancy does not lead to the creation of the 5-fold coordinated Ti but causes the axial oxygen to be displace 0.29 Å. The doubly and quadruply charged vacancy causes a equatorial oxygen being displaced 0.63 and 0.51 Å towards the 6-fold coordinated row, respectively. The triply charged vacancy caused the displacement of four the surrounding oxygen ions by a minimum of 0.26 Å.

The difference in the charge state dependence on defect structure observed for the Ti vacancies in these two methods is due to the system size dependence seen in the Zr vacancies.

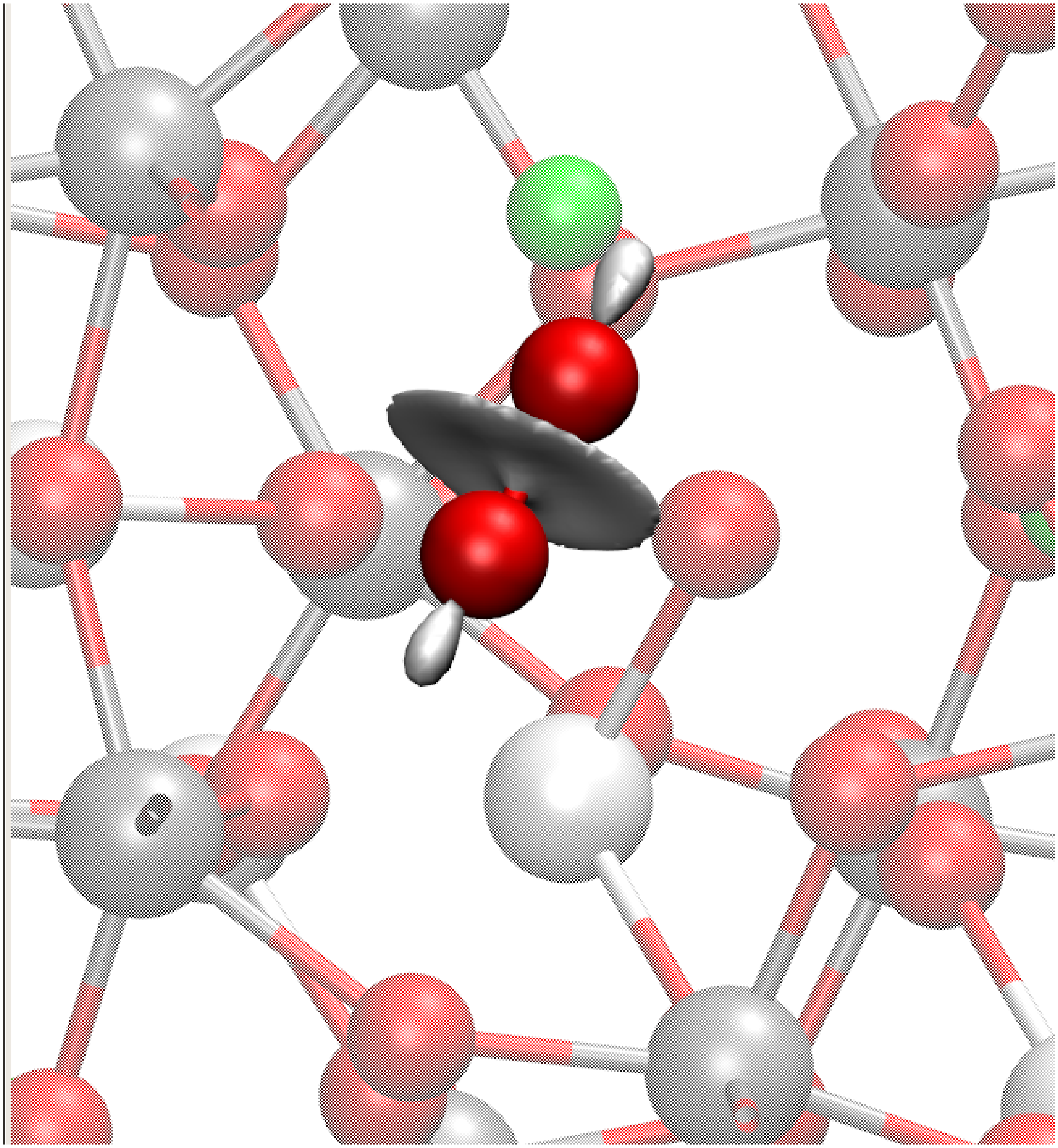

Figure 6.13: Iso-surface (-0.01 e $Å^{-3}$) of the 6-fold coordinated Ti neutral vacancy showing electron density between the oxygen atoms viewed along the <001> direction. [3] Copyright 2011 by the American Physical Society.

Table 6.4: Summary of the effects of charge localisation and chemical environment on the defect structure of the Ti vacancies. [3]

Charge state	1^{st} environment	2^{nd} environment	3^{rd} environment
$V^{0}{}_{Ti}$	O_2	6-fold coordinated Ti	3 x 5-fold coordinated Ti
$V^{-}{}_{Ti}$	O_2	6-fold coordinated Ti	2 x 5-fold coordinated Ti
$V^{2-}{}_{Ti}$		6-fold coordinated Ti	3 x 5-fold coordinated Ti
$V^{3-}{}_{Ti}$	5-fold coordinated Ti	6-fold coordinated Ti	5-fold coordinated Ti
$V^{4-}{}_{Ti}$	5-fold coordinated Ti	6-fold coordinated Ti	5-fold coordinated Ti

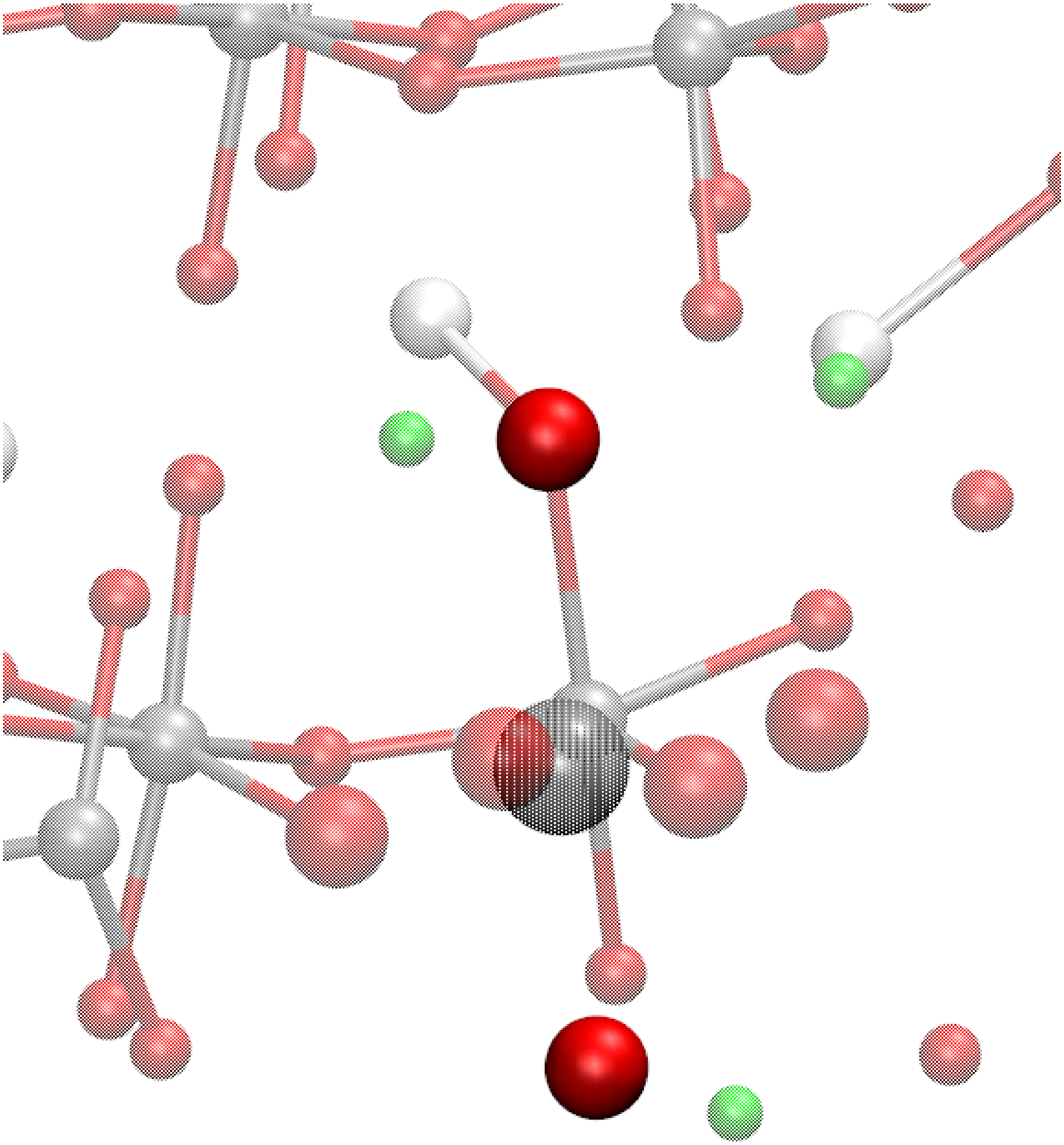

Figure 6.14: Displaced axial oxygen ions from the vacancy polyhedra. Dotted silver sphere shows Ti vacancy.

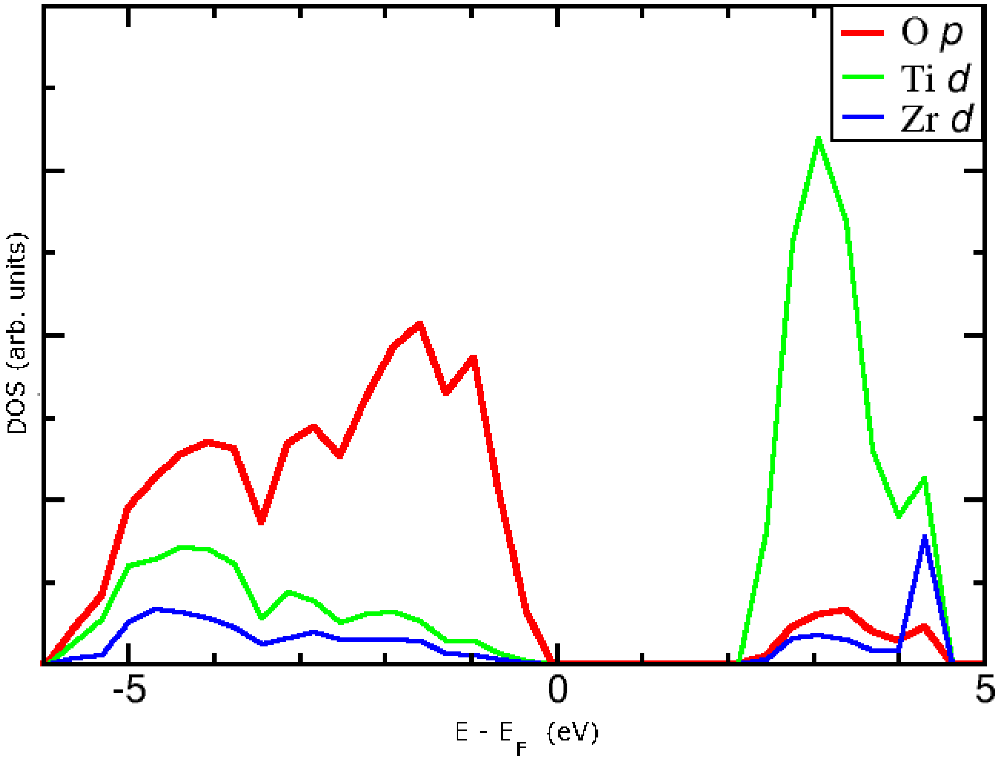

Figure 6.15: Partial DOS of the quadruply charged Ti vacancy in the second environment. [3] Copyright 2011 by the American Physical Society.

It is rare that DFT is able to describe hole localisation in oxide materials.[157] However it has been observed to localise correctly hole states at low coordination sites on the MgO surface.[158] Analysis of the oxygen coordination in zirconolite shows that the oxygen ions are either 2- or 3-fold coordinated, thus providing sites for holes to localise. The calcium and first Ti vacancies localise holes on 2-fold coordinated oxygen ions, while the second Ti vacancy localise the holes on only 3-fold coordinated oxygen ions. The Zr and the 4-fold coordinated Ti vacancy localises the holes on both 2- and 3-fold coordinated oxygen ions.

6.3.2.1 Vacancy defect formation energies

The formation energy of the vacancy defects has been calculated to determine the stable charge state of the vacancy and the results are summarised in Table 6.5. The formation energy is calculated using equation (6.1) and is with respect to the chemical potential of the element and the electrons.

$$E_f(\mu_X, E_F) = (E_v - q\Delta V) - E_B + \mu_X + qE_{VBM} + qE_F \tag{6.1}$$

here, E_f is the formation energy, E_v is the energy of the cell containing the vacancy, $q\Delta V$ is the potential alignment correction,[57] E_B is the energy of the cell without the defect, μ_X is the chemical potential of the isolated element in a vacuum ($\mu_X = E_X$, with the oxygen atom in a triplet state), E_{VBM} is the energy of the valence band maximum and E_F is the Fermi level which acts as an electron reservoir and is set to the valence band maximum in these calculations.

As table 6.5 shows the different defect structures calculated using the two methods have an effect on the defect formation energies obtained. The higher lattice energy predicted by DFT-D3, compared to the value from DFT simulations, results in a constant shift in the vacancy formation energies of around 3 eV. The lower lattice energy in the previous calculation was due to the local minimum located during the cell optimisation, with a

Table 6.5: A comparison between the defect formation energies calculated using DFT and DFT-D3. The formation energies are with respect to the chemical potential of the isolated atom in vacuum and the electron chemical potential set to the valence band maximum. The numbers in bold show the most stable charge state for each vacancy. Charges are positive for anion vacancies and negative for cation vacancies.

Vacancy		Neutral (eV)		Singly charged (eV)		Doubly charged (eV)		Triply charged (eV)		Quadruply charged (eV)	
		With correction	Without correction	With correction	Without correction	With correction	Without correction	With correction	Without correction	With correction	Without correction
O bridging two 6-fold coordinated Ti	DFT	3.75	3.75	1.10	-2.11	**-1.32**	**-7.76**				
	DFT-D3	7.64	7.64	4.32	-2.41	**1.60**	**-11.85**				
O short Ti Zr bridge	DFT	5.78	5.78	2.99	-0.23	**0.49**	**-5.95**				
	DFT-D3	8.82	8.82	5.88	-0.85	**3.07**	**-10.38**				
O long Ti Zr bridge	DFT	5.04	5.04	2.58	-0.64	**-0.20**	**-6.64**				
	DFT-D3	7.58	7.58	4.64	-2.08	**1.67**	**-11.78**				
3-fold coordinated bridging O	DFT	5.43	5.43	1.43	-1.79	**-1.19**	**-7.62**				
	DFT-D3	8.56	8.56	5.72	-1.01	**1.72**	**-11.73**				
Ca	DFT	8.16	**8.16**	**7.84**	11.06	7.90	14.34				
	DFT-D3	11.04	**11.04**	10.97	17.70	**10.89**	24.34				
Zr	DFT	20.40	**20.40**	20.94	24.16	19.35	25.79	19.70	28.83	**19.05**	31.93
	DFT-D3	23.13	**23.13**	22.94	29.66	22.62	36.07	22.47	42.64	**22.37**	49.27
1st 6-fold coordinated Ti	DFT	17.89	**17.89**	18.02	21.24	17.54	23.98	**17.32**	26.98	17.66	30.54
	DFT-D3	20.37	**20.37**	20.15	26.88	**19.96**	33.41	20.18	40.36	20.37	47.27
2nd 6-fold coordinated Ti	DFT	17.36	**17.36**	16.69	19.91	**16.33**	22.77	16.60	26.26	16.91	29.78
	DFT-D3	20.40	**20.40**	**20.30**	27.02	20.56	34.01	20.83	41.01	20.73	47.63
4/5-fold coordinated Ti	DFT	18.58	**18.58**	18.37	21.59	18.46	24.90	**16.35**	26.01	16.48	29.36
	DFT-D3	19.85	**19.85**	19.43	26.15	19.28	32.73	**19.28**	39.45	19.41	46.30

Table 6.6: Frenkel pair energies of the species within zirconolite. * denotes the energy of the Zr interstitial located in <010> channel used to calculate the Frenkel pair energy.

Frenkel pair	Defect energy (eV)	
	With correction	Without correction
O^{0} + two 6-fold coordinated Ti bridging $V^{0}{}_{O}$	1.15	1.15
O^{-} + two 6-fold coordinated Ti bridging $V^{+}{}_{O}$	-1.60	-1.68
O^{0} + Ti Zr short bridging $V^{0}{}_{O}$	3.18	3.18
O^{-} + Ti Zr short bridging $V^{+}{}_{O}$	0.28	0.19
O^{0} + Ti Zr long bridging $V^{0}{}_{O}$	2.44	2.44
O^{-} + Ti Zr long bridging $V^{+}{}_{O}$	-0.13	-0.21
O^{0} + 3-fold coordinated bridging $V^{0}{}_{O}$	2.83	2.83
O^{-} + 3-fold coordinated bridging $V^{+}{}_{O}$	-1.28	-1.36
Ca^{2+} + $V^{2-}{}_{Ca}$	1.97	2.31
Zr^{2+}* + $V^{2-}{}_{Zr}$	8.22	7.01
Ti^{2} + 1st 6-fold coordinated $V^{2-}{}_{Ti}$	5.11	5.37
Ti^{2+} + 2nd 6-fold coordinated $V^{2-}{}_{Ti}$	3.98	4.12
Ti^{2+} + 4-fold coordinated $V^{2-}{}_{Ti}$	6.03	6.29

difference in lattice energy of 7.27 eV per unit cell between the structures. The bulk structure obtained from the DFT-D3 calculations was used to calculate the neutral oxygen vacancy in VASP, using the same set-up used in the other DFT calculations. The oxygen vacancy formation energy was 7.33 eV, in agreement with the DFT-D3 values.

Table 6.5 shows that, for this position of the E_F, the neutral defects are the least stable for all species, apart from the Zr vacancy which is 0.5 eV more stable than the singly charged defect. The chemical environment of the 6-fold coordinated Ti has an effect on the stable vacancy charge state with the Ti in the 6-fold coordinated row favouring the triple charged state, while Ti in the alternating row favours the doubly charged state. The value of E_f for the oxygen vacancies are in good agreement with that for the formation of oxygen vacancies in ZrO_2.[159]

6.3.3 Frenkel defects

The energies of the isolated interstitials and vacancies were used to calculate the Frenkel pair energies, equation (6.2), for each species present in zirconolite using DFT. The Frenkel pair energies are summarised in table 6.6.

$$E_{FP} = (E_v - q_v \Delta V) + (E_i - q_i \Delta V) - 2E_p \tag{6.2}$$

where E_{FP} is the Frenkel defect energy, E_v is the energy of the cell containing the vacancy, E_i is the energy of the cell containing the interstitial, $q\Delta V$ is the potential alignment correction[57] and E_p is the energy of the bulk cell.

Table 6.6 shows that the Frenkel defect energies are relatively low and that they are consistent with other complex materials, with the oxygen Frenkel pair energies ranging from 2.8-5.3 eV in pyrochlores[160] and a Zr Frenkel pair energy of 11.16 eV in zircon.[41] The low value for the Ca Frenkel pair supports results from Chappell et al., who found that there was a significantly larger fraction of Ca defects when the damage was normalised to the amount of each ion in the formula unit, 2106 Ca defects compared to 542 O defects.[115] It was also observed that there was no recovery for the Ca ion in the early stages of the cascade, unlike that seen for the other species. The high number of defects created and the lack of healing by the Ca seen by Chappell *et al.* shows that the Ca defects are relatively stable compared to the lattice and this is what the Frenkel pair energy calculated here shows. The low Frenkel pair formation energy of the defects in zirconolite is the reason for the low self-healing of the lattice, as the defects are relatively stable compared to the lattice. The neutral oxygen Frenkel pair defect energy in MgO, which undergoes significant self-healing of the lattice to leave only point defects, has an defect energy of 10.28 eV compared to 1-3 eV in zirconolite, supporting the conclusion that the low energy of the Frenkel pairs prevents self-healing from occurring in the zirconolite lattice.

The negative values for the singly charged oxygen Frenkel pairs are unphysical and are caused by the local minimum from which the DFT structure is located. This was shown by using DFT to calculate the Frenkel pair defect energy with the bulk structure used in the DFT-D3 simulations. The Frenkel defect for the singly charged two 6-fold coordinated Ti bridge oxygen pair has a defect formation energy of 3.92 eV, proving that the local minimum is the cause of the unphysical result. However, in the experimental synthesis of the monoclinic structure, the addition of excess TiO_2 and ZrO_2 is required to form the monoclinic phase. It can therefore be implied that the monoclinic crystal structure is not the most stable phase of zirconolite. This could result in the creation of defects allow the reorientation of the structure towards a lower energy structure.

6.4 Conclusions

DFT has been used to study intrinsic defects in zirconolite, a complex ceramic that is a promising candidate for encapsulating high-level radioactive waste. The complex crystal structure and the range of possible defect oxidation states means that this material is challenging to study using both experimental and modelling techniques.

We have used an efficient random search technique to identify the lowest energy conformation for interstitials in the zirconolite unit cell. This method enabled the identification of stable defect structures that would have been difficult to predict by traditional methods. The neutral O interstitial resulted in the removal of the 4-fold coordinated Ti polyhedra, whereas the O^- interstitial increased the coordination of a Ti ion from 4 to 5. The Ca and Ti interstitials favour sites in the <010> channels between the ions, whereas the Zr interstitial displaced a Ti ion from its lattice site to form a substitutional Zr ion and a Ti interstitial.

Vacancies in zirconolite were also shown to have interesting structures, which were sometimes strongly dependent on the oxidation state and size of the simulation cell. In particular, the neutral Zr vacancy resulted in the formation of an O_2 molecule, whereas the singly charged vacancy did not result in molecule formation, but it did cause significant displacement of one oxygen atom on a neighbouring 6-fold coordinated Ti ion in the larger cell. Oxygen molecules were also observed to form near some Ti vacancies, those associated with the 6-fold coordinated Ti ion, but not in others.

The chemical environment of the O vacancies was found to have a strong effect on the formation energies of oxygen Frenkel pairs, which range between 1.15 eV and 3.18 eV for different chemical environments. The low Frenkel pair formation energies could explain why zirconolite requires a small number of displacements per atom (dpa) to become amorphous[11] as the defects are relatively stable.

Chapter 7

He in zirconolite

7.1 Introduction

The formation of He inside the waste form is caused by the α particle, emitted from a decaying encapsulated actinide element, localising two electrons. Therefore, every α decay event will lead to the production of a He atom. The proposed plutonium loading of a zirconolite waste form is 10 wt%[23] and this is equivalent to one Pu ion per zirconolite unit cell. Nuclear waste generates Pu in a number of different isotopes, which have different half lives and decay paths, therefore the production of He will occur at different rates over time as each Pu isotope decays. However, Pu^{239} decay sequence involves eight α decays and therefore, eight He atoms will eventually be produced over 10^8 years.

$Pu^{239} \xrightarrow{\alpha} U^{235} \xrightarrow{\alpha} Th^{231} \xrightarrow{\beta} Pa^{231} \xrightarrow{\alpha} Ac^{227} \xrightarrow{\beta} Th^{227} \xrightarrow{\alpha} Ra^{233} \xrightarrow{\alpha} Rn^{219} \xrightarrow{\alpha} Po^{215} \xrightarrow{\alpha} Pb^{211} \xrightarrow{\beta}$
$Bi^{211} \xrightarrow{\alpha} Tl^{207} \xrightarrow{\beta} Pb^{207}$

The produced He atoms will be confined within the waste form, either in the bulk, localised at grain boundaries or in the form of He bubbles. The accumulation of He will have an effect on the performance of the waste form, as the strain caused by the He bubbles can lead to cracking of the waste form. The He atoms tend to cluster into bubbles to maximise the van der Waals interactions. As the bubbles grow in size the lattice must distort to accommodate the bubble. These distortions lead to the creation of the strain which eventually leads to the cracking of the waste form. The HIPing method of synthesising the zirconolite waste form leads to a polycrystalline material, which contains a large number of grain boundaries in which He could aggregate and form bubbles, resulting in large stress fields through the waste form.

The closed shell configuration of the He atom means that He will only interact through van der Waals interactions. The small electron density around the He atom means that no permanent-induced dipoles will be created, unlike the larger noble gas atoms, such as Xe.[161] Therefore, instantaneous-induced dipoles (London dispersion) will dominate the behaviour of the He atom. Standard DFT is unable to describe the instantaneous fluctuations in the charge distribution as two atoms get closer. This has the effect of overbinding noble gas atoms.[162]

In order to model He interactions in zirconolite accurately DFT with the dispersion correction (DFT-D) is needed. The DFT-D method implemented in the VASP code adds the energy from classical potentials to the total energy calculated at each self consistent cycle.[162] However, as DFT over estimates the bonding for the noble gases, the addition of another energy term has no effect on the results for the noble gases. Grimme *et al.* have developed a more sophisticated method for calculating the dispersion forces in DFT-D.[62] The long range interactions of the DFT potentials have been removed, leaving the potential only acting on or near the atom. The long range interactions have been modelled through interatomic potentials and the total energy is the sum of the short range and long range energies (DFT-D3). This implementation of DFT-D is available in the CP2K code. CP2K is a periodic DFT code that uses Gaussian basis sets, as well as plane waves, to efficiently treat the electrostatic interactions, which leads to a linear scaling computational cost with system size. The Gaussian Plane Wave (GPW) representation of the Kohn-Sham energy is:

$$E[n] = E_T[n] + E_V[n] + E_{Hartree}[n] + E_{XC}[n] + E_{II}$$

$$\begin{aligned} &= \sum_{\mu\nu} P^{\mu\nu} \left\langle \varphi_\mu(\mathbf{r}) \mid -\frac{1}{2}\nabla^2 \mid \varphi_\nu(\mathbf{r}) \right\rangle + \sum_{\mu\nu} P^{\mu\nu} \left\langle \varphi_\mu(\mathbf{r}) \mid V^{PP}_{loc}(\mathbf{r}) \mid \varphi_\nu(\mathbf{r}) \right\rangle \\ &+ \sum_{\mu\nu} P^{\mu\nu} \left\langle \varphi_\mu(\mathbf{r}) \mid V^{PP}_{nl}(\mathbf{r},\mathbf{r}') \mid \varphi_\nu(\mathbf{r}) \right\rangle + 2\pi\Omega \sum_{\mathbf{G}} \frac{\tilde{n}*(\mathbf{G})\,\tilde{n}(\mathbf{G})}{\mathbf{G}^2} \\ &+ \int e^{XC}(\mathbf{r})\,\mathrm{d}\mathbf{r} + \frac{1}{2}\sum_{I\neq J} \frac{Z_I Z_J}{\left|\mathbf{R}_I - \mathbf{R}_j\right|} \end{aligned} \tag{7.1}$$

here E_{II} is interaction energies of the ionic cores with charge Z_A and position $\mathbf{R}_A$, $P^{\mu\nu}$ is the density matrix, $\varphi_\mu(\mathbf{r}) = \sum_i d_{i\mu} g_i(\mathbf{r})$ with $g_i(\mathbf{r})$ as a primitive Gaussian function and corresponding contraction coefficient $d_{i\mu}$, Ω is the volume of the unit cell, $\boldsymbol{G}$ is the reciprocal lattice vectors and $\tilde{n}(\mathbf{G})$ is such that $\tilde{n}(\mathbf{r})$ is equal to $n(\mathbf{r})$ on a regular grid in the unit cell.

DFT-D3 was used to locate the position of the He interstitial site using AIRSS. The incorporation energy of He was calculated and compared to other nuclear ceramic materials. The migration barrier of the He interstitial was calculated using the nudged elastic band method and compared to the limited experimental results. The binding energy of the He atom to the vacancies was calculated, via a trapping energy, to see if there was a tendency for He to localise in the lattice vacancies, where they can act as nucleation sites for bubble formation. AIRSS was used to study if bubbles could form in the bulk of zirconolite, by inserting multiple He atoms at once in the searches.

7.2 Computation method

Zirconolite 2M is comprised of layers of 6- and 5-fold coordinated Ti polyhedra separated by layers of alternating Zr and Ca ions, with a monoclinic crystal structure (figure 7.1).[2] The 88 ion unit cell was used in this work. The structure was relaxed using the periodic DFT CP2K code,[61] the revised PBE functional along with Grimme's D3 dispersion correction[62] and DZVP basis sets.[61] Structures were considered to be relaxed when the forces on all atoms were less than 0.025 eV Å^{-1}. The CP2K code uses Γ point sampling of the Brillouin zone. The relaxed cell vectors were in good agreement to those obtained by Rossell using x-ray diffraction (XRD) experiments (table 6.2).[2] The defects were then introduced into this simulation cell and all ions relaxed with the cell parameters fixed. The 10 wt% loading proposed for zirconolite[23] is equivalent to a Pu ion per 88 ion unit cell and this will eventually result in 8 He atoms per unit cell, after the decay of all Pu and daughter ions after 10^8 years. Thus the cell size used in this work allows the behaviour of the maximum He build up to be studied.

7.2.1 Interstitial He defects

The complicated crystal structure of zirconolite makes it difficult to predict the stable configurations of the He interstitial defects and therefore AIRSS was employed in this study to identify energy minima. He atoms were randomly placed within the simulation cell and the ionic positions were relaxed using CP2K. The process

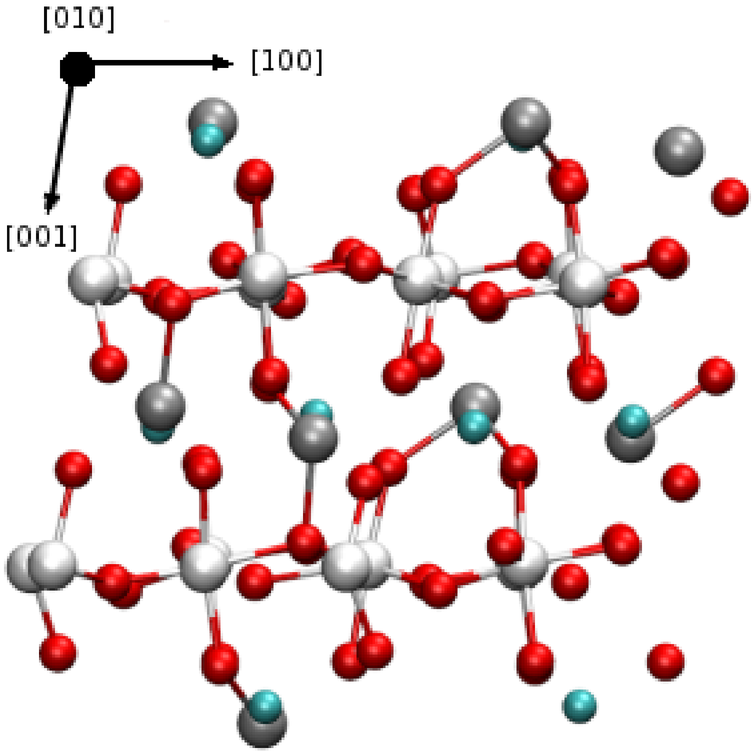

Figure 7.1: Structure of the unit cell of zirconolite projected in the [010] direction. The red spheres show oxygen ions, white spheres show titanium ions, silver spheres show zirconium ions and blue spheres show calcium ions.

was repeated until 20 different local minima were found. The interstitial site was identified as the lowest energy local minimum from the searches. A similar procedure was carried out for the multiple He interstitials, but in this case a number of He atoms were inserted simultaneously at random positions in the simulation cell using 100 searches.

The He migration pathway was calculated using the climbing image nudged elastic band (CI-NEB) methodology. The CI-NEB calculations were performed using 18 and 17 images for the <010> and <110> paths respectively, with a spring constant of 1.94 eV $Å^{-2}$.

7.2.2 Vacancy defect

The vacancy structures were taken from those obtained using DFT-D3 in Chapter 6.

7.2.3 He trapping

The trapping energy of a He atom by a vacancy is defined as the energy difference between the He in the vacancy and the vacancy and He interstitial separately. The trapped He energies were obtained by replacing the vacancy ghost ion by a He atom in the relaxed vacancy structure. A ghost basis-set of the vacant species was placed in the position of the He ghost in the vacancy calculation and the position of the ghost was fixed while the 88 atomic positions were relaxed.

$$E_{trap} = E_{He-B} + E_v - E_{He-v} - E_B \tag{7.2}$$

here E_{trap} is the energy of locating a He atom inside a vacancy, E_{He-B} is the energy of the cell containing the He atom located at the interstitial site within the bulk, E_v is the energy of the vacancy, E_{He-v} is the energy of

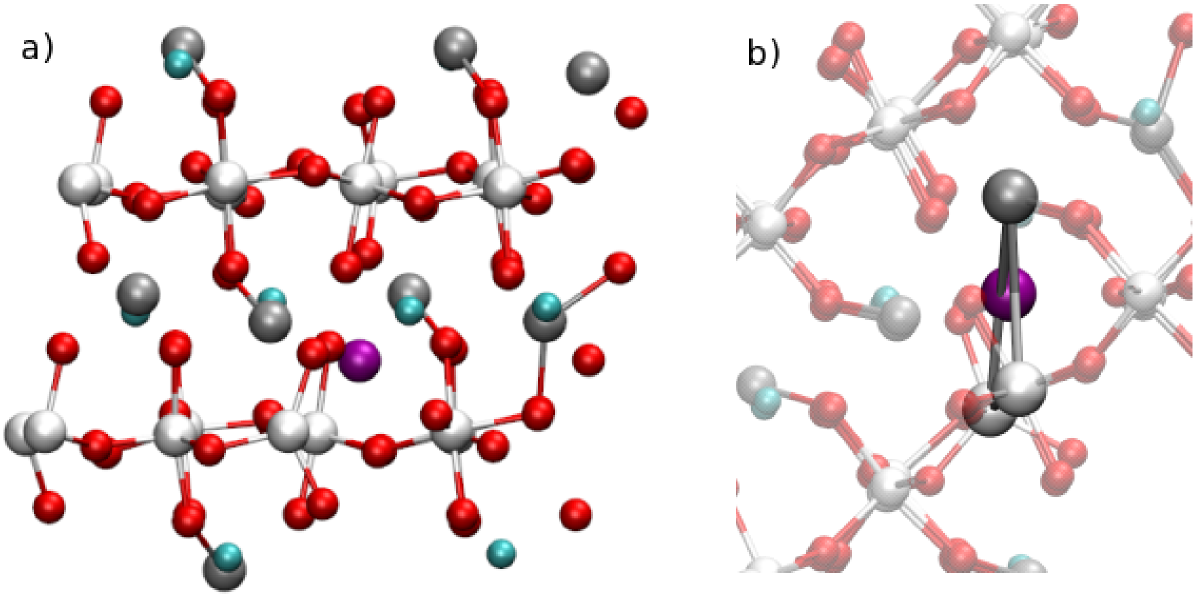

Figure 7.2: a) The lowest energy configuration for the He interstitial. b) Showing the He resides in the plane between the three ions. The purple sphere shows the helium atom.

the cell with the He placed inside the vacancy and E_B is the energy of bulk zirconolite with the He ghost basis set.

7.3 Results and discussion

7.3.1 Interstitial He defects

The lowest energy configuration for the He atom interstitial was located in <010> channels of the zirconolite lattice. The interstitial site is located in the plane between a 6-fold coordinated Ti (2.76 Å), a 5-fold coordinated Ti (2.74 Å) and a Zr ion (2.84 Å) (figure 7.2b). This position is the same interstitial site found using DFT and a hundred AIRSS searches. This is the reason why only twenty AIRSS searches were performed using DFT-D3. The interstitial He site is similar to that found in other ceramic materials studied, as the He interstitial site in zircon is in the channel parallel to the c axis, with a Zr-He distance of 2.55 Å.[41] In UO_2 the lowest energy configuration for the He atom is the octahedral interstitial site. In some metals (bcc Fe for example) the substitutional configuration, in which a He atom displaces a lattice ion and resides on the lattice site, causing the metal ion to become an interstitial, has been found to be the lowest energy configuration.[163] In other metals, such as bcc V metal, the favoured site for the He interstitial is the tetrahedral interstitial position.

The incorporation energy of He within zirconolite is calculated by eq (7.3), and gives a value of 1.08 eV. This is similar to values calculated for other ceramic materials, with $ZrSiO_4$ 1.45 eV,[41] $UO_{2\pm x}$ 1.34 eV[38] and ZrO_2 1.35 eV.[33]

$$E_{incorp=}E_{He-B}-(E_{He}+E_B) \tag{7.3}$$

here E_{incorp} is the energy required to incorporate a He atom into zirconolite, E_{He-B} is the energy of the cell containing the He atom located at the interstitial site within the bulk, E_{He} is the energy of the He atom in vacuum and E_B is the energy of bulk zirconolite with the He ghost basis set.

7.3.1.1 He diffusion

The location of the He interstitial suggests that there will be two easy directions for diffusion, the <010> and the <110> directions. The migration barriers were calculated by CI-NEB calculations for both pathways. Figure 7.3 shows the migration barriers predicted for the each pathway.

The CI-NEB predicts the <010> pathway is favoured over the <110>, with barriers of 1.46 eV and 1.70 eV, respectively. The calculated migration barrier is in reasonable agreement with the barrier of 1.05 eV obtained through thermal diffusion data.[138] Figure 7.3 shows the complicated migration barrier for He migration in both of the channels. The <010> barrier involves three potential barriers, while the <110> pathway involves four. The four barriers are caused by the He atom displacing Ca ions out of the Ca row as it migrates along the channel. The three barriers along the <010> path are caused by the He atom displacing 3, 2 and 1 oxygen ions, respectively, which form the channel, as it passes. The complexity of the potential energy surface means that lower energy pathways may be present but other computational methods (hyperdynamics[164] for example) would be required to locate these paths.

7.3.2 He trapping

The trapping of He by lattice defects is an important factor when determining the durability of a waste form because the trapped He could act as a nucleation site for the formation of bubbles within the lattice. The trapping energy is calculated by eq (7.2) and the results are summarised in table 7.1.

Table 7.1 shows that the favoured trap charge state for each species is the charge which gives the lowest electron density around the vacancy, which are the charged oxygen vacancies and the neutral cation vacancies. This favoured charge state trend is in agreement with the understanding of the substitution configuration in metals where the He atom favours low electron density sites, due to the closed shell electronic configuration. This is the cause of the substitution defect configuration in metals as in metallic systems the low electron density sites are on the vacant lattice sites.

The strongest trapping defect site in zirconolite is the neutral 5-fold coordinated Ti vacancy, followed by the Ca vacancies. The neutral 5-fold coordinated Ti vacancy site is thought to be favoured because the four holes associated with this defect reduce the charge on four of the five O ions surrounding the vacancy, which reduces the electron density around the vacancy (figure 7.4). The Ca vacancy is favoured because this site creates a large space within the lattice that easily accommodates the He atom. The trapping energy is independent of the charge state of the vacancy because of the size of the vacancy site.

The doubly charged 3-fold coordinated bridging O is the only vacancy inside which it is unfavourable to trap He, the reason being that the presence of the He atom inhibits the vacancy relaxation to its ground state configuration. The lowest energy configuration of the vacancy is a rearrangement of the remaining 5 coordinated O ions around a 6-fold coordinated Ti ion into a square pyramidal arrangement, with the bottom oxygen ion of the octahedron being displaced into the position of the removed oxygen, where the He should be placed (figure 7.5). In contrast to the other calculations, where the He atom was added to the relaxed structure of the vacancy, in this case the trapping energy was calculated by substituting the O atom with He in the bulk structure before relaxation.

The presence of the He atom in the singly charged short Ti-Zr bridge vacancy, caused a shift in the position of the defect level in the band gap by +0.44 eV, shown in figure 7.6. A shift of +0.77 eV was also observed in the position of the defect level for the singly charged 3-fold coordinated O vacancy, while in the neutral vacancy the defect level decreases in energy by 0.34 eV.

Similar shifts in the defect level position were also seen in the cation vacancy, with a small shift of +0.05 eV for the triply charged 2^{nd} 6-fold coordinated Ti vacancy. The formation of a doublet defect level occurred for the doubly charged vacancy, with peaks at 0.64 eV and 0.82 eV above the valence band maximum (VBM),

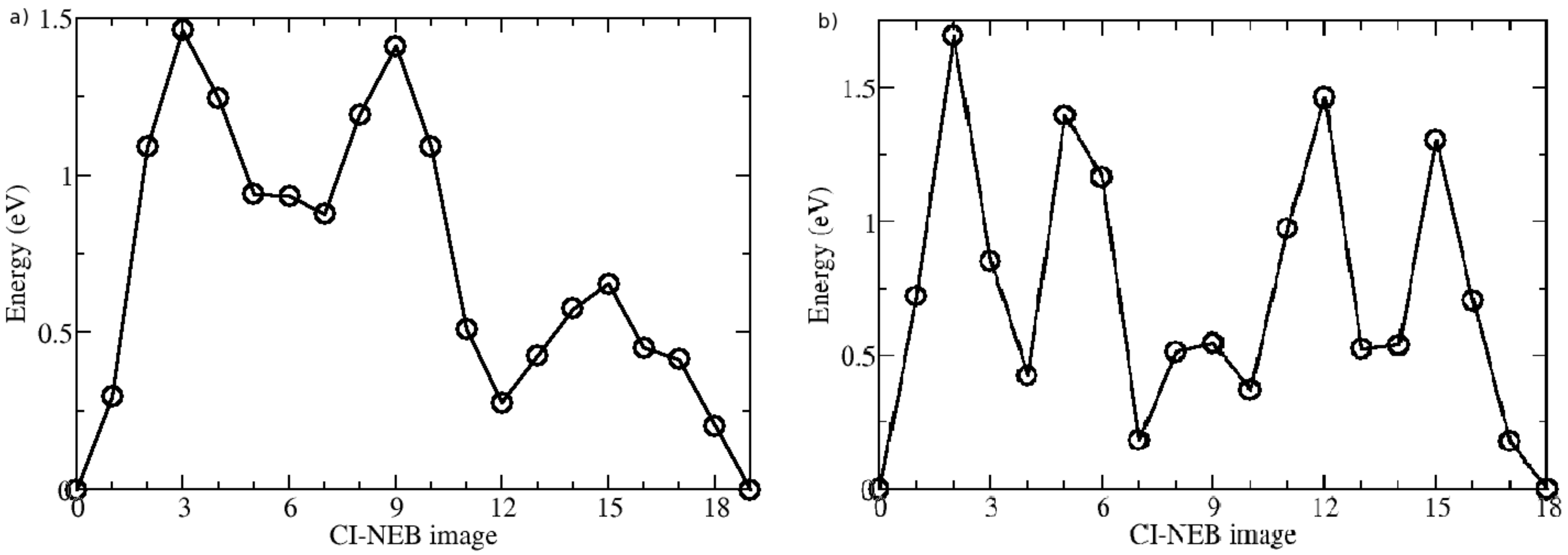

Figure 7.3: Migration barrier of the He atom through the a) <010> and b) <110> channels.

Table 7.1: Summary of the trapping energies of the vacancies in different charge states. The numbers in bold show the favoured charge state for trapping He for each vacancy.

Vacancy	Neutral (eV)	Singly charged (eV)	Doubly charged (eV)	Triply charged (eV)	Quadruply charged (eV)
O bridging two 6-fold coordinated Ti	0.65	0.59	**0.67**		
O short Ti Zr bridge	0.49	0.55	**0.69**		
O long Ti Zr bridge	0.50	0.56	**0.57**		
3-fold coordinated Ti	0.61	**0.76**	-0.19		
Ca	**0.97**	0.95	0.96		
Zr	0.78	**0.84**	0.68	0.64	0.61
1^{st} 6-fold coordinated Ti	**0.50**	0.25	0.22	0.25	0.43
2^{nd} 6-fold coordinated Ti	**0.46**	0.24	0.40	0.19	0.29
5-fold coordinated Ti	**1.11**	0.80	0.65	0.60	0.49

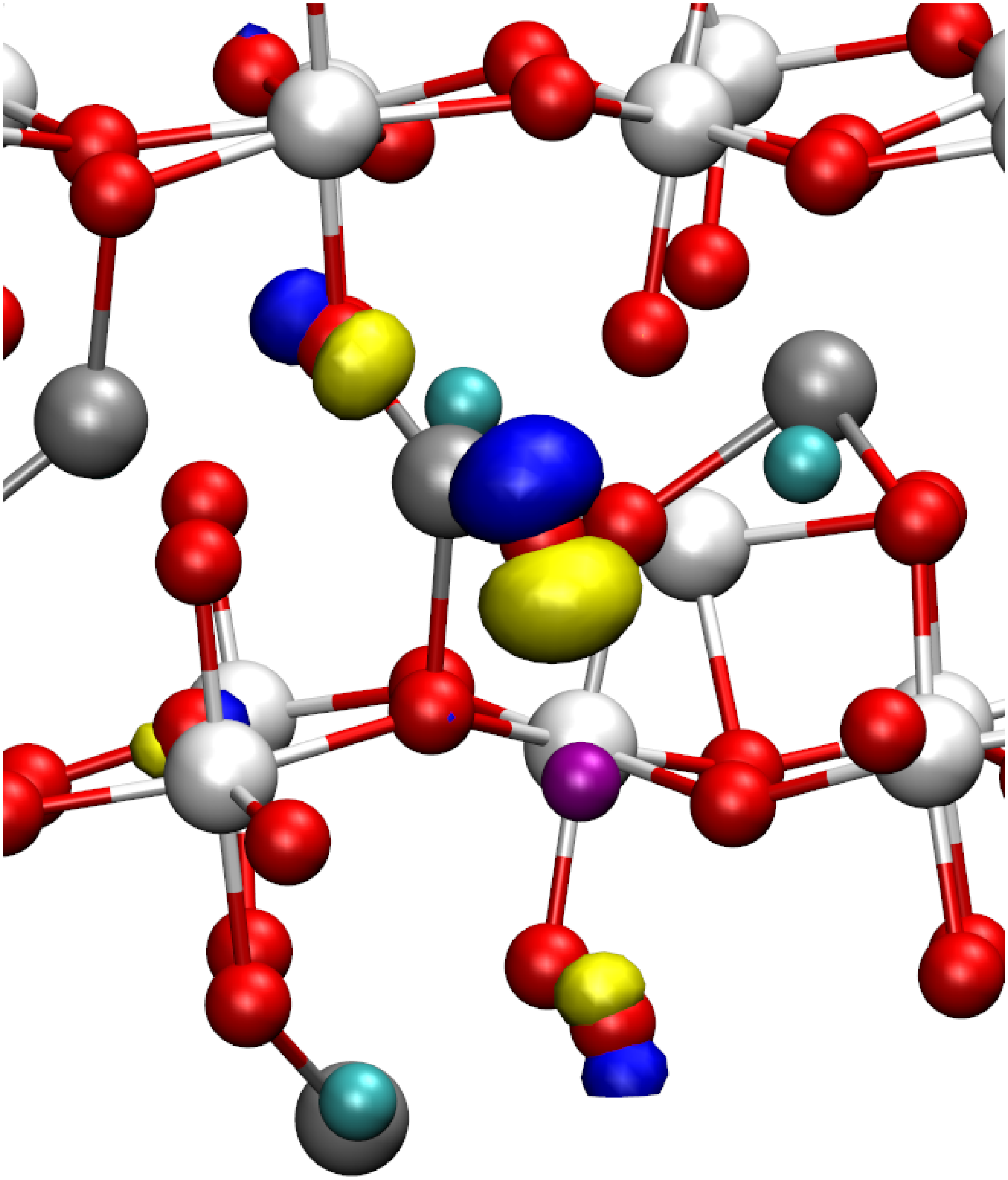

Figure 7.4: Charge density of the neutral 5-fold coordinated Ti vacancy with a He atom localised inside, shown at 0.08 e Å^{-3}.

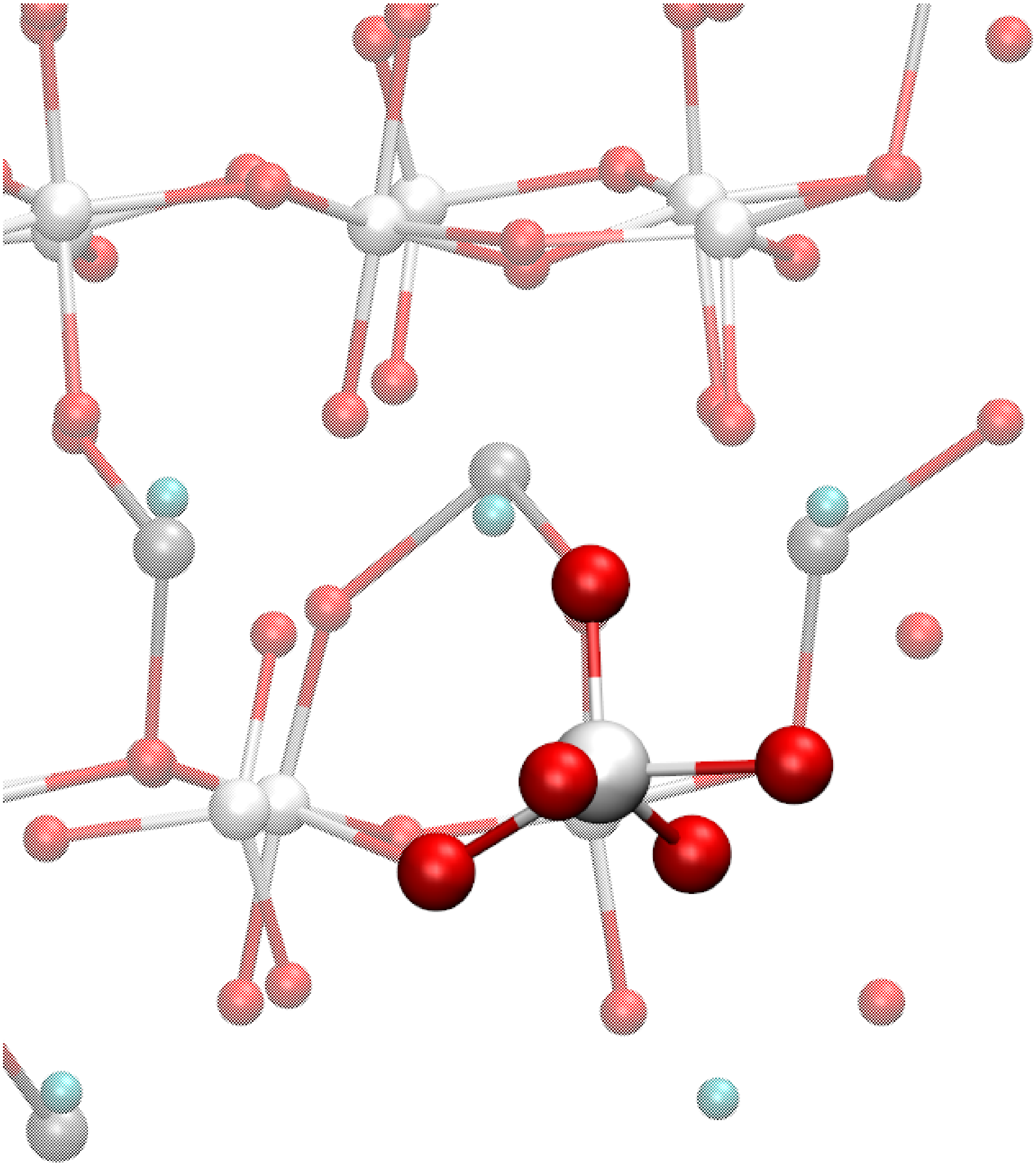

Figure 7.5: Relaxed configuration of the doubly charged 3-fold coordinated O vacancy, showing the square pyramidal rearrangement of the oxygen ions.

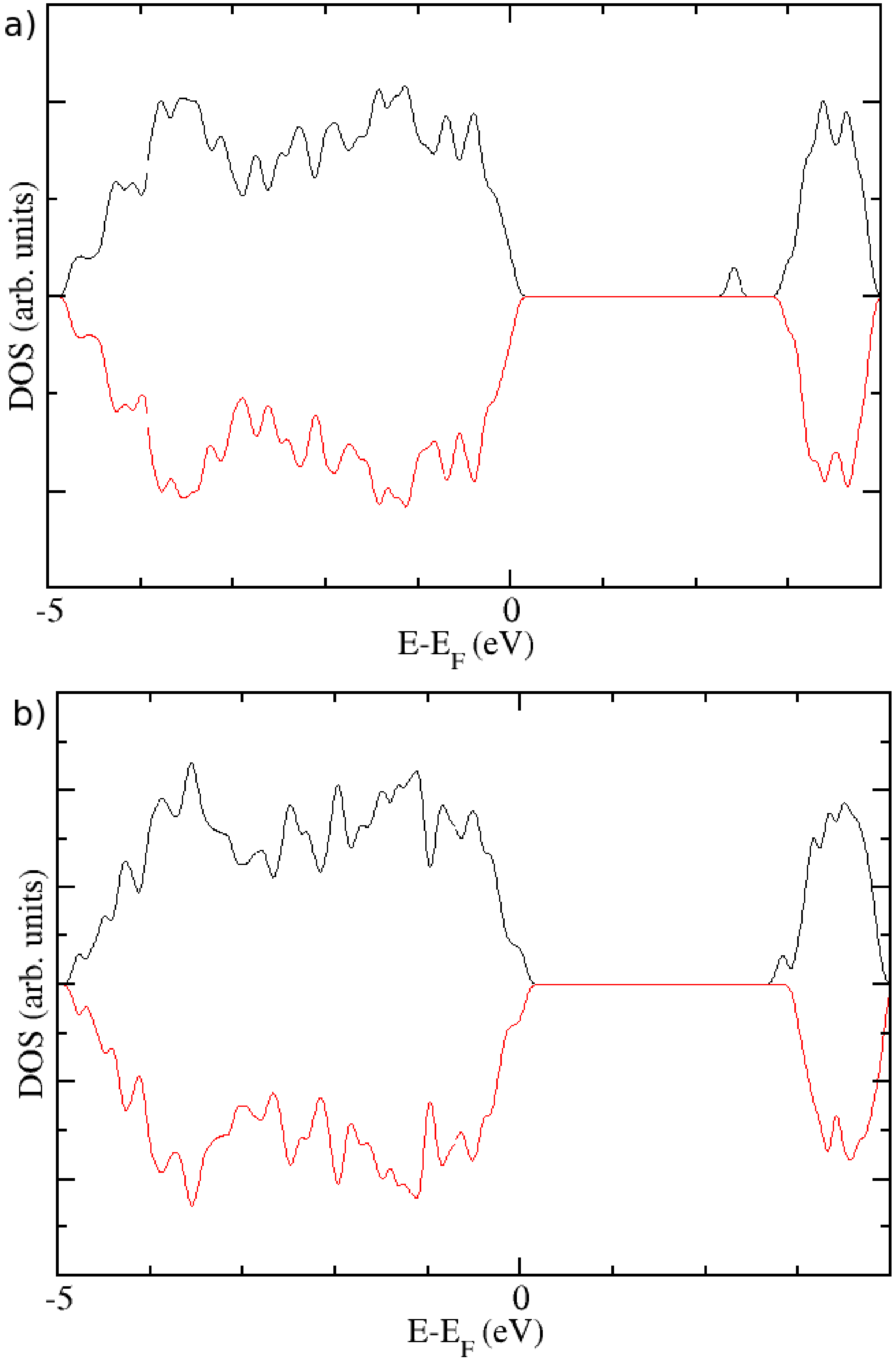

Figure 7.6: DOS of the singly charged short Ti-Zr bridge a) vacancy and b) vacancy with trapped He.

compared to 0.57 eV above the VMB for the empty vacancy (figure 7.7). The split of the defect level is due to the two holes becoming delocalised over three oxygen ions when the He atom is inside the vacancy. The three oxygen ions are from the same 6-fold coordinated polyhedron in a different Ti layer than the vacancy site (figure 7.8). The difference in chemical position of the localising oxygen ions gives rise to the different defect level structure.

The strongest trapped, neutral 5-fold coordinated Ti caused the two defect level of the empty vacancy merge to form a single defect level at 0.28 eV above the VBM. This is caused by the movement of a localised hole to a singly coordinated oxygen ion, next to the vacancy site. The other three localised holes remain on oxygen ions from the same polyhedron. The doubly charged vacancy behaved in a similar way, with the defect level doublet in the empty vacancy (0.30 eV and 0.45 eV above the VBM) becoming a singlet with a peak at 0.41 eV above the VBM when He is trapped.

The strongest effect that the trapping of He had on the electron properties of the vacancies was seen in the neutral Zr vacancy, shown in figure 7.9. The vacancy had a single defect level in the down-spin state at 0.28 eV above the VBM. However, when He is trapped in the vacancy, the down-spin defect level decreases in energy and shoulders the valence band. This coincides with the formation of two defect levels in the up-spin state at 0.59 eV and 1.67 eV above the VMB, with the lower energy level occupied, while the higher energy level is unoccupied. The shape of the valence band and conduction band edges are also changed with the presence of He in the vacancy. These changes are because three of the localised holes have moved, from three Ti-O-Ti bridges and a long Ti-Zr bridge to one Ti-O-Ti bridge and three long Ti-Zr bridges (figure 7.10). The localisation on the Ti-Zr bridges means that the defect levels are generated from different levels in the valence band, than the Ti-O bridges. Therefore, the energy increase of the level, by localising the hole, causes the defect levels to be in different positions in the band gap than the defect levels from a Ti-O bridge. The hole that remains on the Ti-O-Ti bridge changes orbital, from O p_x in the vacancy to an O p_z orbital, as figure 7.10 shows.

Aside from the changes of the position of the defect levels when He is trapped by the vacancies, the trapping of He causes the formation of a new level in the DOS. In the oxygen vacancies, this new level appears around -13 eV, compared to around -8 eV for the cation vacancies.

7.3.3 Multiple He interstitials

The interaction of multiple He atoms in a zirconolite lattice is an important issue to understand as the clustering of He will lead to the formation of bubbles and cracks within the waste form. To study whether He would cluster in zirconolite, calculations were performed with 2, 3 and 4 He interstitials per unit cell and the resulting structures were analysed.

The lowest energy configuration for the two He interstitial atoms was one in which the two He atoms sit 3.80 Å apart, with the two He atoms residing in interstitial sites that are equivalent to the site favoured by the single He interstitial (figure 7.11). This configuration is 0.11 eV less stable than having two He atoms in different unit cells, compared to 0.22 eV when the He atoms are separated by 4.03 Å and 2.08 eV with the two He atoms located within the same channel clustered together.

The configuration with three He interstitial atoms in the unit cell has the same relaxed configuration with the three He atoms occupying the lowest energy interstitial. These three He atoms are separated by a minimum distance of 6.27 Å, which indicates that the strain imposed on the lattice prevents the He from interacting. This configuration of the He atoms is 0.17 eV less stable than if the three He atoms were in different unit cells. It is 0.26 eV less stable in a configuration where two of the He atoms 3.38 Å apart and the third He in the interstitial site one Ti row below, than three separated He atoms.

An organised arrangement of He atoms is the lowest energy configuration for the four interstitials, which is lower in energy than the configuration AIRSS found, implying insufficient searches were carried out. The

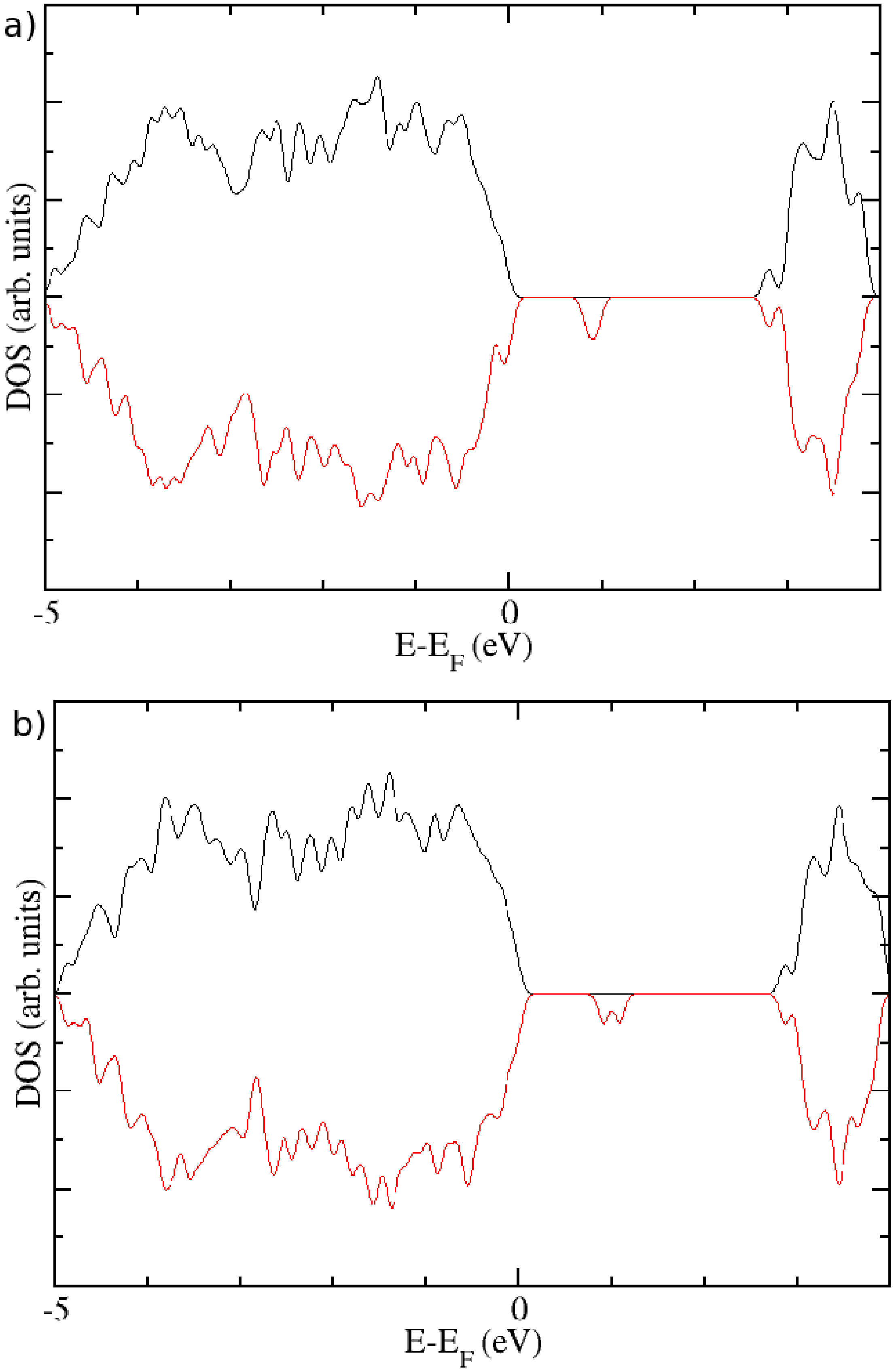

Figure 7.7: DOS of the doubly charged 2^{nd} 6-fold coordinated Ti a) vacancy and b) vacancy with trapped He.

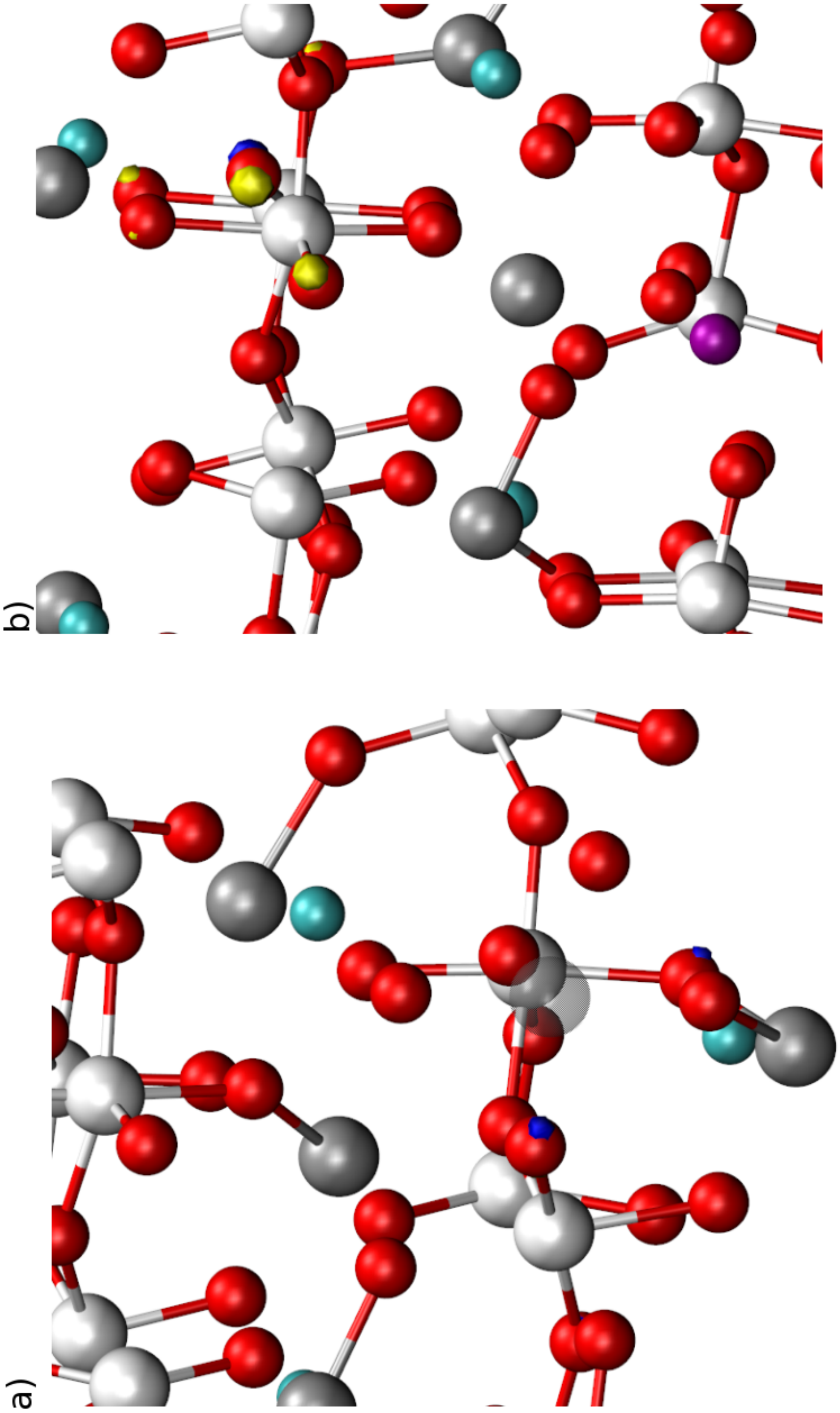

Figure 7.8: Charge density of the doubly charged 2^{nd} 6-fold coordinated Ti a) vacancy and b) vacancy with trapped He, with isosurface shown at 0.13 e Å^{-3}.

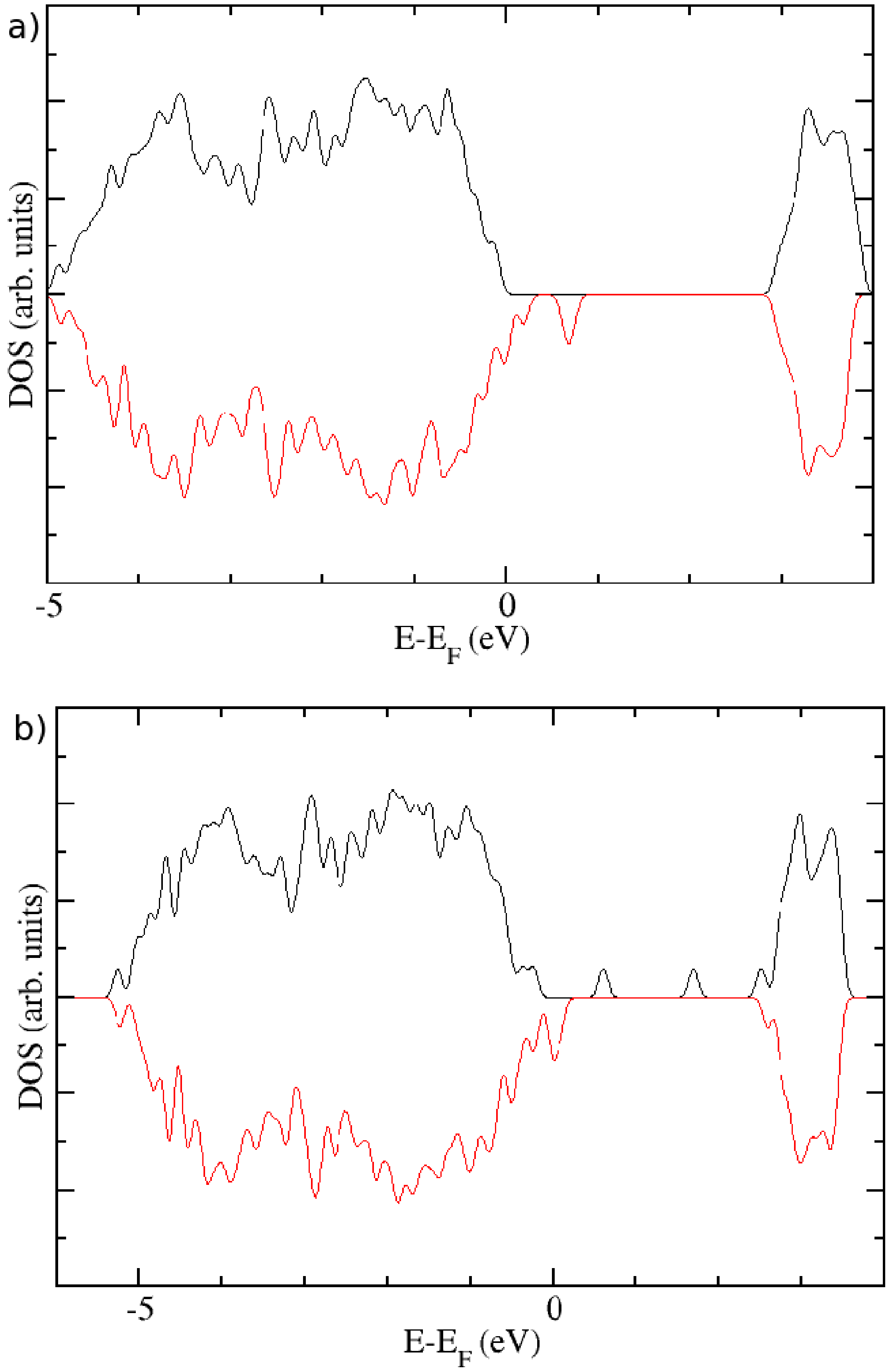

Figure 7.9: DOS of the neutral Zr a) vacancy and b) vacancy with trapped He.

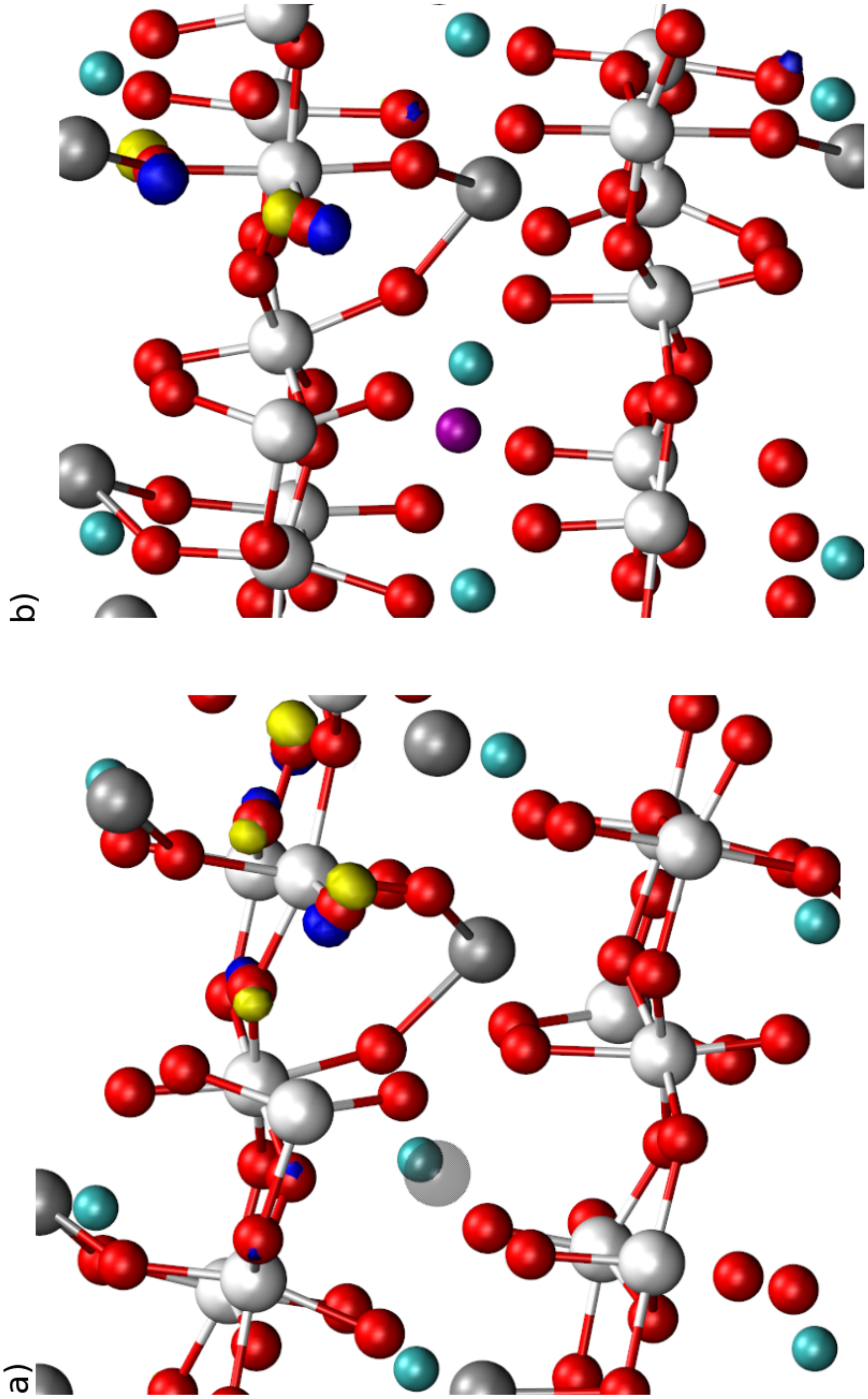

Figure 7.10: Charge density of the neutral Zr a) vacancy and b) vacancy with trapped He, with isosurface shown at 0.12 e Å^{-3}.

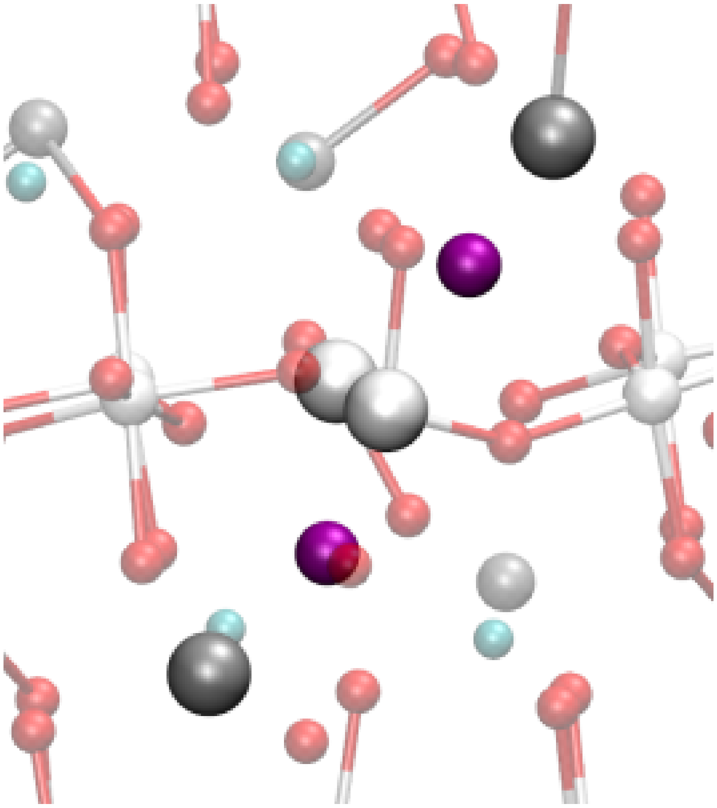

Figure 7.11: Lowest energy configuration of two He interstitials in bulk zirconolite.

Table 7.2: A summary of the % increase in the unit cell volume of zirconolite caused by the introduction of He interstitials.

Number of He interstitials	% volume increase
1	0.39
2	0.79
3	1.45
4	1.79
He in neutral 5-fold coordinated Ti vacancy	0.69

organised arrangement of He atoms involves the four interstitials located in the interstitial sites, with a minimal separation of 3.31 Å and it is 0.43 less stable than four separated He atoms. The configuration predicted by AIRSS is 0.68 eV less stable than isolated He atoms.

7.3.3.1 Volume expansion

The swelling of the lattice is an important aspect of radiation damage as this can lead to the formation of cracks and reduce the structural stability of the waste form. A 5.4% volume swelling has been observed in fully loaded ($CaPuTi_2O_7$) zirconolite which has a cubic structure,[14]] while the monoclinic zirconolite has a reported swelling of 6%.[31] The observed swelling in a material is caused by either accumulation of point defects or by the incorporation of gas bubbles, such as He. It is difficult to distinguish the contribution of each cause to the overall swelling by experimental methods. To calculate the % volume increase as a function of He interstitial concentration, cell optimisations were performed on the relaxed configuration of the He interstitials and the results are summarised in table 7.2.

As table 7.2 shows, the incorporation of He into the bulk structure results in a significant swelling of the lattice volume. The swelling caused by the inclusion of three He atoms is 29% of the total swelling observed in experiments, however the volume increases calculated in this study take no account of damage induced in the experimental studies, which will create sites for He trapping. Table 7.2 shows that the He ion trapped in the 5-fold coordinated Ti vacancy results in a larger increase in volume than the interstitial He. This is because the free space in the channels of the zirconolite crystal structure is greater than that associated with the vacancy site and therefore the substitutional He displaces the surrounding atoms more than the interstitial He. The defects created by the experimental techniques is likely to create defect clusters and the He may be incorporated into these defects.

7.4 Conclusions

We have used DFT-D3 to study the He defects in zirconolite, a proposed encapsulation matrix for Pu. The formation of He atoms inside the waste form can lead to a decrease in durability, as the formation of bubbles will lead to cracks forming due to increased stress. Therefore, an understanding of the behaviour of He in zirconolite is important if the long term performance of the waste form is to be predicted.

The position of the He interstitial in bulk zirconolite was found using AIRSS, due to the complex crystal structure. The interstitial site located was in the <010> channel, in the plane of the 6-fold coordinated Ti, 5-fold coordinated Ti and a Zr ion. The incorporation energy of the He is 1.08 eV, which is lower than for other nuclear ceramics and is consistent with the observed He retention in zirconolite. The migration barriers of the He atom were calculated using CI-NEB and found preferential migration down the <010> channel, with a barrier of 1.46 eV. The He atoms reside in low electron density sites within the zirconolite structure, this supports the current understanding of the behaviour of He defects in materials.

The binding energies of the He atom with the vacancies were calculated as trapping energies to assess possible bubble nucleation sites within zirconolite. It was found that the neutral 5-fold coordinated Ti site was the strongest trap, with a binding energy of 1.11 eV, followed by the Ca vacancies. The Ti site is the preferred trap due to the removal of electron density by the localisation of the holes associated with the vacancy on 4 of the 5 oxygen ions.

Clustering of He interstitials was not observed in bulk zirconolite at the concentrations studied, as an organised arrangement of 4 He atoms had a lower energy than a clustered configuration. A clustered arrangement may become favourable at higher concentrations than the concentration studied here.

Chapter 8

Summary

The effect of charge localisation on the properties of defects has been investigated in two ceramic materials, magnesium oxide and zirconolite. The charge state variation in the O defect structures and migration barriers were investigated in magnesium oxide, while in zirconolite the effect of charge state on the structure and binding energy of He atoms to the vacancies was studied.

DFT can describe the localisation of charge on the oxygen defects in MgO, as shown through the study of vacancies and interstitials. The magnesium defects are not described accurately by DFT, as the localisation of the holes around the vacancy cannot be correctly modelled. Alternative methods have been proposed to describe the charge trapping of the magnesium vacancies, such as hybrid functionals or DFT+U, but these methods are beyond standard DFT and also have their own associated problems, such as the U affecting all the species to which it is applied and not just the ion the holes are localised on. This research has shown that localisation of charge on defects in MgO has a significant effect on the structure and migration barriers of the O vacancies and interstitials. The structural changes associated with the oxygen interstitials as the charge state changes show that different extended defect configurations could be possible. These observed structural changes corrected experimental results into the orientation of the ${O_2}^{2-}$, from the <110> configuration observed by Halliburton and Kapper[132] to the lowest energy <111> configuration. The interstitial cluster showed that the effects observed in isolated defects are also present in larger defect clusters. The structure and migration of the hexa-interstitial cluster was affected by the localisation of charge. It was of interest that the singly charged interstitial cluster had the smallest migration barrier, in agreement with the isolated interstitial.

Zirconolite is a proposed ceramic waste host for the long term storage of waste plutonium in a geological repository. The results from this research support the use of zirconolite as an encapsulation ceramic due to the behaviour of He interstitials. This research has shown that the He will not cluster in the zirconolite bulk, at a concentration related to over 10^8 years of storage, if a 10 wt% loading is used. If He bubbles form, they could result in large stress fields in the solid and possibly the formation of cracks through the waste form. However, our results have indicated that the clustering is not likely to be a problem that will affect the long timescale integrity of the ceramic. An additional issue is that radiation damage, caused by the decay of the actinde elements, may cause amorphorisation of the lattice. The displacement of the lattice ions caused by collisions with the recoil (daughter) ion results in the creation of a large number of Frenkel pairs, which can lead to the eventual failure of the material. Although the DFT results have shown that the zirconolite lattice is easy to amorphise, with low Frenkel pair defect formation energies, experimental results have shown that this is not an issue for zirconolite encapsulation. Experimental results for leaching from an amorphous zirconolite lattice shows that the waste form still retains a good retention of the actinides species and is comparable to the crystalline results, unlike zircon. The performance of the amorphous system is one of the key factors in the use of zirconolite as a ceramic waste form, as the time scales involved in the disposal of nuclear waste mean that the waste form will remain crystalline for an insignificant amount of time in the repository.

In summary, we have demonstrated that charge localisation effects are significant for a wide range of processes and need to be considered if the evolution of defects are to be accurately described in ceramic materials. The observed radiation enhanced diffusion of the interstitials and the changes in structure of the vacancies mean that the predictions from kinetic Monte Carlo simulations, that neglect these effects, will be incorrect. The overestimation is unable to be quantified without further work.

Chapter 9

Future work

This chapter looks at the topics that could not be investigated in this research due to time restraints. However, discussed below is the research I would have liked to have done if I had sufficient time. This work could be carried out in future by someone wishing to extend the work I have produced.

As this research has focused on oxygen vacancies in MgO, it would be of interest to see whether similar effects were present for the magnesium defects. As discussed in this work, standard DFT methods cannot be used for this study. The localisation of a hole on the Mg vacancies can be described correctly using hybrid functionals (B3LYP, PBE0, etc.) or using the Hubbard U method (DFT+U). The migration barriers could then be calculated in the different charge states and compared to the O vacancies. This would show whether charge localisation had a larger effect on the cation or anion. The Mg interstitial may be more problematic as the conduction band of MgO is constructed from Mg *s* orbitals, so the localisation of electrons on to the interstitial may not be possible. This is because the electron would have to be localised on a delocalised state. Therefore, the interstitial state must be lower in energy than the conduction band to allow the electron to localise on the interstitial or it would be more energetic to delocalise the electron, as seen in these calculations.

The hexa-interstitial cluster has been studied in three charge states: neutral, singly- and doubly-charged. However, as there are three oxide ions in this interstitial cluster, there is the possibility of localising six holes, two on each oxide ion. The first three charge states were only studied due to the limited size of the simulation cell. This restricted the charge we could study without excess charge interactions occurring between periodic images. A larger supercell would be needed to study the higher charged clusters but the computational expense of this is currently excessive. It would be of interest to study whether the trends in the charge dependence already identified continue in the higher charge states, when large supercells become computationally accessible.

The interstitial cluster has only been studied with the localisation of holes, however electrons should also localise on the cluster. A test calculation was run with an extra electron using DFT but the electron delocalised over the whole cell. Therefore, to study the localisation of up to six electrons on the cluster, a computational method similar to that used for the magnesium interstitial would be needed. Studying the localised electron would be interesting to see if a similar change occurred in the barrier height of the interstitial cluster. This would allow a comparison between the effects on mobility of localised holes and electrons.

The structure of the intrinsic defects in zirconolite was studied in different charge states but the migration barriers were not calculated. As the defects seemed to have simple migration pathways, it would be useful to calculate these and compare to the results from the constituent oxides. This would allow an extra test of the suitability of comparing the results in zirconolite and the oxides, due to the limited available data for zirconolite. The migration barriers of the defects are also inportant to allow predictions on the defect evolution over time. If the migration barriers are high, this may also explain why little self-healing of an irradiation event occurs. I have shown that the low Frenkel pair energies of the defects may be the cause of the low structural recovery but high defect migration barriers would also contribute to this. It would also be interesting to understand the effect of the O_2 molecules on the diffusion of the vacancies, as this would have an effect on the evolution of damage within the crystal and affect the long time durability of the waste form. The effect of He atoms trapped in the vacancies are also of interest as these would have similar effects to the O_2 molecules, they would prevent the predicted diffusion pathway of the vacancies, which would likely increase the migration barriers.

The migration barrier will play an important role in the formation of bubbles within the zirconolite lattice, therefore an accurate description of the barrier is important. The multi-barrier migration of He through zirconolite means that other low energy pathways are likely to be present, but the expense of the NEB method means that it is not feasible to search for other pathways. I believe it would be interesting to use a different methodology that would allow basin searches to identify other pathways and possibly give a calculated barrier in closer agreement to the experimentally observed value. Also, the effect of He accumulation has on the migration of a He atom would be of interest. Would the build up of He interstitials and the distortions created, aid or hinder the migration of one of the He atoms through the lattice? This combined with the effect that vacancies have on the migration pathway would allow an understanding of how He would migrate towards bubbles and grain boundaries. This would allow calculations of bubble growth rates and other factors that would have an effect on the durability of the zirconolite structure.

The National Nuclear Laboratory (NNL) is favouring a composite waste form for the disposal of Pu because it means that impure PuO_2 can be encapsulated. An understanding of the interface between the zirconolite and glass is important. A fundamental understanding of the basic defect properties at the interface would allow predictions of the durability of the waste form to be made. The properties of the He interstitials at the interface would have a significant effect on the durability of the waste form, if He atoms clustered at the interface it would cause a large amount of stress in the system and lead to cracking of the waste form. There has been previous work on charge localisation in amorphous SiO_2 using B3LYP, with the amount of exact exchange altered. This provides results against which part of the model can be tested. The result of a decay event at the interface would be of interest to study as it would show the amount of mixing of the interface and the effect that this may have on the erosion of the interface. However, this would require classical methods and it would be difficult to develop accurate potentials for the interface region. To find the lowest energy interface structure would require a large amount of computational time because there is currently no experimental investigation of the glass-zirconolite interface to aid modellers. Therefore, more experimental studies on the interface are needed, such as AFM, to help limit the number of interfaces that would need to be investigated. To make an accurate description of the interface region would require an experimental-computational collaboration, where the results would feed into each other's research due to the complexity of the interface.

Bibliography

[1] J. Mulroue and D. M. Duffy, “An ab initio study of the effect of charge localization on oxygen defect formation and migration energies in magnesium oxide,” *Proceedings of the Royal Society A: Mathematical, Physical and Engineering Sciences*, p. 1471, Mar. 2011.

[2] H. J. Rossell, “Zirconolite a fluorite-related superstructure,” *Nature*, vol. 283, pp. 282–283, Jan. 1980.

[3] J. Mulroue, A. Morris, and D. Duffy, “Ab initio study of intrinsic defects in zirconolite,” *Physical Review B*, vol. 84, pp. 1–8, Sept. 2011.

[4] SRIM, “http://www.srim.org,” 2008.

[5] WNA, “www.world-nuclear.org,” 2012.

[6] NDA, “http://www.nda.gov.uk/,” 2012.

[7] A. Setiadi, N. B. Milestone, J. Hill, and M. Hayes, “Corrosion of aluminium and magnesium in BFS composite cements,” *Advances in Applied Ceramics*, vol. 105, no. 4, p. 6, 2006.

[8] T. Baldwin, N. Chapman, and F. Neall, “Geological Disposal Options for High-Level Waste and Spent Fuel Report for the UK Nuclear Decommissioning Authority,” *Sciences-New York*, no. January, 2008.

[9] D. Strachan, R. Scheele, J. Icenhower, E. Buck, A. Kozelisky, R. Sell, R. Elovich, and W. Buchmiller, “Radiation Damage Effects in Candidate Ceramics for Plutonium Immobilization,” tech. rep., Pacific Northwest National Laboratory, 2004.

[10] A. E. Ringwood, S. E. Kesson, N. G. Ware, W. Hibberson, and A. Major, “Immobilisation of high level nuclear reactor wastes in SYNROC,” *Nature*, vol. 278, pp. 219–223, Mar. 1979.

[11] M. Gilbert, C. Davoisine, M. Stennett, N. Hyatt, N. Peng, C. Jeynes, and W. Lee, “Krypton and Helium Irradiation Damage in Neodymium-Zirconolite,” *Journal of Nuclear Materials*, pp. 221–224, Dec. 2010.

[12] A. Ringwood, V. Oversby, S. Kesson, W. Sinclair, N. Ware, W. Hibberson, and a. Major, “Immobilization of high-level nuclear reactor wastes in SYNROC: A current appraisal,” *Nuclear and Chemical Waste Management*, vol. 2, no. 4, pp. 287–305, 1981.

[13] M. R. Gilbert, C. Selfslag, M. Walter, M. C. Stennett, J. Somers, N. C. Hyatt, and F. R. Livens, “Synthesis and characterisation of Pu-doped zirconolites (Ca 1-x Pu x)Zr(Ti 2-2x Fe 2x)O 7,” *IOP Conference Series: Materials Science and Engineering*, vol. 9, p. 012007, Mar. 2010.

[14] F. Clinard Jr, D. Peterson, D. Rohr, and L. Hobbs, “Self-irradiation effects in 238Pu-substituted zirconolite. Temperature dependence of damage,” *Journal of Nuclear Materials*, vol. 126, pp. 245–254, Nov. 1984.

[15] R. C. Ewing, “Nuclear waste forms for actinides.,” *Proceedings of the National Academy of Sciences of the United States of America*, vol. 96, pp. 3432–9, Mar. 1999.

[16] T. Geisler, K. Trachenko, S. Ríos, M. T. Dove, and E. K. H. Salje, “Impact of self-irradiation damage on the aqueous durability of zircon (ZrSiO 4): implications for its suitability as a nuclear waste form,” *Journal of Physics: Condensed Matter*, vol. 15, pp. L597–L605, Sept. 2003.

[17] C. Barbé, R. Graf, K. Finnie, M. Blackford, R. Trautman, and J. Bartlett, “Sol-Gel Synthesis of Complex Titanates in Micro-Emulsions,” 2003.

[18] E. Sizgek, J. Bartlett, and M. Brungs, “Production of Titanate Microspheres by Sol-Gel and Spray-Drying,” 1998.

[19] R. Ewing, W. Lutze, and W. J. Weber, “Zircon: A host-phase for the disposal of weapons plutonium,” *Journal of Materials Research*, vol. 10, pp. 243–246, Feb. 1995.

[20] W. J. Weber, R. C. Ewing, and L.-M. Wang, “The radiation-induced crystalline-to-amorphous transition in zircon,” *Journal of Materials Research*, vol. 9, pp. 688–698, Mar. 1994.

[21] T. Murakami, B. Chakoumakos, R. Ewing, G. Lumpkin, and W. Weber, “Alpha-decay event damage in zircon,” *American Mineralogist*, vol. 76, no. 9-10, p. 1510, 1991.

[22] Balwin T, Chapman N, and Neall F, “Geological Disposal Options for High-Level Waste and Spent Fuel,” tech. rep., National Decommissioning Authority, 2008.

[23] NDA, “NDA Plutonium Topic Strategy ,” tech. rep., NDA, 2009.

[24] CCFE, “www.ccfe.ac.uk,” 2012.

[25] N. Aoi, K. Yoneda, E. Ideguchi, T. Kishida, T. Nakamura, M. Notani, H. Sakurai, T. Teranishi, Y. Watanabe, H. Wu, A. Yoshida, H. Miyatake, Y. Yamamoto, H. Ogawa, S. Yamamoto, and M. Ishihara, “Anomaly of N=8 shell closure in neutron-rich Be and B isotopes studied via delayed neutron emitting 14Be β decay,” *Physical Review C*, vol. 66, pp. 041301–041312, June 2002.

[26] “Lawrence Berkeley National laboratory,http://www.lbl.gov/,” 2012.

[27] F. Bahrassa and R. Datta, “Postoperative beta radiation treatment of pterygium,” *International Journal of Radiation Oncology*Biology*Physics*, vol. 9, pp. 679–684, May 1983.

[28] D. Duffy, S. Daraszewicz, and J. Mulroue, “Modelling the effects of electronic excitations in ionic-covalent materials,” *Nuclear Instruments and Methods in Physics Research Section B: Beam Interactions with Materials and Atoms*, pp. 21–27, Dec. 2011.

[29] H. Trinkaus and B. Singh, “Helium accumulation in metals during irradiation - where do we stand?,” *Journal of Nuclear Materials*, vol. 323, pp. 229–242, Dec. 2003.

[30] H. E. Hansen, H. Rajainmaki, R. Talja, M. D. Bentzon, R. M. Nieminen, and K. Petersen, “Helium bubbles in alpha-irradiated aluminium: positron lifetime studies,” *Journal of Physics F: Metal Physics*, vol. 15, pp. 1–10, Jan. 1985.

[31] T. Wiss, X. Deschanels, J. Hiernaut, D. Roudil, S. Peuget, and V. Rondinella, “Helium release from plutonium and curium-doped zirconolite,” *Journal of Nuclear Materials*, vol. 362, no. 2-3, pp. 431–437, 2007.

[32] T. Wiss, J. Hiernaut, P. Damen, S. Lutique, R. Fromknecht, and W. Weber, “Helium behaviour in waste conditioning matrices during thermal annealing,” *Journal of Nuclear Materials*, vol. 352, no. 1-3, pp. 202–208, 2006.

[33] P. Zhang, Y. Lu, C.-H. He, and P. Zhang, “First-principles study of the incorporation and diffusion of helium in cubic zirconia,” *Journal of Nuclear Materials*, vol. 418, pp. 143–151, Nov. 2011.

[34] H. Iwakiri, K. Yasunaga, K. Morishita, and N. Yoshida, “Microstructure evolution in tungsten during low-energy helium ion irradiation,” *Journal of Nuclear Materials*, vol. 283-287, pp. 1134–1138, Dec. 2000.

[35] S. M. Hafez Haghighat, G. Lucas, and R. Schäublin, “State of a pressurized helium bubble in iron,” *Europhysics Letters*, vol. 85, p. 60008, Mar. 2009.

[36] E. Lee, J. Hunn, T. Byun, and L. Mansur, “Effects of helium on radiation-induced defect microstructure in austenitic stainless steel,” *Journal of Nuclear Materials*, vol. 280, pp. 18–24, June 2000.

[37] H. Smith and D. Michel, “The effect of irradiation on the fatigue and flow behavior of TZM alloy,” *Journal of Nuclear Materials*, vol. 66, pp. 125–142, Apr. 1977.

[38] G. Brillant, F. Gupta, and A. Pasturel, “Fission products stability in uranium dioxide,” *Journal of Nuclear Materials*, vol. 412, pp. 170–176, May 2011.

[39] Y. Yun, O. Eriksson, P. M. Oppeneer, H. Kim, and K. Park, “First-principles theory for helium and xenon diffusion in uranium dioxide,” *Journal of Nuclear Materials*, vol. 385, pp. 364–367, Mar. 2009.

[40] M. Reich, R. C. Ewing, T. A. Ehlers, and U. Becker, “Low-temperature anisotropic diffusion of helium in zircon: Implications for zircon (U-Th)/He thermochronometry,” *Geochimica et Cosmochimica Acta*, vol. 71, pp. 3119–3130, June 2007.

[41] I. Saadoune, J. Purton, and N. De Leeuw, “He incorporation and diffusion pathways in pure and defective zircon ZrSiO4: A density functional theory study,” *Chemical Geology*, vol. 258, pp. 182–196, Jan. 2009.

[42] L. Smith and E. Moore, *Solid State Chemistry*. Tylor and Francis, third ed., 2005.

[43] L. W. Hobbs, A. E. Hughes, and D. Pooley, “A Study of Interstitial Clusters in Irradiated Alkali Halides Using Direct Electron Microscopy,” *Proceedings of the Royal Society A: Mathematical, Physical and Engineering Sciences*, vol. 332, pp. 167–185, Mar. 1973.

[44] J. Jeffries, M. Wall, K. Moore, and A. Schwartz, “He bubble coarsening by migration and coalescence in annealed PuGa alloys,” *Journal of Nuclear Materials*, vol. 410, pp. 84–88, Mar. 2011.

[45] S. Miro, J. Costantini, J. Haussy, L. Beck, S. Vaubaillon, S. Pellegrino, C. Meis, J. Grob, Y. Zhang, and W. Weber, “Nuclear reaction analysis of helium migration in silicon carbide,” *Journal of Nuclear Materials*, vol. 415, pp. 5–12, Aug. 2011.

[46] A. L. Shluger, K. P. McKenna, P. V. Sushko, D. M. n. Ramo, and A. V. Kimmel, “Modelling of electron and hole trapping in oxides,” *Modelling and Simulation in Materials Science and Engineering*, vol. 17, p. 084004, Dec. 2009.

[47] P. Hohenberg and W. Kohn, “Inhomogeneous Electron Gas,” *Physical Review*, vol. 136, no. 3B, pp. B864–B871, 1964.

[48] R. Martin, *Electronic structure : basic theory and practical methods*. Cambridge University Press, 2004.

[49] L. Kantorovich, *Quantum Theory of the solid state: An Introduction*. Dordrecht: Kluwer Academic Publishers.

[50] J. Perdew, J. Chevary, S. Vosko, K. Jackson, M. Pederson, D. Singh, and C. Fiolhais, "Atoms, molecules, solids, and surfaces: Applications of the generalized gradient approximation for exchange and correlation," *Physical Review B*, vol. 46, pp. 6671–6687, Sept. 1992.

[51] A. P. Scott and L. Radom, "Harmonic Vibrational Frequencies: An Evaluation of Hartree-Fock, Møller-Plesset, Quadratic Configuration Interaction, Density Functional Theory, and Semiempirical Scale Factors," *The Journal of Physical Chemistry*, vol. 100, pp. 16502–16513, Jan. 1996.

[52] T. Ziegler, "Approximate density functional theory as a practical tool in molecular energetics and dynamics," *Chemical Reviews*, vol. 91, pp. 651–667, July 1991.

[53] P. M. W. Gill, B. G. Johnson, J. A. Pople, and M. J. Frisch, "An investigation of the performance of a hybrid of Hartree-Fock and density functional theory," *International Journal of Quantum Chemistry*, vol. 44, pp. 319–331, Mar. 1992.

[54] D. R. Bowler, T. Miyazaki, and M. J. Gillan, "Recent progress in linear scaling ab initio electronic structure techniques," *Journal of Physics: Condensed Matter*, vol. 14, pp. 2781–2798, Mar. 2002.

[55] C. Fonseca Guerra, J. G. Snijders, G. te Velde, and E. J. Baerends, "Towards an order- N DFT method," *Theoretical Chemistry Accounts: Theory, Computation, and Modeling (Theoretica Chimica Acta)*, vol. 99, pp. 391–403, Nov. 1998.

[56] G. E. Scuseria, "Linear Scaling Density Functional Calculations with Gaussian Orbitals," *The Journal of Physical Chemistry A*, vol. 103, pp. 4782–4790, June 1999.

[57] S. Lany and A. Zunger, "Accurate prediction of defect properties in density functional supercell calculations," *Modelling and Simulation in Materials Science and Engineering*, vol. 17, p. 084002, Dec. 2009.

[58] S. Lany, "Magnetic interactions of Cr-Cr and Co-Co impurity pairs in ZnO within a band-gap corrected density functional approach," *Physical Review B*, vol. 77, no. 24, 2008.

[59] M. Payne, M. Teter, D. Allan, T. Arias, and J. Joannopoulos, "Iterative minimization techniques for ab initio total-energy calculations: molecular dynamics and conjugate gradients," *Reviews of Modern Physics*, vol. 64, pp. 1045–1097, Oct. 1992.

[60] G. Mills, "Reversible work transition state theory: application to dissociative adsorption of hydrogen," *Surface Science*, vol. 324, pp. 305–337, Feb. 1995.

[61] J. Vande Vondele, M. Krack, F. Mohamed, M. Parrinello, T. Chassaing, and J. Hutter, "Quickstep: Fast and accurate density functional calculations using a mixed Gaussian and plane waves approach," *Computer Physics Communications*, vol. 167, no. 2, pp. 103–128, 2005.

[62] S. Grimme, "Density functional theory with London dispersion corrections," *Wiley Interdisciplinary Reviews: Computational Molecular Science*, vol. 1, pp. 211–228, Mar. 2011.

[63] J.-D. Chai and M. Head-Gordon, “Long-range corrected hybrid density functionals with damped atom-atom dispersion corrections.,” *Physical chemistry chemical physics : PCCP*, vol. 10, pp. 6615–20, Nov. 2008.

[64] H. B. G. Casimir and D. Polder, “The Influence of Retardation on the London-van der Waals Forces,” *Physical Review*, vol. 73, pp. 360–372, Feb. 1948.

[65] M. Lein, J. F. Dobson, and E. K. U. Gross, “Toward the description of van der Waals interactions within density functional theory,” *Journal of Computational Chemistry*, vol. 20, pp. 12–22, Jan. 1999.

[66] G. Henkelman, A. Arnaldsson, and H. Jonsson, “A fast and robust algorithm for Bader decomposition of charge density,” *Computational Materials Science*, vol. 36, pp. 354–360, June 2006.

[67] R. Gonzalez, Y. Chen, D. Caceres, and I. Vergara, “Impurity effects in neutron-irradiated simple oxides: Implications for fusion devices,” *Nuclear Instruments and Methods in Physics Research Section B: Beam Interactions with Materials and Atoms*, vol. 250, no. 1-2, pp. 324–329, 2006.

[68] Y. Oishi and W. D. Kingery, “Oxygen Diffusion in Periclase Crystals,” *The Journal of Chemical Physics*, vol. 33, p. 905, Sept. 1960.

[69] H. Hashimoto, “Preferential diffusion of oxygen along grain boundaries in polycrystalline MgO,” *Journal of Applied Physics*, vol. 43, p. 4828, Nov. 1972.

[70] S. Shirasaki and M. Hama, “Oxygen-diffusion characteristics of loosely-sintered polycrystalline MgO,” *Chemical Physics Letters*, vol. 20, pp. 361–365, June 1973.

[71] K. W.D., ed., *Advances in ceramics Volume 10: Structure and Properties of MgO and Al2O3 Ceramics*. The American ceramic society, 1983.

[72] D. R. Sempolinski and W. D. Kingery, “Ionic Conductivity and Magnesium Vacancy Mobility in Magnesium Oxide,” *Journal of the American Ceramic Society*, vol. 63, pp. 664–669, Nov. 1980.

[73] M. Duclot and C. Deportes, “Influence des impuretés sur la conductivité cationique dans l’oxyde de magnesium monocristallin,” *Journal of Solid State Chemistry*, vol. 31, pp. 377–385, Mar. 1980.

[74] B. J. Wuensch, “Cation self-diffusion in single-crystal MgO,” *The Journal of Chemical Physics*, vol. 58, p. 5258, June 1973.

[75] J. Narayan and J. Washburn, “Self diffusion in magnesium oxide,” *Acta Metallurgica*, vol. 21, pp. 533–538, May 1973.

[76] B. C. Harding, D. M. Price, and A. J. Mortlock, “Cation self-diffusion in single crystal MgO,” *Philosophical Magazine*, vol. 23, pp. 399–408, Feb. 1971.

[77] C. A.R and H. A.H, eds., *Mass transport phenomena in ceramics*. New York: Plenum, 1975.

[78] W. H. Gourdin and W. D. Kingery, “The defect structure of MgO containing trivalent cation solutes: shell model calculations,” *Journal of Materials Science*, vol. 14, pp. 2053–2073, Sept. 1979.

[79] L. Halliburton, L. Kappers, D. Cowan, F. Dravnieks, and J. Wertz, “Isotropic ESR Line of the V^{-} Center in MgO at Room Temperature,” *Physical Review Letters*, vol. 30, pp. 607–610, Mar. 1973.

[80] B H Rose and L E Halliburton, “Esr hyperfine investigation of the v 0 centre in mgo,” 1974.

[81] J. E. Wertz, P. Auzins, J. H. E. Griffiths, and J. W. Orton, "III. Spin resonance studies of defects in magnesium oxide," *Discussions of the Faraday Society*, vol. 28, p. 136, 1959.

[82] J. Wertz, P. Auzins, R. Weeks, and R. Silsbee, "Electron Spin Resonance of F Centers in Magnesium Oxide; Confirmation of the Spin of Magnesium-25," *Physical Review*, vol. 107, pp. 1535–1537, Sept. 1957.

[83] M. Sterrer, E. Fischbach, T. Risse, and H.-J. Freund, "Geometric Characterization of a Singly Charged Oxygen Vacancy on a Single-Crystalline MgO(001) Film by Electron Paramagnetic Resonance Spectroscopy," *Physical Review Letters*, vol. 94, no. 18, pp. 1–4, 2005.

[84] G. Busker, "Predicted vacancy cluster structures in MgO and their interaction with helium," *Nuclear Instruments and Methods in Physics Research Section B: Beam Interactions with Materials and Atoms*, vol. 171, pp. 528–536, Dec. 2000.

[85] G. V. Lewis and C. R. A. Catlow, "Potential models for ionic oxides," *Journal of Physics C: Solid State Physics*, vol. 18, pp. 1149–1161, Feb. 1985.

[86] B. Uberuaga, R. Smith, A. Cleave, G. Henkelman, R. Grimes, A. Voter, and K. Sickafus, "Dynamical simulations of radiation damage and defect mobility in MgO," *Physical Review B*, vol. 71, no. 10, p. 104102, 2005.

[87] E. Kotomin and a. Popov, "Radiation-induced point defects in simple oxides," *Nuclear Instruments and Methods in Physics Research Section B: Beam Interactions with Materials and Atoms*, vol. 141, pp. 1–15, May 1998.

[88] C. Gilbert, S. Kenny, R. Smith, and E. Sanville, "Ab initio study of point defects in magnesium oxide," *Physical Review B*, vol. 76, no. 18, pp. 1–10, 2007.

[89] W. C. Mackrodt and R. F. Stewart, "Defect properties of ionic solids : 111. The calculation of the point-defect structure of the alkaline-earth oxides and CdO," vol. 12, 1979.

[90] C. Catlow, I. Faux, and M. Norgett, "Shell and breathing shell model calculations for defect formation energies and volumes in magnesium oxide," *Journal of Physics C: Solid State Physics*, vol. 9, no. 1971, pp. 419–430, 1976.

[91] L. Vočadlo, A. Wall, S. Parker, and G. D. Price, "Absolute ionic diffusion in MgO - computer calculations via lattice dynamics," *Physics of the Earth and Planetary Interiors*, vol. 88, pp. 193–210, Apr. 1995.

[92] L. Kittiratanawasin, R. Smith, B. Uberuaga, and K. Sickafus, "Displacement threshold and Frenkel pair formation energy in ionic systems," *Nuclear Instruments and Methods in Physics Research Section B: Beam Interactions with Materials and Atoms*, vol. 268, pp. 2901–2906, Oct. 2010.

[93] A. De Vita, M. Gillan, J. Lin, M. Payne, I. Štich, and L. Clarke, "Defect energetics in MgO treated by first-principles methods," *Physical Review B*, vol. 46, pp. 12964–12973, Nov. 1992.

[94] W. Weber, J. Wald, and H. Matzke, "Effects of self-radiation damage in Cm-doped Gd2Ti2O7 and CaZrTi2O7," *Journal of Nuclear Materials*, vol. 138, pp. 196–209, Apr. 1986.

[95] D. Strachan, R. Scheele, E. Buck, A. Kozelisky, R. Sell, R. Elovich, and W. Buchmiller, "Radiation damage effects in candidate titanates for Pu disposition: Zirconolite," *Journal of Nuclear Materials*, vol. 372, pp. 16–31, Jan. 2008.

[96] Hyatt N, “MRS talk,” in *Scientific Basis for Nuclear Waste Management*, MRS, 2012.

[97] G. Lumpkin, “Application of analytical electron microscopy to the study of radiation damage in the complex oxide mineral zirconolite,” *Micron*, vol. 28, pp. 57–68, Feb. 1997.

[98] S. Wang, “Ion irradiation-induced amorphization of six zirconolite compositions,” *Nuclear Instruments and Methods in Physics Research Section B: Beam Interactions with Materials and Atoms*, vol. 166-167, pp. 293–298, May 2000.

[99] R. Ewing and L. Wang, “Amorphization of zirconolite: alpha-decay event damage versus krypton ion irradiation,” *Nuclear Instruments and Methods in Physics Research Section B: Beam Interactions with Materials and Atoms*, vol. 65, pp. 319–323, Mar. 1992.

[100] J. Wald and P. Offemann, “A Study of Radiation Effects in Curium-Doped Gd2Ti2O7 (Pyrochlore) and CaZrTi2O7 (Zirconolite),” *MRS Proceedings*, vol. 11, Jan. 1981.

[101] D. M. Strachan, R. D. Scheele, A. E. Kozelisky, R. L. Sell, H. T. Schaef, M. J. O’Hara, C. F. Brown, Buchmiller, and W. C., “Radiation Damage in Titanate Ceramics for Plutonium Immobilization,” *MRS Proceedings*, vol. 713, Jan. 2002.

[102] Sinclair W and Ringwood AW, “Alpha-recoil damage in natural zirconolite and perovskite,” *Geochemical Journal*, vol. 15, no. 5, pp. 229–243, 1981.

[103] S. Wang, “Ion irradiation-induced phase transformation of pyrochlore and zirconolite,” *Nuclear Instruments and Methods in Physics Research Section B: Beam Interactions with Materials and Atoms*, vol. 148, pp. 704–709, Jan. 1999.

[104] K. Smith, “In situ studies of ion irradiated zirconolite, pyrochlore and perovskite,” *Journal of Nuclear Materials*, vol. 250, pp. 36–52, Nov. 1997.

[105] R. C. Ewing and T. J. Headley, “Alpha-recoil damage in natural zirconolite (CaZrTi2O7),” *Journal of Nuclear Materials*, vol. 119, pp. 102–109, Nov. 1983.

[106] D. Reid, M. Stennett, B. Ravel, J. Woicik, N. Peng, E. Maddrell, and N. Hyatt, “The structure of ion beam amorphised zirconolite studied by grazing angle X-ray absorption spectroscopy,” *Nuclear Instruments and Methods in Physics Research Section B: Beam Interactions with Materials and Atoms*, pp. 1847–1852, Feb. 2010.

[107] C. Fillet, T. Advocat, F. Bart, G. Leturcq, and H. Rabiller, “Titanate-based ceramics for separated long-lived radionuclides,” *Comptes Rendus Chimie*, vol. 7, pp. 1165–1172, Dec. 2004.

[108] H. Larguem, P. Trocellier, M. Tarrida, M. Madon, S. Poissonnet, D. Gosset, O. Leseigneur, H. Martin, P. Bonnaillie, L. Beck, S. Vaubaillon, and S. Miro, “Chemical reactivity and ion beam irradiation behaviour of perovskite- and zirconolite-nuclear ceramics type,” *Nuclear Instruments and Methods in Physics Research Section B: Beam Interactions with Materials and Atoms*, vol. 249, pp. 140–144, Aug. 2006.

[109] Pöml P, Geisler T, Cobos-Sabaté J, Wiss T, Raison PE, Schmid-Beurmann P, Deschanels X, Jégou C, Heimink J, and Putnis A, “The mechanism of the hydrothermal alteration of cerium- and plutonium-doped zirconolite,” *Journal of Nuclear Materials*, vol. 410, no. 1-3, pp. 10–23, 2011.

[110] V. Oversby and A. Ringwood, “Lead Isotopic Studies of Zirconolite and Perovskite and Their Implications for Long Range Synroc Stability,” *Rad. Waste Man*, vol. 1, pp. 289–307, 1981.

[111] J. H. Hadley, F. H. Hsu, Y. Hu, R. V. Eric, and D. B. Bruce, “Observation of Vacancies by Positron Trapping in Cerium-Doped Zirconolites,” *Journal of the American Ceramic Society*, vol. 82, pp. 203–205, Dec. 2004.

[112] J. H. Hadley, F. H. Hsu, E. R. Vance, M. Colella, K. L. Smith, G. R. Lumpkin, M. L. Carter, and B. D. Begg, “Cation vacancies in doped zirconolite (CaZrTi2O7),” *Journal of Materials Science*, vol. 40, pp. 6029–6032, Sept. 2005.

[113] J. Ziegler, *The Stopping and Range of Ions in Solids* . Pergamon, 1985.

[114] L. Veiller, J. Crocombette, and D. Ghaleb, “Molecular dynamics simulation of the α-recoil nucleus displacement cascade in zirconolite,” *Journal of Nuclear Materials*, vol. 306, pp. 61–72, Nov. 2002.

[115] H. Chappell, M. Dove, K. Trachenko, R. McKnight, E. Artacho, and S. Redfern, “Structural changes in zirconolite under alpha-decay,” *Journal of Physics: Condensed Matter*, vol. in press, 2012.

[116] K. Trachenko, M. T. Dove, E. Artacho, I. T. Todorov, and W. Smith, “Atomistic simulations of resistance to amorphization by radiation damage,” *Physical Review B*, 2006.

[117] Y. Zhang, I. Bae, and W. Weber, “Atomic collision and ionization effects in oxides,” *Nuclear Instruments and Methods in Physics Research Section B: Beam Interactions with Materials and Atoms*, vol. 266, no. 12-13, pp. 2828–2833, 2008.

[118] C. Ortiz and M. Caturla, “Simulation of defect evolution in irradiated materials: Role of intracascade clustering and correlated recombination,” *Physical Review B*, vol. 75, May 2007.

[119] A. Rutherford and D. Duffy, “The effect of electron-ion interactions on radiation damage simulations,” *Journal of Physics: Condensed Matter*, vol. 19, p. 496201, 2007.

[120] D. M. Duffy, N. Itoh, a. M. Rutherford, and a. M. Stoneham, “Making tracks in metals,” *Journal of Physics: Condensed Matter*, vol. 20, no. 8, p. 082201, 2008.

[121] C. P. Race, D. R. Mason, and A. P. Sutton, “Electronic excitations and their effect on the interionic forces in simulations of radiation damage in metals,” *Journal of Physics: Condensed Matter*, vol. 21, p. 115702, Mar. 2009.

[122] Itoh N. and A. M. Stoneham, *Materials modification by electronic excitation* . Cambridge: Cambridge University Press, 2001.

[123] Y. Chen and M. Abraham, “Trapped-hole centers in alkaline-earth oxides,” *Journal of Physics and Chemistry of Solids*, vol. 51, pp. 747–764, Jan. 1990.

[124] P. E. Blöchl, “Projector augmented-wave method,” *Physical Review B*, vol. 50, pp. 17953–17979, Dec. 1994.

[125] G. Kresse, “From ultrasoft pseudopotentials to the projector augmented-wave method,” *Physical Review B*, vol. 59, pp. 1758–1775, Jan. 1999.

[126] N. G. Schmahl and G. F. Eikerling, “Cryptomodifications of copper(II) oxide,” *Z. Phys. Chem. Neue Folge*, vol. 62, p. 268, 1968.

[127] J. Carrasco, N. Lopez, and F. Illas, “First Principles Analysis of the Stability and Diffusion of Oxygen Vacancies in Metal Oxides,” *Physical Review Letters*, vol. 93, no. 22, pp. 3–6, 2004.

[128] R. Grimes, C. Catlow, and A. Stoneham, "A comparison of defect energies in MgO using Mott-Littleton and quantum mechanical procedures," *Journal of Physics: Condensed Matter*, vol. 1, pp. 7367–7384, 1989.

[129] D. Alfè and M. Gillan, "Schottky defect formation energy in MgO calculated by diffusion Monte Carlo," *Physical Review B*, vol. 71, no. 22, pp. 1–3, 2005.

[130] J. P. Perdew and K. Schmidt, "Jacob's ladder of density functional approximations for the exchange-correlation energy," in *Density Functional Theory And Its Application To Materials* (V. Van Doren, C. Van Alsenoy, and P. Geerlings, eds.), vol. 577, (Antwerp (Belgium)), pp. 1–20, AIP, July 2001.

[131] T. Brudevoll, E. Kotomin, and N. Christensen, "Interstitial-oxygen-atom diffusion in MgO.," *Physical review. B, Condensed matter*, vol. 53, pp. 7731–7735, Mar. 1996.

[132] L. Halliburton and L. Kappers, "Radiation-induced oxygen interstitials in MgO," *Solid State Communications*, vol. 26, pp. 111–114, Apr. 1978.

[133] P. K. de Boer and R. A. de Groot, "The conduction bands of MgO, MgS and," *Journal of Physics: Condensed Matter*, vol. 10, pp. 10241–10248, Nov. 1998.

[134] E. Kotomin, M. Kuklja, R. Eglitis, and a. Popov, "Quantum chemical simulations of the optical properties and diffusion of electron centres in mgo crystals," *Materials Science and Engineering B*, vol. 37, pp. 212–214, Feb. 1996.

[135] J. U. Reveles, A. M. Koster, S. N. Khanna, and C. Quintanar, "Surface Oxygen Diffusion into Neutral, Cationic, and Dicationic Oxygen Vacancies on MgO(100) Surfaces," *The Journal of Physical Chemistry C*, vol. 114, pp. 12265–12270, July 2010.

[136] B. Uberuaga, R. Smith, A. Cleave, R. Grimes, A. Voter, and K. Sickafus, "Accelerated molecular dynamics simulations of interstitial clusters in pure and Al-doped MgO," *Nuclear Instruments and Methods in Physics Research Section B: Beam Interactions with Materials and Atoms*, vol. 250, pp. 12–16, Sept. 2006.

[137] P. Pöml, T. Geisler, J. Cobos-Sabaté, T. Wiss, P. Raison, P. Schmid-Beurmann, X. Deschanels, C. Jégou, J. Heimink, and A. Putnis, "The mechanism of the hydrothermal alteration of Cerium- and Plutonium-doped zirconolite," *Journal of Nuclear Materials*, Dec. 2010.

[138] D. Roudil, X. Deschanels, P. Trocellier, F. c. ois Jomard, A. Boutry, C. Jègou, S. Peuget, D. Gosset, and P. Nivet, "Thermal diffusion of Helium and volatil fission products in UO2 and zirconolite nuclear ceramics," *MRS Proceedings*, vol. 824, Jan. 2004.

[139] F. Farges, R. C. Ewing, and G. E. Brown, "The structure of aperiodic, metamict (Ca, Th)ZrTi2O7 (zirconolite): An EXAFS study of the Zr, Th, and U sites," *Journal of Materials Research*, vol. 8, pp. 1983–1995, Aug. 1993.

[140] C. Pickard and R. Needs, "High-Pressure Phases of Silane," *Physical Review Letters*, vol. 97, July 2006.

[141] C. J. Pickard and R. J. Needs, "Structure of phase III of solid hydrogen," *Nature Physics*, vol. 3, pp. 473–476, May 2007.

[142] C. J. Pickard and R. J. Needs, "Ab initio random structure searching.," *Journal of physics. Condensed matter*, vol. 23, p. 053201, Feb. 2011.

[143] A. Morris, C. Pickard, and R. Needs, “Hydrogen/silicon complexes in silicon from computational searches,” *Physical Review B*, vol. 78, Nov. 2008.

[144] A. Morris, C. Pickard, and R. Needs, “Hydrogen/nitrogen/oxygen defect complexes in silicon from computational searches,” *Physical Review B*, vol. 80, Oct. 2009.

[145] B. M. Gatehouse, I. E. Grey, R. J. Hill, and H. J. Rossell, “Zirconolite, CaZrxTi3-xO7; structure refinements for near-end-member compositions with x = 0.85 and 1.30,” *Acta Crystallographica Section B Structural Crystallography and Crystal Chemistry*, vol. 37, pp. 306–312, Feb. 1981.

[146] J. P. Perdew, K. Burke, and M. Ernzerhof, “Generalized Gradient Approximation Made Simple,” *Physical Review Letters*, vol. 77, pp. 3865–3868, Oct. 1996.

[147] Miseki Y, Saito K, and Kudo A, “Nanocrystalline CaZrTi2O7 Photocatalyst Prepared by a Polymerizable Complex Method in the Presence of Cs2CO3 Flux for Water Splitting,” *Chemistry Letters*, vol. 38, no. 2, pp. 180–181, 2009.

[148] N. Hine, K. Frensch, W. Foulkes, and M. Finnis, “Supercell size scaling of density functional theory formation energies of charged defects,” *Physical Review B*, vol. 79, Jan. 2009.

[149] H.-J. Zhai and L.-S. Wang, “Probing the electronic structure and band gap evolution of titanium oxide clusters (TiO(2))(n)(-) (n = 1-10) using photoelectron spectroscopy.,” *Journal of the American Chemical Society*, vol. 129, pp. 3022–6, Mar. 2007.

[150] D.-Y. Kim, C.-H. Lee, and S. J. Park, “Preparation of zirconia thin films by metalorganic chemical vapor deposition using ultrasonic nebulization,” *Journal of Materials Research*, vol. 11, pp. 2583–2587, Oct. 1996.

[151] U. Seth and R. Chaney, “Energy-band structure of calcium-oxide crystals by the method of tight binding,” *Physical Review B*, vol. 12, pp. 5923–5930, Dec. 1975.

[152] A. Foster, V. Sulimov, F. Lopez Gejo, A. Shluger, and R. Nieminen, “Structure and electrical levels of point defects in monoclinic zirconia,” *Physical Review B*, vol. 64, Nov. 2001.

[153] A. Foster, F. Lopez Gejo, A. Shluger, and R. Nieminen, “Vacancy and interstitial defects in hafnia,” *Physical Review B*, vol. 65, May 2002.

[154] G.-Y. Huang, C.-Y. Wang, and J.-T. Wang, “First-principles study of diffusion of oxygen vacancies and interstitials in ZnO.,” *Journal of physics. Condensed matter : an Institute of Physics journal*, vol. 21, p. 195403, May 2009.

[155] N. P. Laverov, S. V. Yudintsev, T. S. Livshits, S. V. Stefanovsky, A. N. Lukinykh, and R. C. Ewing, “Synthetic minerals with the pyrochlore and garnet structures for immobilization of actinide-containing wastes,” *Geochemistry International*, vol. 48, pp. 1–14, Feb. 2010.

[156] D. Cherniak, J. Manchester, and E. Watson, “Zr and Hf diffusion in rutile,” *Earth and Planetary Science Letters*, vol. 261, pp. 267–279, Sept. 2007.

[157] J. Gavartin, P. Sushko, and A. Shluger, “Modeling charge self-trapping in wide-gap dielectrics: Localization problem in local density functionals,” *Physical Review B*, vol. 67, Jan. 2003.

[158] A. Shluger, P. Sushko, and L. Kantorovich, “Spectroscopy of low-coordinated surface sites: Theoretical study of MgO,” *Physical Review B*, vol. 59, pp. 2417–2430, Jan. 1999.

[159] A. Samanta, T. Lenosky, and J. Li, “Thermodynamic stability of oxygen point defects in cubic Zirconia,” p. 20, Sept. 2010.

[160] M. Rushton, C. Stanek, A. Cleave, B. Uberuaga, K. Sickafus, and R. Grimes, “Simulation of defects and defect processes in fluorite and fluorite related oxides: Implications for radiation tolerance,” *Nuclear Instruments and Methods in Physics Research Section B: Beam Interactions with Materials and Atoms*, vol. 255, pp. 151–157, Feb. 2007.

[161] P. M. Dehmer, S. T. Pratt, and J. L. Dehmer, “Photoelectron spectra of xenon dimer (Xe2*) obtained by resonantly enhanced multiphoton ionization,” *The Journal of Physical Chemistry*, vol. 91, pp. 2593–2598, May 1987.

[162] F. Ortmann, F. Bechstedt, and W. Schmidt, “Semiempirical van der Waals correction to the density functional description of solids and molecular structures,” *Physical Review B*, vol. 73, May 2006.

[163] T. Seletskaia, Y. Osetsky, R. Stoller, and G. Stocks, “Magnetic Interactions Influence the Properties of Helium Defects in Iron,” *Physical Review Letters*, vol. 94, Feb. 2005.

[164] A. Voter, “Hyperdynamics: Accelerated Molecular Dynamics of Infrequent Events,” *Physical Review Letters*, vol. 78, pp. 3908–3911, May 1997.